

---


Electronic Theses and Dissertations, 2004-2019

---

2016

## Catalytically Enhanced Heterogeneous Combustion of methane

Anthony Terracciano  
*University of Central Florida*

 Part of the [Mechanical Engineering Commons](#)  
Find similar works at: <https://stars.library.ucf.edu/etd>  
University of Central Florida Libraries <http://library.ucf.edu>

This Doctoral Dissertation (Open Access) is brought to you for free and open access by STARS. It has been accepted for inclusion in Electronic Theses and Dissertations, 2004-2019 by an authorized administrator of STARS. For more information, please contact [STARS@ucf.edu](mailto:STARS@ucf.edu).

---

### STARS Citation

Terracciano, Anthony, "Catalytically Enhanced Heterogeneous Combustion of methane" (2016). *Electronic Theses and Dissertations, 2004-2019*. 5271.  
<https://stars.library.ucf.edu/etd/5271>

**CATALYTICALLY ENHANCED HETEROGENEOUS  
COMBUSTION OF METHANE**

by

ANTHONY CARMINE TERRACCIANO

A.A. Broward College, 2010

B.S.M.E. University of Central Florida 2013

M.S.M.E. University of Central Florida 2014

A dissertation submitted in partial fulfillment of the requirements  
for the degree of Doctor of Philosophy  
in the Department of Mechanical and Aerospace Engineering  
in the College of Engineering and Computer Science  
at the University of Central Florida  
Orlando, Florida

Fall Term  
2016

Major Professors: Nina Orlovskaya & Subith S. Vasu

© 2016 Anthony Carmine Terracciano

## ABSTRACT

Heterogeneous combustion is an advanced internal combustion technique, which enables heat recuperation within the flame by utilizing a highly porous ceramic media as a regenerator. Heat released within the gas phase convectively transfers to the solid media. This heat within the solid media then travels towards the inlet, enabling reactant preheating. Such heat redistribution enables stable burning of both ultra-lean fuel/air mixtures, forming a more diffuse flame through the combustion chamber, and results in reduced pollutant formation. To further enhance heterogeneous combustion, the ceramic media can be coated with catalytically active materials, which facilitates surface based chemical reactions that could occur in parallel with gas phase reactions.

Within this work, a flow stabilized heterogeneous combustor was designed and developed consisting of a reactant delivery nozzle, combustion chamber, and external instrumentation. The reactant delivery nozzle enables the combustor to operate on mixtures of air, liquid fuel, and gaseous fuel. Although this combustor has high fuel flexibility, only gaseous methane was used within the presented experiments. Within the reactant delivery nozzle, reactants flow through a tube mixer, and a homogeneous gaseous mixture is delivered to the combustion chamber.  $\alpha$ -alumina ( $\alpha$ -Al<sub>2</sub>O<sub>3</sub>), magnesia stabilized zirconia (MgO-ZrO<sub>2</sub>), or silicon carbide (SiC) was used as the material for the porous media. Measurement techniques which were incorporated in the combustor include an array of axially mounted thermocouples, an external microphone, an external CCD camera, and a gas chromatograph with thermal conductivity detector which enable temperature measurements, acoustic spectroscopy, characterization of thermal radiative emissions, and composition analysis of exhaust gasses, respectively. Before evaluation of the various solid

media in the combustion chamber the substrates and catalysts were characterized using X-ray diffraction, X-ray fluorescence, scanning electron microscopy and energy dispersive spectroscopy.

MgO-ZrO<sub>2</sub> porous media was found to outperform both  $\alpha$ -Al<sub>2</sub>O<sub>3</sub> and SiC matrices, as it was established that higher temperatures for a given equivalence ratio were achieved when the flame was contained within a MgO-ZrO<sub>2</sub> matrix. This was explained by the presence of oxygen vacancies within the MgO doped ZrO<sub>2</sub> fluorite lattice which facilitated catalytic reactions. Several catalyst compositions were evaluated to promote combustion within a MgO-ZrO<sub>2</sub> matrix even further.

Catalysts such as: Pd enhanced WC, ZrB<sub>2</sub>, Ce<sub>0.80</sub>Gd<sub>0.20</sub>O<sub>1.90</sub>, LaCoO<sub>3</sub>, La<sub>0.80</sub>Ca<sub>0.20</sub>CoO<sub>3</sub>, La<sub>0.75</sub>Sr<sub>0.25</sub>Fe<sub>0.95</sub>Ru<sub>0.05</sub>O<sub>3</sub>, and La<sub>0.75</sub>Sr<sub>0.25</sub>Cr<sub>0.95</sub>Ru<sub>0.05</sub>O<sub>3</sub>; were evaluated under lean fuel/air mixtures. LaCoO<sub>3</sub> outperformed all other catalysts, by enabling the highest temperatures within the combustion chamber, followed by Ce<sub>0.80</sub>Gd<sub>0.20</sub>O<sub>1.90</sub>. Both LaCoO<sub>3</sub> and Ce<sub>0.80</sub>Gd<sub>0.20</sub>O<sub>1.90</sub> enabled a flame to exist at  $\phi=0.45\pm 0.02$ , however LaCoO<sub>3</sub> caused the flame to be much more stable. Furthermore, it was discovered that the coating of MgO-ZrO<sub>2</sub> with LaCoO<sub>3</sub> significantly enhanced the total emissive power of the combustion chamber. In this work as acoustic spectroscopy was used to characterize heterogeneous combustion for the first time. It was found that there is a dependence of acoustic emission on the equivalence ratio and flame position regardless of media and catalyst combination. It was also found that when different catalysts were used, the acoustic tones produced during combustion at fixed reactant flow rates were distinct

I would like to dedicate this work to Diana, my stunning and loving wife who puts up with me  
“Anthonying” everything. To 100 more beautiful years together.

## ACKNOWLEDGMENTS

I would like to thank my Dissertation Committee for their thought provoking questions and encouragement which is above and beyond anything I would have expected. I would also like to thank my primary adviser, Dr. Nina Orlovskaya, I have greatly enjoyed the opportunities and experiences I have been presented while working within her laboratory at the University of Central Florida. I would also like to thank Dr. Subith Vasu for help with my professional development and encouraging me to showcase my work around the nation.

Along the way there were many times in which I became distraught and disinterested in my research. Having lab mates to share jokes with or discuss science made everything much more bearable, thank you to: Amjad Aman, Samuel De Olivera, Richard Stadlemann “Dr. Dick”, Zhilin Xie, Manuel Robayo, Yan Chen, Alejandro Carrasco, Brayden Roque, Ryan Jordan, Ruslan Fayzalev, William Henken, Jonathan Torres, and all my other lab mates. I would also like to thank the many people whom I have collaborated and co-authored with on scientific papers: Zhilin Xie, Samuel De Olivera, Nina Orlovskaya, Richard Blair, Fernando Uribe-Romo, Subith Vasu, Deepti Siddhanti, Demetrius Vasquez-Molina and David Cullen.

Most importantly I would like to thank everyone in my family for providing me with the occasional place to crash, warm meal, and words of advice during the many points in my academic career where I was absolutely loosing my \*\*\*\*ing mind.

# TABLE OF CONTENTS

LIST OF FIGURES .....	X
LIST OF TABLES .....	XV
1. INTRODUCTION .....	1
1.1. Combustion.....	1
1.1.1. Chemical Equilibrium and Kinetics.....	4
1.1.2. Time Invariant Flowing Combustion.....	7
1.2. Heterogeneous Combustion.....	9
1.2.1. Excess Enthalpy (Super Adiabatic) Combustion .....	12
1.2.2. Fluid Phenomena of Heterogeneous Combustion.....	13
1.2.3. Heat Recirculation and Standing Flames .....	14
1.2.4. Transient Behavior of Flames Within Porous Media.....	19
1.3. Applications of Heterogeneous Combustion.....	21
1.3.1. Heat Source for Organic Rankine Cycle Combined Heat and Power Systems .....	21
1.3.2. Fuel Reformers for Fuel Cells.....	22
1.3.3. Efficient and Clean Gas Flares.....	23
1.3.4. Chemical Processors for Hydraulic Fracturing .....	24
1.3.5. Case Hardening.....	25
1.4. Goals of Research.....	26
2. LITERATURE REVIEW .....	27
2.1. Reactant Delivery and Mixing.....	31



2.2.	Combustion Chamber .....	33
2.2.1.	Inlet Plenum .....	34
2.2.2.	Reticulated Foam Properties .....	36
2.2.3.	Chamber Housing .....	38
2.3.	Instrumentation and Measurements .....	39
2.3.1.	Temperature Measurements Using Thermocouples.....	39
2.3.2.	Photographic Imaging .....	40
2.3.3.	Ex-Situ Gas Chromatography .....	42
2.3.4.	Acoustic and Pressure Measurement Techniques .....	45
2.4.	Heterogeneous Catalysis .....	47
2.4.1.	Substrate Reactivity .....	48
2.4.2.	Cerium Oxide Based Catalysts .....	49
2.4.3.	Perovskite Oxide Catalysts .....	50
2.4.4.	Tungsten Carbide/Palladium Catalysts .....	51
3.	<b>COMBUSTOR APPARATUS, CATALYST APPLICATIONS and EXPERIMENTAL METHODS .....</b>	<b>53</b>
3.1.	Introduction .....	53
3.2.	Methods of Reactant Delivery and Control.....	58
3.3.	Ex-Situ Instrumentation.....	65
3.3.1.	Acoustic Measurements Setup .....	66
3.3.2.	Optical Measurements Setup .....	66
3.3.3.	Gas Chromatography .....	67

3.4.	Characterization of Selected Substrates .....	68
3.4.1.	Silicon Carbide.....	69
3.4.2.	Magnesia Stabilized Zirconia.....	70
3.4.3.	Alumina Oxide.....	71
3.5.	Catalyst/Coating Characterization.....	72
3.5.1.	$Ce_{0.8}Gd_{0.2}O_{1.9}$ .....	72
3.5.2.	La Based Perovskites .....	75
3.5.3.	Tungsten Carbide Enhanced Palladium .....	81
3.5.4.	Zirconium Diboride .....	86
3.6.	Summary.....	87
4.	EXPRIMENTAL OBSERVATIONS .....	89
4.1.	Introduction .....	89
4.2.	Observations of the Combustor Using $Al_2O_3$ Media.....	90
4.3.	Catalyst/Substrate Performance Characterization .....	100
4.3.1.	Thermal Performance Overview .....	100
4.3.2.	Substrate Performance Overview.....	102
4.3.3.	$Ce_{0.8}Gd_{0.2}O_{1.9}$ Catalyst Performance .....	108
4.3.4.	$LaCoO_3$ Catalyst Performance .....	111
4.3.5.	Pd-WC Catalyst Performance .....	115
5.	CONCLUSIONS .....	121
	REFERENCES.....	122
.....		

## LIST OF FIGURES

Figure 1-1: Total flow rates and equivalence as functions of reactant flow rates. ....	3
Figure 1-2: Reactant flow rates presented as a function of total flow rate and equivalence ratio. .	4
Figure 1-3: Representation of various types of chemical reactions which occur in combustion [9]. .....	7
Figure 1-4: Temperature and OH profile of a laminar diffusion flame at 1 atm [11].....	8
Figure 1-5: Laminar burning velocity of a near adiabatic CH <sub>4</sub> -air flame [12] and adiabatic flame temperature (calculated) at one atmosphere [9].....	9
Figure 1-6: A) Reticulated foam. B) Packed bed of constant radii balls. ....	10
Figure 1-7: Various geometries for packed bed solids. A) Reschig ring. B) Dogbone. C) Saddle. D) Cross .....	10
Figure 1-8: A) Optical micrograph of SiC porous media. B) Idealized tetradecahedron representing a single cell [18].....	10
Figure 1-9: 2-D Flow-field through a porous medium at an aggregate 45° orientation from the flow direction [34].....	13
Figure 1-10: Schematic of heterogeneous combustion with thermal profile of gas and solid phases. .....	15
Figure 1-11: A) Solid Phase temperatures as a function of r*. B) Upper branch reactor profile at r*=10. C) Lower b reactor profile at r*=10. ....	18
Figure 1-12: Combustion wave in heterogeneous combustion of equal magnitude .....	19
Figure 1-13: A) Conditions of a flame beginning a progression towards the exhaust. B) Unstable progression of the flame continuing to blow off conditions. C) Flame settles at some new equilibrium position within the porous media. ....	20
Figure 1-14: Conditions of a flame beginning a progression towards the inlet. B) Unstable progression of the flame continuing to flashback conditions. C) Flame settling at some new equilibrium position within the porous media. ....	20
Figure 1-15: Flow Diagram for a Heterogeneous combustor to be used as a fuel reformer for a fuel cell stack.....	23
Figure 1-16: Flare stack connected to an oil field.....	24
Figure 1-17: Schematic of a hydraulic fracturing well. ....	24

Figure 1-18: Method of case hardening using a heterogeneous combustor.....	26
Figure 2-1: A) Ignition by external pilot flame. B) Ignition of a reacting flow by heterogeneous catalysis. C) Laser ignition. D) Conventional spark ignition.....	28
Figure 2-2: Heterogeneous combustor with a spark plug igniter. [52].....	28
Figure 2-3: Spray nozzle liquid fueled heterogeneous combustor [53].....	29
Figure 2-4: Bi-fuel loop shaped heterogeneous combustor [54]. .....	30
Figure 2-5: Heterogeneous combustor for combined heat and power [28]. .....	30
Figure 2-6: Multistage heterogeneous combustor using zirconia media [55].....	31
Figure 2-7: Combustion of a liquid fuel droplet in a laminar gas flow [60].....	32
Figure 2-8: Flow of air at 300K and 1 atm through 2D Ducts corresponding to Reynolds numbers of (upper) 4000 and (lower) 20000.....	35
Figure 2-9: Monolith structure featuring many small flow channels. ....	35
Figure 2-10: A thermocouple bead placed in a flow with some prescribed conditions while simultaneously being exposed to a surface. ....	40
Figure 2-11: Level curves of hemispherical black body emissive power.....	42
Figure 2-12: Diagram of a two Column Gas chromatograph. ....	43
Figure 2-13: Flow schematic diagram of a Valco-valve.....	44
Figure 2-14: Diagram of a TCD detector.....	45
Figure 2-15: Acoustic wave propagating in an isotropic medium with no interference from the surroundings or receivers. Versus an acoustic wave propagating through an isotropic medium with interference in the form of echo due to the interaction of the wave with the wall. ....	47
Figure 3-1: Exploded view of combustor .....	53
Figure 3-2: Schematic of the combustion chamber .....	54
Figure 3-3: Photograph of the experimental combustor in operation; the approximate flame.....	55
Figure 3-4: (A) Isometric view of combustion chamber exhaust side with shutters closed. (B) Isometric view of combustion chamber inlet side with shutters open exposing alumina windows. (C) Optical micrograph of the thermocouple designed for use along the combustion chamber axis. (D) Axial thermocouple schematic showing the separation of thermocouple probe from porous media via a wire mesh.....	56

Figure 3-5: A photograph of MgO stabilized ZrO <sub>2</sub> , Al <sub>2</sub> O <sub>3</sub> , and SiC porous ceramic media used for combustion experiments inside of the combustion chamber to contain a flame. The porous ceramic cylinders contain 10 pores per inch and have 50mm in diameter and 50.4mm in length.....	58
Figure 3-6: Block diagram of reactant delivery path. (1) compressor, (2) pressure gauge, (3) reservoir, (4) pressure regulating valve, (5) dryer, (6) flow controller, (7) methane cylinder, and (8) liquid fuel reservoir. ....	59
Figure 3-7: Assembly model and cross sectional view of fuel delivery nozzle. ....	60
Figure 3-8: (A) Exploded reactant flow diagram of siphon nozzle. (B) Reactant flow path when both liquid fuel and methane are simultaneously used. (C) Reactant flow path when only methane fuel is used. ....	61
Figure 3-9: Photos of (A) Inlet Cap assembled with siphon nozzle and supplemental inlet ports attached, liquid fuel inlet is capped off; (B) underside view of fuel inlet cap. (C) Assembled fuel delivery nozzle. ....	63
Figure 3-10: (A) Isometric view of flow streamlines and flow domain. (B) Side profile view of flow streamlines combustion chamber showing the length of recirculation.....	64
Figure 3-11: (A) A photograph of the heterogeneous combustor aligned with instrumentation devices within a fume hood. (B) A schematic for the location of the microphone, mirror, and CCD camera relative to the combustor exhaust port in the experimental set up. ....	65
Figure 3-12: Chromatograms of exhaust samples and air using the GC/TDC/sampling system incorporated to the heterogeneous combustion chamber. ....	68
Figure 3-13: (A) XRD pattern of SiC. (B and C) Scanning electron micrographs of SiC. ....	69
Figure 3-14: (A) X-ray diffraction pattern; (B) and (C) SEM micrographs of the surface of the 3 wt% MgO stabilized ZrO <sub>2</sub> ceramic. ....	71
Figure 3-15: (A) X-ray diffraction pattern; (B) and (C) SEM micrographs of the surface of the Al <sub>2</sub> O <sub>3</sub> ceramic. ....	72
Figure 3-16: (A) X-ray diffraction pattern; (B) and (C), SEM micrographs and (D) EDS of Ce <sub>0.8</sub> Gd <sub>0.2</sub> O <sub>1.9</sub> catalyst powders used for coating the 3 wt% MgO stabilized ZrO <sub>2</sub> porous media. ....	73
Figure 3-17: (A) X-ray diffraction pattern; (B) and (C) SEM micrographs and (D) EDS spectrum of the 3 wt% MgO stabilized ZrO <sub>2</sub> porous media with Ce <sub>0.2</sub> Gd <sub>0.8</sub> Ce <sub>1.9</sub> coating. ....	75
Figure 3-18: A) XRD pattern, (B and C) SEM micrographs, and D) EDS spectra of LaCoO <sub>3</sub> ....	76
Figure 3-19 A) XRD pattern, (B and C) SEM micrographs, and D) EDS spectra of La <sub>0.80</sub> Ca <sub>0.20</sub> CoO <sub>3</sub> .....	77

Figure 3-20: A) XRD pattern, (B and C) SEM micrographs, and D) EDS spectra of $\text{La}_{0.75}\text{Sr}_{0.25}\text{Cr}_{0.95}\text{Ru}_{0.05}\text{O}_3$ .	78
Figure 3-21: A) XRD pattern, (B and C) SEM micrographs, and D) EDS spectra of $\text{La}_{0.75}\text{Sr}_{0.25}\text{Fe}_{0.95}\text{Ru}_{0.05}\text{O}_3$ .	79
Figure 3-22: A) XRD pattern, (B and C) SEM micrographs, and D) EDS spectra of $\text{LaCoO}_3$ on GDC coated MSZ media.	80
Figure 3-23 (A) Uncoated $\text{MgO-ZrO}_2$ media. (B) Pd enhanced WC coated $\text{MgO ZrO}_2$ media...	83
Figure 3-24: (A) SEM SE micrograph of WC-Pd catalyst powder showing detail of crystallite surface and location of EDS. (B) Selected area EDS of WC-Pd catalyst powder.	84
Figure 3-25: X-Ray Diffraction pattern of the WC-Pd catalyst powder.	85
Figure 3-26: Scanning electron micrographs of the surface of $\text{MgO-ZrO}_2$ porous media coated with WC-Pd. (A) secondary electron and (B) back scattered detector micrograph. (C) EDS of the region of surface depicted in the micrographs.	85
Figure 3-27: (A) BSD Electron micrograph image of catalyst coated surface, with selected area EDS shown. (B) Close up BSD electron micrograph of EDS region. (C) BSD micrograph of EDS region. (D) SE micrograph of EDS region.	86
Figure 3-28: (A and B) SE Electron micrograph image of the $\text{ZrB}_2$ catalyst coated MSZ media surface, with selected area EDS shown. (C) EDS spectra of regions within micrographs.	87
Figure 4-1: Time evolution of selected thermocouples, shown with steady state burning delineations at each equivalence ratio.	91
Figure 4-2: (A) Flame at various positions within the combustion chamber shortly after ignition. (B) Time evolution of selected thermocouples during ignition and warm up. (C) Acoustic profiles at selected times.	93
Figure 4-3: A) Time evolution of selected thermocouples within the combustion chamber between the achieved steady state at $\phi=0.51$ to $\phi=0.49$ , vertical lines on the plot indicate when acoustic profiles were recorded. B) Acoustic profiles recorded at various times as the combustor approaches steady state following the $\phi=0.51$ to $\phi=0.49$ transition.	95
Figure 4-4: Observed temperature profiles across the combustion chamber at given equivalence ratios.	97
Figure 4-5: Acoustic profiles corresponding to the equivalence ratios presented.	98
Figure 4-6: Images of the combustion chamber exit plane at given equivalence ratios.	100

Figure 4-7: Axial temperature profiles of the catalyst and substrate combinations are presented for selected equivalence ratios.....	101
Figure 4-8: Axial temperature profiles at $\phi=0.47\pm 0.02$ for the MSZ media and catalysts coated onto the MSZ substrate. ....	102
Figure 4-9: Axial temperature profiles of the selected substrates at various equivalence ratios. ....	103
Figure 4-10: Acoustic profiles over the range of steady states pertaining to the selected substrates. ....	104
Figure 4-11: Equivalence ratio pertaining to operation of the combustion chamber with various substrates at the equivalence ratio of $\phi=0.75\pm 0.02$ .....	105
Figure 4-12: Equivalence ratio pertaining to operation of the combustion chamber with various substrates at the equivalence ratio of $\phi=0.53\pm 0.02$ .....	106
Figure 4-13: Photographs of radiative emissions of the porous media through the combustion chamber exhaust.....	107
Figure 4-14: Photographs of radiative emissions of the porous media through the combustion chamber exhaust.....	109
Figure 4-15: Photographs of radiative emissions of the porous media through the combustion chamber exhaust.....	110
Figure 4-16: Axial temperature profile of the combustion chamber containing MSZ media coated with $\text{LaCoO}_3$ . ....	111
Figure 4-17: Acoustic and optical characterization of the exhaust emissions while $\text{LaCoO}_3$ coated MSZ media was immersed in the combustion chamber. ....	114
Figure 4-18: Acoustic and optical characterization of the exhaust emissions while $\text{LaCoO}_3$ coated MSZ media was immersed in the combustion chamber. ....	116
Figure 4-19: Optical images of the combustor exhaust with Pd Enhanced WC catalyst. ....	117
Figure 4-20: Acoustic profiles from the combustion chamber with a Pd-WC catalyst. ....	119

## LIST OF TABLES

Table 1-1: Characterized regimes of heterogeneous combustion .....	11
Table 1-2: Boundary conditions for nondimensionalized equations (1-17) through (1-19).....	17
Table 1-3: Description of coordinate transforms corresponding to equations (1-20) through (1-24). .....	17
Table 1-4: Types of novel organic compounds, and water, for closed loop turbine cycles [42]..	22
Table 2-1: Design considerations of a heterogeneous combustor. ....	27
Table 2-2: Heterogeneous combustor sizing by air flow rate SLPM.....	33
Table 2-3: Properties of selected refractory ceramics [76]. ....	36
Table 2-4: Thermal conductivities of select gasses at 400 K [92].....	45

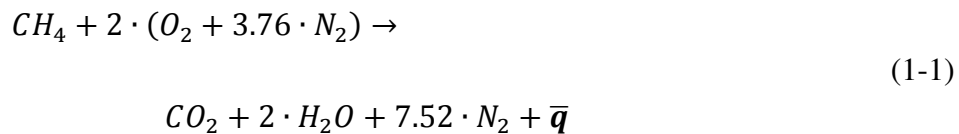


# 1. INTRODUCTION

## 1.1. Combustion

Combustion is an exothermic redox chemical reaction between a fuel and an oxidizer [1, 2]. A combustion reaction requires three components: fuel, oxidizer, and a “*spark*” to ignite the reactants. Once combustion has begun, the reaction will terminate if only one of three conditions are met: **1** if quenching occurs, **2** local molecular species concentration disallows the collision of reacting species or **3** the reaction byproducts are at an entropy maximizing equilibrium with remaining reactants.

Within this work the most fundamental equation is that which represents the chemical reaction of methane combustion in air, (1-1); which represents the idealized stoichiometric conversion of reactants to their respective products, and  $\bar{q}$  *the quantity of heat released*. For simplicity it is assumed “air” is wholly comprised of oxygen and nitrogen in a molar ratio of 1: 3.76. For methane the stoichiometric ratio, or ratio which describes neither reagent in excess, is 1 mole of methane per 2 moles of oxygen. For other combinations of fuels, and oxidizers the stoichiometric ratio will inherently change with chemical compositions.



While (1-1) characterizes a combustion reaction of methane when there is no excess of either reactant, if a reactant is outside of the stoichiometric ratio the other reactant will not be entirely consumed. Furthermore, if the reactants are in such disproportion, the reaction will cease to initiate or progress [3]. To assist in the characterization of a reacting mixture a dimensionless parameter which represents the ratio of fuel to oxidizer, relative to the stoichiometric fuel to oxidizer ratio is

presented: the *equivalence ratio*,  $\phi$ . The equivalence ratio dictates how much of a single reagent will remain in excess following combustion, among other important parameters. When a combustion process uses air as the oxidant, the molar quantity of oxidizer is comprised only of the diatomic oxygen within the air and therefore in air the stoichiometric mixture of methane-air can be represented as (1-2).

$$\phi = \frac{\left( \frac{n_{CH_4}}{n_{air} \cdot 1/4.76} \right)_{actual}}{\left( \frac{(1)_{CH_4}}{(2)_{oxygen}} \right)_{stoichiometric}} \quad (1-2)$$

When considering a combustion reaction in a flowing device, the flow rate of reactants must adhere to a certain relative ratio in order to remain within compliance of the stoichiometric equation. The unit *standard liter per minute SLPM*, is defined as volume of one liter of gaseous reagent delivered in one minute taken at *standard temperature*  $T_{std}$  (1-3), and *standard pressure*  $P_{std}$  (1-4). *SLPM* is a convenient unit of measure as the flow rate of reactants and the molar flow rate are correlated by the *molar specific volume*  $\bar{v}_{std}$  (1-5) where  $\bar{R}_u$  is *the ideal gas constant*. Therefore  $\phi$  may be expressed in terms of the *molar flow rate*,  $\dot{n}$ , as in (1-6).

$$T_{std} \equiv 295.4 \text{ K} \quad (1-3)$$

$$P_{std} \equiv 101.35 \cdot 10^3 \text{ Pa} \quad (1-4)$$

$$\bar{v}_{std} \equiv \left( \bar{R}_u \cdot T_{std} / P_{std} = 24.23 \text{ L/mol} \right) \quad (1-5)$$

$$\phi = \frac{\left( \frac{\dot{n}_{CH_4}}{\dot{n}_{air} \cdot 1/4.76} \right)_{actual}}{\left( \frac{(1)_{CH_4}}{(2)_{oxygen}} \right)_{stoichiometric}} \quad (1-6)$$

When considering the design of a flowing combustor where no diluent is used, it is convenient to work between two related coordinate systems which describe the delivery rate and mixture composition: **1** as a function of fuel and oxidizer flow rates, and **2** as a function of equivalence ratio and total flow rate. For methane combustion occurring in air the graphical coordinate systems are presented in Figure 1-1 and Figure 1-2.

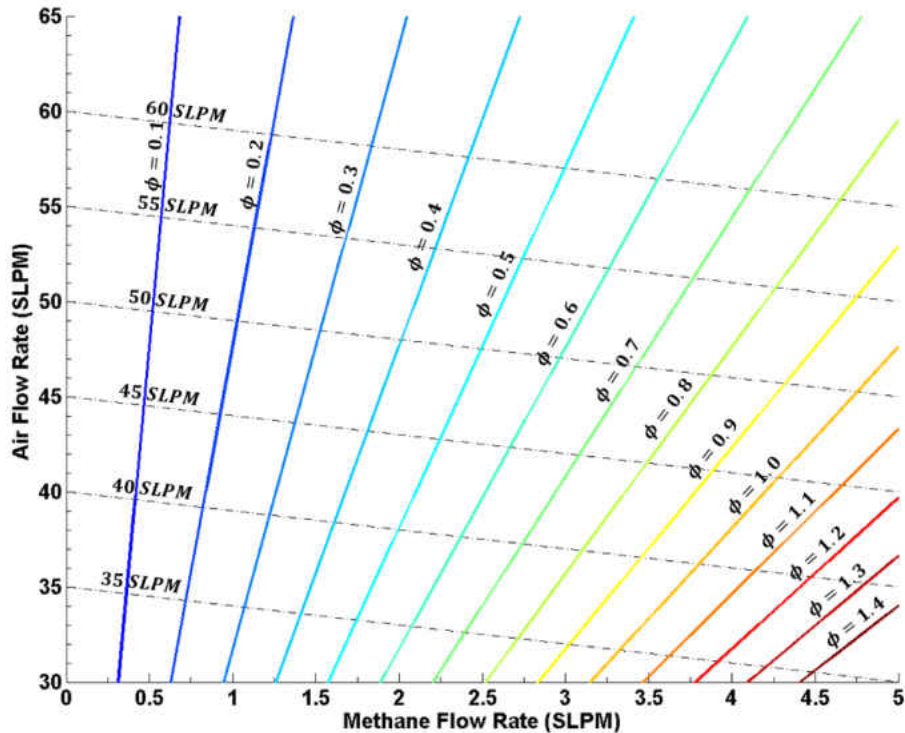


Figure 1-1: Total flow rates and equivalence as functions of reactant flow rates.

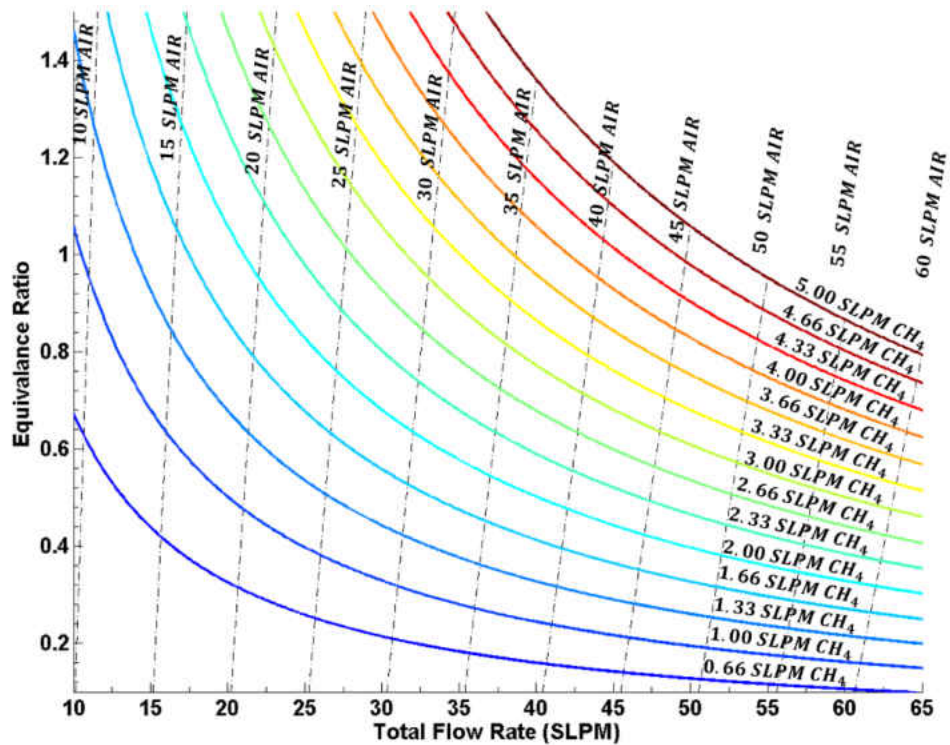


Figure 1-2: Reactant flow rates presented as a function of total flow rate and equivalence ratio.

Combustion must satisfy conservation principles and the entropy maximum postulate. Consequently the mathematics used to describe combustion must also account for these principles, while atomic species, energy, and mass conservation are satisfied by the balancing of chemical equations as in (1-1); (1-1) fails to account for entropy maximization [1]. Section **Error! eference source not found.** accounts for the maximization of entropy and a description of the chemical process by which entropy may maximize. Section 1.1.2 discusses the nature of conventional combustion in a flowing system.

### 1.1.1. Chemical Equilibrium and Kinetics

A generalized form of a chemical reaction is presented in (1-7) where  $X_i$  is the reacting species or product,  $\mu_i$  is the stoichiometric coefficient of the  $i$ 'th reactant species, and  $\nu_i$  is the

*stoichiometric coefficient of the i'th product species*. Real combustion does not entirely consume reactants even when reactants are in the stoichiometric ratio. Incomplete and/or undesired reaction byproducts such as CO and NO<sub>x</sub> may also be formed during combustion under conditions of excess oxidizer, under circumstances of locally insufficient oxidizer, or near the interface of an inhibiting solid phase soot may be formed [4-6].

$$\sum_i \mu_i \cdot X_i \leftrightarrow \sum_i \nu_i \cdot X_i \quad (1-7)$$

For every chemical reaction, entropy maximization is accounted for through the temperature change between reactants and products and a reaction specific *equilibrium pressure constant*  $K_p$  (1-8), which is derived from the minimization of Gibb's Free Energy across the reaction [1], where  $P$  is the gas pressure and  $\bar{n}_i$  is the molar quantity of the i'th species in the gas phase. The sum of all numbers of moles of a given species  $\bar{n}_i$  is related to  $\nu_i$  by the quantity of reactants.

$$K_p = \prod_i X_i^{\nu_i \oplus \mu_i} \cdot P \cdot \left( \bar{n}_i / \sum_i \bar{n}_i \right)^{\sum_i \nu_i - \sum_i \mu_i} \quad (1-8)$$

While a combustion processes may be represented by a single chemical reaction, such reaction is highly improbable; and this reaction is used to model the global equilibrium. Instead, combustion may be conceptualized as a process which consumes and produces various molecular species. Consumption and production of molecular species within combustion occurs through several reaction pathways, which are comprised of specific chemical reactions occurring in series and parallel. Furthermore not all reactions proceed at a single rate, each reaction occurs at a specific rate based upon the temperature, reacting species, and byproducts.

Chemical reaction rates are characterized by their *rate constant*  $K(T)$  (1-9), which is always a function of temperature and three other reaction specific parameters: *reaction activation energy*

$E_a$ , the **exponential prefactor**  $A$ , and a **correction factor**  $n_1$ . From (1-7), the bidirectional arrow  $\leftrightarrow$  is an indication of a chemical reaction in equilibrium, and therefore there is the possibility of the reaction occurring in both the forward and reverse direction. While literature will typically report a **forward reaction rate** constant denoted by the subscript  $f$ , it is possible to evaluate the **reverse reaction rate** constant denoted by subscript  $r$  based upon  $K_p$  in (1-10).

$$K(T) = A \cdot T^{n_1} \cdot e^{\frac{-E_a}{R_u \cdot T}} \quad (1-9)$$

$$\frac{K_f(T)}{K_r(T)} \equiv K_p \cdot \left(1 / (\bar{R}_u \cdot T)\right)^{\sum_i v_i + \sum_i \mu_i} \quad (1-10)$$

For a specific chemical reaction, the rate at which the **product species**  $X_k$ , is produced (1-11) is a function of the products of all reacting species considered in that reaction and the rate constant. When considering a chemical mechanism, a group of chemical reactions which describe an event, it is necessary to consider the net rate of production for the product species of interest which is a linear composite of all reactions which influence that species occurring simultaneously (1-12). Chemical modeling of combustion may incorporate thousands of molecular species and tens of thousands of reactions [7], though it is often far beyond practicality to model combustion in such explicit detail. For engineering applications it is often advantageous to employ a compact chemical mechanism [8] to enable the study of many phenomena simultaneously.

$$\frac{d_i[X_k]}{dt} = K_i(T) \cdot \prod [X_j] \quad (1-11)$$

$$\frac{d[X_k]}{dt}_{global} = \sum_i \frac{d_i[X_k]}{dt} \quad (1-12)$$

All chemical reactions which occur during combustion may be designated as one of the following types: **1** initiation, **2** propagation, **3** branching, and **4** termination [1] examples of each type are presented in Figure 1-3. Initiation reactions occur between stable species to

produce/consume one or more unstable species known as radicals; radicals may be characterized as a molecular species which has one or more unpaired electrons. Propagation reactions both consume and produce radicals with a net production of zero. Branching reactions produce more radicals than are consumed. Lastly, termination reactions consume radicals.

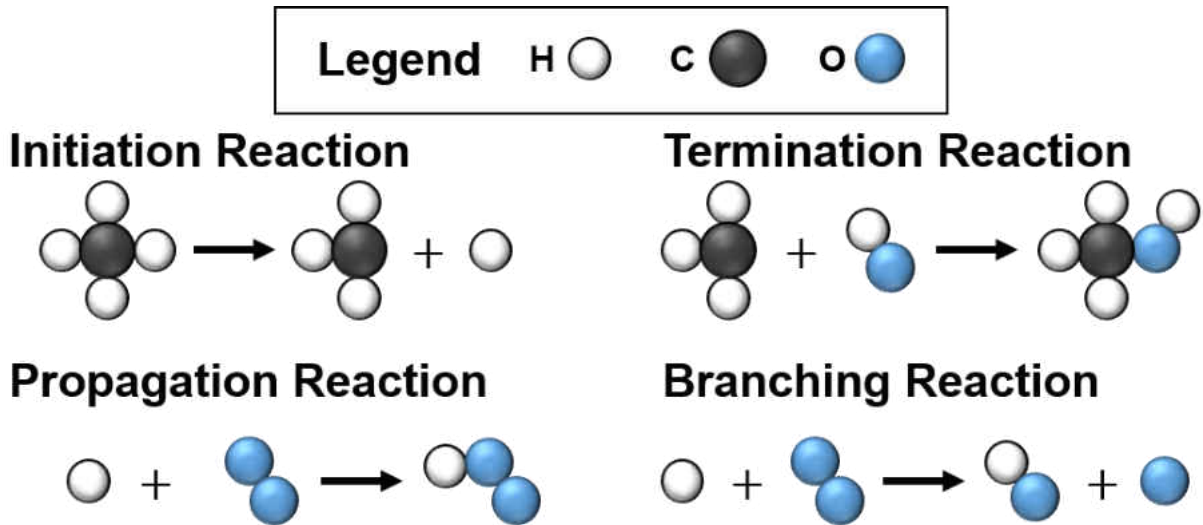


Figure 1-3: Representation of various types of chemical reactions which occur in combustion [9].

### 1.1.2. Time Invariant Flowing Combustion

In steady flow combustion, a stable operating condition must exist to maintain time invariant spatial characteristics of combustion. A flame may be considered as a reaction wave propagating relative to a flowing gas which may be luminous within the visible spectrum [10]. Consider a laminar diffusion flame similar to that of a Bunsen burner flame. Which has premixed reactants with some initial prescribed temperature, equivalence ratio, and mass flow rate. Depending on the conditions of the reacting flow and the *rate at which heat is released from the flame*  $\dot{q}_{out}$ , the *flame thickness*  $\delta_L$  will assume a characteristic value after some *preheating length*  $x_o$ . Using various measurement techniques, a profile of temperature and chemical species may be taken, a characteristic profile of temperature and OH profiles are presented in Figure 1-4 [11].

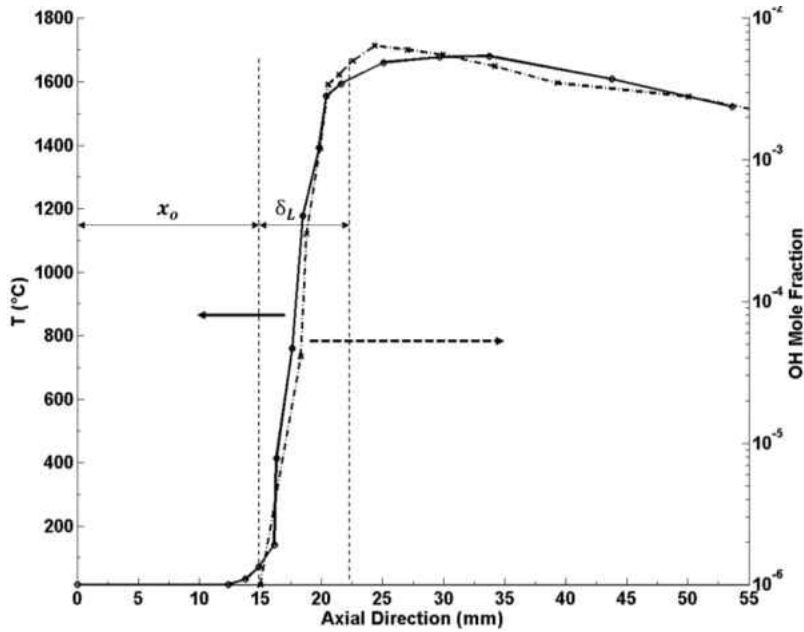


Figure 1-4: Temperature and OH profile of a laminar diffusion flame at 1 atm [11].

At a prescribed set of conditions, reactants delivered to a flame will cross the boundary entering the flame at a characteristic parameter, *laminar flame speed*  $S_L$ . From measurements observed of an adiabatic diffusion flame,  $S_L$  can be seen as a function of equivalence ratio and the species of fuel within the reacting mixture [12], the laminar flame speed is presented for methane. It is of importance to note  $S_L$  has also been shown to vary inversely with the static pressure at which combustion occurs for both lean and slightly rich fuel air mixtures [13]. Similarly, there is a maximum amount of thermal energy which may be released from combustion of a mixture of a given fuel, oxidizer, and diluents creating a “maximum” limit on flame temperature, known as the *adiabatic flame temperature*  $T_{adb}$ .  $S_L$  and  $T_{adb}$  are presented in Figure 1-5 for a CH<sub>4</sub>-Air diffusion flame at 1 atm.



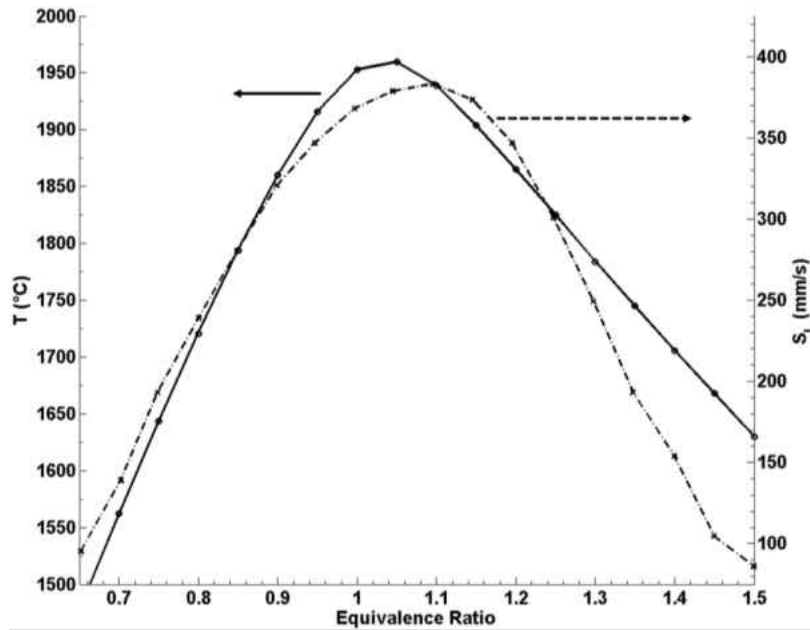


Figure 1-5: Laminar burning velocity of a near adiabatic  $CH_4$ -air flame [12] and adiabatic flame temperature (calculated) at one atmosphere [9].

## 1.2. Heterogeneous Combustion

As an expansion of conventional diffusion flame combustion in which heat transport is limited to small length scales [10], heterogeneous combustion is a method of combustion in which a fuel and oxidizer mixture is burned within the voids of a high surface area solid, porous media. Porous media refers to a solid which has a network of common size flow chambers connected by openings of a smaller size [6].

Multiple types of porous media are seen across literature and proprietary designs [14-17]. Media types are arranged into two groups; reticulated foam, and packed beds for which the simplest shape consist of constant diameter spheres Figure 1-6; more complicated geometries for packed beds may be seen in Figure 1-7. While each media geometry offers specific advantages, all designs seek to achieve a high specific surface area and low total pressure drop. Composition of the solid structures need only provide high temperature structural and chemical stability; for packed bed

substrates the likelihood of fracture decreases as the individual pieces are not rigidly arranged however contact resistance can minimize thermal conductivity [17].

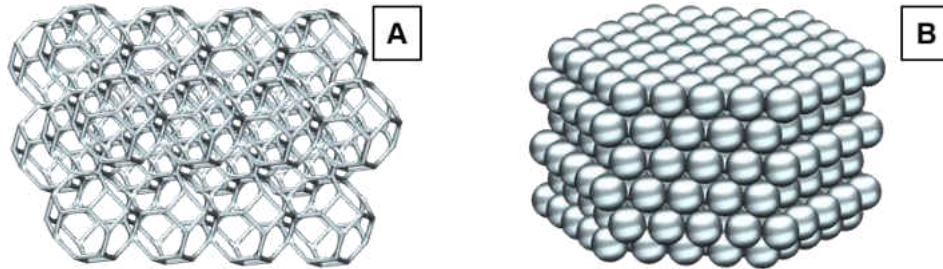


Figure 1-6: A) Reticulated foam. B) Packed bed of constant radii balls.

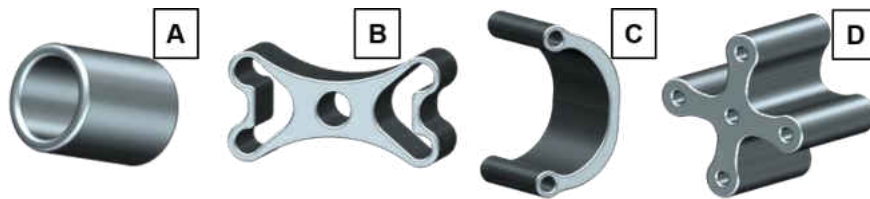


Figure 1-7: Various geometries for packed bed solids. A) Reschig ring. B) Dogbone. C) Saddle. D) Cross

Within this work reticulated ceramic foam porous media is used. While the actual shape of the foam is somewhat random, models have been proposed which show the structure to be a tessellatable tetradecahedron, a 3D solid with 14 faces, comprised of hexagonal and square openings. [14, 18]. A micrograph of the media and idealized shape are presented in Figure 1-8.

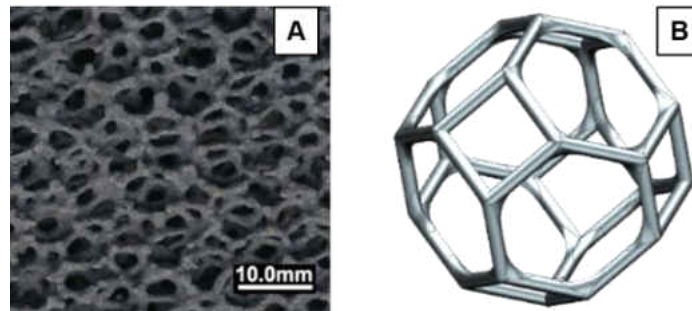


Figure 1-8: A) Optical micrograph of SiC porous media. B) Idealized tetradecahedron representing a single cell [18].

Experimental results and numerical simulations exemplify three parameters which determine the stabilization of flames within heterogeneous combustion when the reacting mixture is

homogenous: **1** equivalence ratio, **2** reactant flow rate, and **3** the heat flux leaving the combustion chamber [19, 20]. Multiple methods are used to characterize regimes of heterogeneous combustion, summarized in Table 1-1, many of which are simultaneously used to describe heterogeneous combustion in detail.

**Table 1-1: Characterized regimes of heterogeneous combustion**

<b>Characterization</b>	<b>Description</b>	<b>Ref</b>
Low Velocity Wave Propagation	Wave position moves on the order of 1mm/s.	[21]
High Velocity Wave Propagation	Wave position moves on the order of m/s.	
Co Flow	Flame wave proceeding with reactants.	[22]
Counter Flow	Flame wave moves against reactants.	
Stationary Flow	Flame wave is at an equilibrium position.	
Reciprocating Flow	Flame wave oscillates about an equilibrium.	[23]
Subadiabatic	Maximum flame temperature is below mixture $T_{adb}$ .	[17]
Superadiabatic	Maximum flame temperature is above mixture $T_{adb}$ .	
Flashback	Flame is between the inlet and porous media.	[19]
Submerged	Flame is stabilized within the porous media.	
Surface	Flame is stabilized at the exhaust of the porous media.	
Rich	Burning mixture has equivalence ratio in excess of 1.	[17]
Lean	Burning mixture has equivalence ratio below 1.	
Stoichiometric	Burning mixture has an equivalence ratio of 1.	
Catalytic	Surface participates in chemical reactions.	[24]
Non-Catalytic	Surface does not participate in chemical reactions.	

The flame structure of heterogeneous combustion may be viewed as an aggregate mix of thermal, chemical species concentration, and pressure waves within a chemically reacting flow [25]. In order to explain the characterization parameters presented in Table 1-1 and to give an understanding of heterogeneous combustion: 1.2.1 discusses excess enthalpy combustion, 1.2.3 explains the thermal structure of heterogeneous combustion, **Error! Reference source not found.** discusses fluid phenomena which are unique to the poly-phase nature of heterogeneous combustion, and 1.2.4 discusses the transitional processes of a flame which exhibits a non-static equilibrium position.

### 1.2.1. *Excess Enthalpy (Super Adiabatic) Combustion*

Excess enthalpy combustion was first postulated during the 1970's [26] as a type of combustion which enabled the transfer of enthalpy from the products to the reactants. Heterogeneous combustion was presented as an in-situ means of achieving excess enthalpy combustion. Heterogeneous combustion is fundamentally different from other forms of combustion as the solid within the combustion chamber enables the recirculation of large quantities of heat over a length scale orders of magnitude larger than conventional combustion.

Through the solid phase, heat may recirculate through the reacting environment through modes unavailable in diffusion flame combustion [17]. Thermal feedback through the solid phase enables substantial reactant preheating prior to the release of chemical energy from the reactants [27], thereby enabling a temperature within the chemically active region of the flow to be in excess of the adiabatic flame temperature for the unreacted mixture; this advanced mode of burning is termed super adiabatic combustion [28]. As a result of the emplaced solid, burners with inert porous materials offer a more even distribution of heat along the axial profile of the flow, reduced NO<sub>x</sub> emissions, reduced acoustic noise compared to diffusion flame combustors, the ability to efficiently emit thermal radiation, and an expansion of flammability limits, with such combustors operating with equivalence ratios between 0.1 and 4.0 [17, 29-31].

Flame behavior for combustion occurring within reticulated ceramic foams has been shown to correlate strongly with the optical thickness of the foam, where increased radiative heat transfer within the flames structure has been shown to enhance burning rate and flame temperature [32] to a point. If the pore size is excessively small the rate of heat release from combustion will fail to exceed what is absorbed by the solid; a loosely defined *critical Péclet Number  $Pe^*$* , or ratio of

advective to diffusive transport, is used to characterize a lower pore size limit (1-13) where  $\alpha_f$  is *the thermal diffusivity of the reactants* and  $d_m$  *the equivalent combustion chamber diameter* [33] where, for values of  $Pe < Pe^*$  the flame will extinguish.

$$45 < (Pe^* = S_L \cdot d_m / \alpha_f) < 65 \quad (1-13)$$

### 1.2.2. Fluid Phenomena of Heterogeneous Combustion

Fluid flow within porous media has a bulk flow direction from the inlet to the exhaust, pictured in Figure 1-9. However, due to the tortuous nature of the porous solid, the local flow can be approximated as moving with velocity components of  $45^\circ$  from the “flow direction” [34]. Such flow structure results in highly irregular flow patterns which vary with the rate at which reactants progress through the porous media [35].

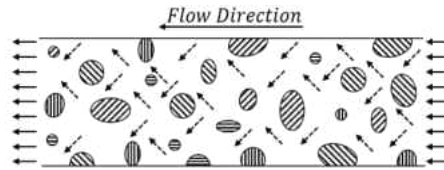


*Figure 1-9: 2-D Flow-field through a porous medium at an aggregate  $45^\circ$  orientation from the flow direction [34].*

Within the flow of a multicomponent mixture moving through porous media, two effects are prominent: dispersion and diffusion [36]. Dispersion and diffusion both act to mix the chemical species of a multi-component fluid; however dispersion is a macro-scale phenomena acting over significantly larger length scales than diffusion and is a characteristic of flow [36, 37]. In flows where both diffusion and dispersion are present, the rates of species mixing are a linear combination of the two processes [36].

Due to viscous effects of a flowing fluid over a solid at the gas-solid interface, without combustion occurring, a total pressure drop within the porous media exists [25]. Across literature,

the permeability, or measure of flow resistivity through the solid phase, has been shown to vary across orders of magnitude [38]. Using the **Reynolds Number  $Re$** , (1-14) where:  $\bar{u}$  *is the mean fluid velocity*, and  $\mu$  *is the fluid viscosity*; three flow schemes have been identified when  $Re < 2.3$ ,  $5 < Re < 80$ , and  $120 < Re$  [35].

$$Re = \bar{u} \cdot \frac{\rho \cdot d_m}{\mu} \quad (1-14)$$

For situations of low flow velocity corresponding to  $Re < 2.3$  the shear stresses on the fluid are negligible and Darcy's Law (1-15) may be used to represent the corresponding pressure differential, where:  $\kappa$  *is the specific permeability*, and  $P_t$  *is total pressure* [38]. For reticulated foams used in heterogeneous combustion,  $\kappa$  is typically near 1 and is a function of flow velocity. At higher flow rates,  $5 < Re < 80$  it is possible to use the Forchheimer equation (1-16) which is a nonlinear pressure drop through a solid which includes the *inertial coefficient  $C_f$*  of the solid through which the fluid flows [18]. For  $120 < Re$ , the principal region of interest in heterogeneous combustion, flow becomes entirely turbulent and unsteady characteristics exist [18].

$$\bar{u} = \frac{\kappa}{\mu} \cdot \frac{\partial P_t}{\partial x} \quad (1-15)$$

$$\frac{\partial P_t}{\partial x} = \bar{u} \cdot \left( \frac{\mu}{\kappa} + \bar{u} \cdot \frac{\rho \cdot C_f}{\sqrt{\kappa}} \right) \quad (1-16)$$

### 1.2.3. Heat Recirculation and Standing Flames

Within heterogeneous combustion, flames may either be stationary with the time averaged position is constant with respect to a fixed point or transient where the time averaged position of the flame is moving with respect to a fixed point. Referring to Figure 1-10, a characteristic

representation of a heterogeneous flame, of thickness  $\delta_L$ , which exists within the voids of porous media some *span  $x_e$  from the reactor inlet*, is presented along with a thermal profile of the gas and solid phases. Regions where the gas temperature is in excess of that of the solid temperature causes heat to be convectively transferred to the solid. Heat which is propagates toward the inlet of the combustion chamber through the solid phase may then be convectively transferred from the solid to the gas enabling reactant preheating without releasing chemical energy from the flow.

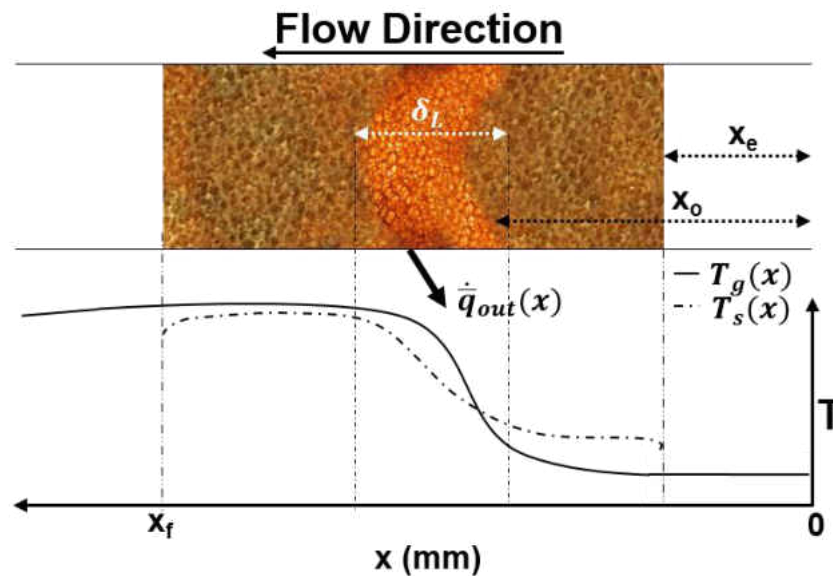


Figure 1-10: Schematic of heterogeneous combustion with thermal profile of gas and solid phases.

Two limiting cases exist for heterogeneous combustion relative to the amount of interphase heat exchange and heat exchange across the solid exist. In the case of extremely high heat transfer through the solid, which is attributed to both a high *thermal conductivity  $k$*  and *emissivity  $\epsilon$* , temperature differences between gas and solid phase decrease in magnitude and the solid can be modeled as isothermal. Conversely in the case of low heat transfer through the solid phase, temperature differences between the two phases becomes increasingly large and temperature variations along the dimensions of the solid phase become increasingly large [22, 39].

An analytical model of heterogeneous combustion was derived [20, 39] employing a single step irreversible chemical reaction over an isothermal solid by extending the equations used to model conventional diffusion flames [40, 41] through the inclusion of an additional term for interphase heat transfer. It is assumed: fluid mass flow rate is sufficiently small to yield an isobaric process, participation of the gas in radiative heat transfer is neglected, the surface is assumed to be chemically inert and the Lewis Number can be assumed unity. Within (1-17) the energy conservation equation, *thermal conductivity of the fluid*  $k_f$  and the accompanied Laplacian represent thermal conduction within the flow, *mass flux*  $\dot{m}''$ , a first derivative of temperature, and *specific heat*  $C_p$  comprise the advection term. Chemical reactions are accounted for through Arrhenius reaction rate and the *formation enthalpies*  $\Delta H_f^\circ$  of the reactants and products where there is an additional heat transfer term is considered between the gas and solid phase characterized by the *convection coefficient*  $h$ . If  $h$  is zero, then (1-17) will collapse, representing a diffusion flame.

$$\frac{d}{dx} \left( k_f \frac{dT}{dx} \right) - \dot{m}'' \cdot C_p \cdot \frac{dT}{dx} + \frac{d[X_k]}{dt} \cdot (\Delta H_f^\circ_1 - \Delta H_f^\circ_2) \quad (1-17)$$

$$+ h \cdot (T_s - T_x) = 0$$

Thermal losses through the combustion chamber wall may be accounted for by, equation over the length of the solid  $x_e$  to  $x_f$ . By treating  $Y$  as the independent variable which is monotonically increasing, solutions of the equations (1-17) and (1-18) are then produced according to a series of mass flux dependent Eigen Values, expressed as equation (1-19); implicitly solving for the solid phase temperature as a two point boundary value problem. Variables from equations (1-17) through (1-19) are then nondimensionalized according to Table 1-3, using values listed in Table



1-2 as boundary conditions where (1-25) represents interfacial heat transfer between the solid and gas phase.

**Table 1-2: Boundary conditions for nondimensionalized equations (1-17) through (1-19).**

Boundary Condition	Value
Inlet Boundary Product Fraction	$Y^* = 0$
Inlet Boundary Gas Temperature	$T^* = 0$
Exhaust Product Fraction	$Y^* = 1$
Exhaust Boundary Gas Temperature	$T^* = 1$

$$Q_e + \int_{x_e}^{x_f} h \cdot (T_x - T_s) dx = 0 \quad (1-18)$$

$$\Lambda_s = \frac{k_f \cdot \rho \cdot K(T)}{\dot{m}_s'' \cdot C_p} \quad (1-19)$$

**Table 1-3: Description of coordinate transforms corresponding to equations (1-20) through (1-24).**

Physical Parameter	Nondimensionalized Representation
$x$ – Spatial Coordinate	$x^*$ – Nondimensional Coordinate
$T$ – Temperature	$T^*$ – Nondimensional Temperature
$Y$ – Product Mass	$Y^*$ – Product Mass Fraction
$\dot{m}''$ – Mass Flux	$r^*$ – Nondimensional Mass flux

$$x^* = \frac{\dot{m}'' \cdot C_p}{k_f} \cdot x \quad (1-20)$$

$$T^* = \frac{T_x - T_o}{T_\infty - T_o} \quad (1-21)$$

$$T_s^* = \frac{T_s - T_o}{T_\infty - T_o} \quad (1-22)$$

$$Y^* = \frac{Y_x - Y_o}{Y_\infty - Y_o} \quad (1-23)$$

$$r^* = \frac{\dot{m}''}{\dot{m}_s''} \quad (1-24)$$

$$f = \frac{\int_{x_e}^{x-x_e} h \cdot A_s'' \cdot (T_s - T_x) dx}{m \cdot C_p \cdot (T_\infty - T_o)} \quad (1-25)$$

From the analytical solution for combustion involving an isothermal solid within the combustion chamber, reasoning based on mathematics may describe several important aspects of heterogeneous combustion [20, 39]: **1** Mass flow rate may greatly exceed the laminar flame speed; **2** External heat loss will cause a reduction in the maximum reactant flow rate; **3** For solid phase temperatures in excess of the temperature correspond to the maximum flow rate, mass flow increases move the flame towards the exhaust; **4** for solid phase temperatures which correspond to flow rates below the maximum flow rate, the flame position will move towards the combustion chamber inlet. Presented data from these analyses in Figure 1-11 assume a constant characteristic equivalence ratio, adiabatic flame temperature, and activation energy of the mixture.

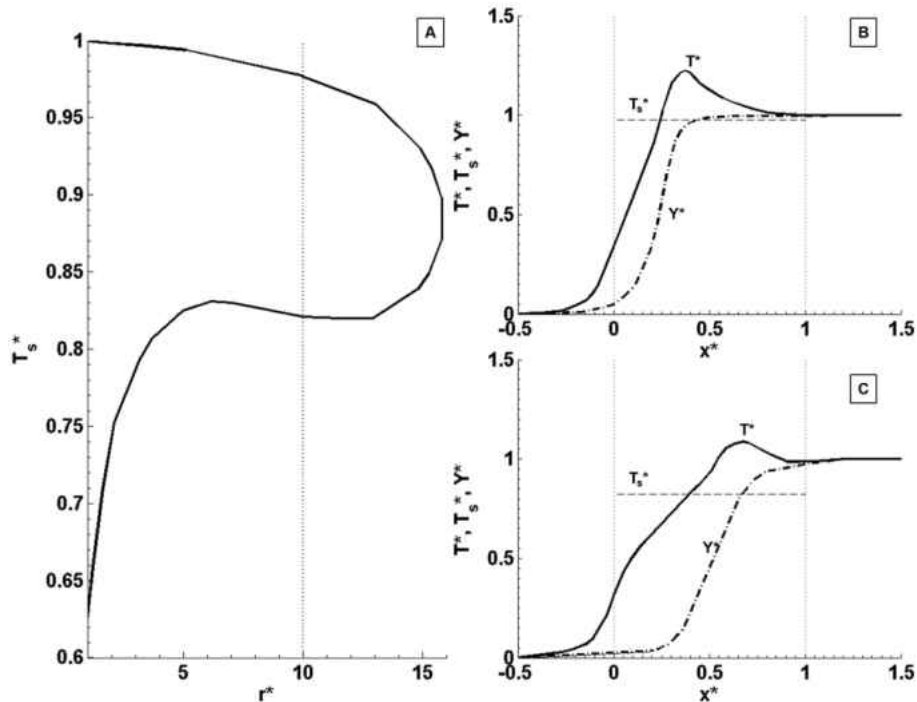


Figure 1-11: A) Solid Phase temperatures as a function of  $r^*$ . B) Upper branch reactor profile at  $r^*=10$ . C) Lower b reactor profile at  $r^*=10$ .

#### 1.2.4. Transient Behavior of Flames Within Porous Media

In heterogeneous combustion an equilibrium depicts the reactant feed rate in sync with the rate at which reactants cross the boundary into the standing flame Figure 1-12 where  $\vec{u}_w$  is the combustion wave velocity, and  $\dot{x}_o$  is the rate of change of the combustion wave front from the reactor inlet (1-26). However upon perturbations to either the flow rate, equivalence ratio, or dramatic change in external heat loss the position of the combustion wave will begin to propagate.

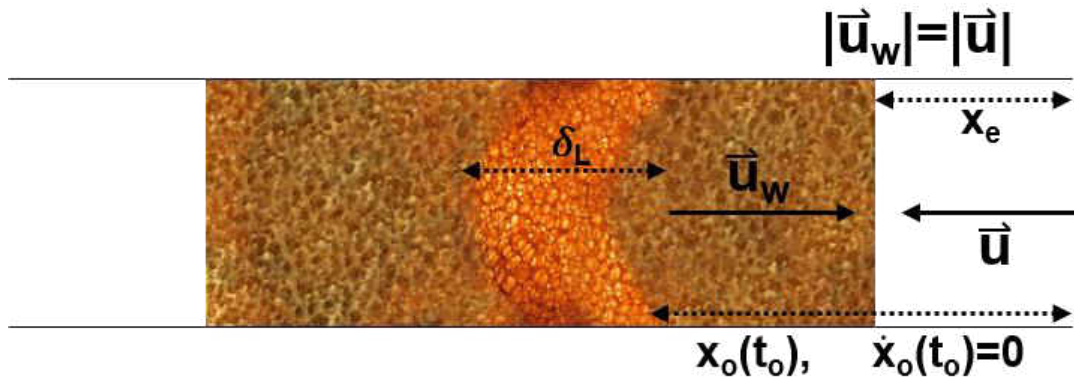


Figure 1-12: Combustion wave in heterogeneous combustion of equal magnitude

$$\dot{x}_o = \vec{u} - \vec{u}_w \quad (1-26)$$

Supposing there is some perturbation to the reactant feed rates or heat loss due to some external influence, the flame position may either proceed towards the exhaust of the combustion chamber, in the extreme case blow off; or move closer to the inlet, flashback. Such cases are presented in Figure 1-13 and Figure 1-14, respectively. For momentary disruptions to the aforementioned quantities, the flame will return to the previous equilibrium position [38]. Under such conditions when disruptions to the reactant flow rates last for some duration of time one of two possible outcomes may occur: **1**, the flame position will exit the porous media; or **2**, the flame will reach some new stable equilibrium.

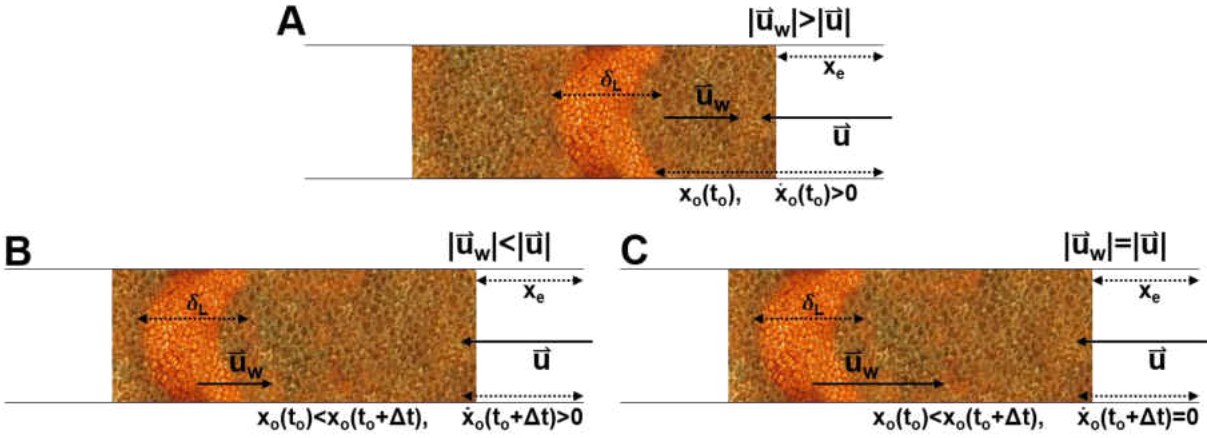


Figure 1-13: A) Conditions of a flame beginning a progression towards the exhaust. B) Unstable progression of the flame continuing to blow off conditions. C) Flame settles at some new equilibrium position within the porous media.

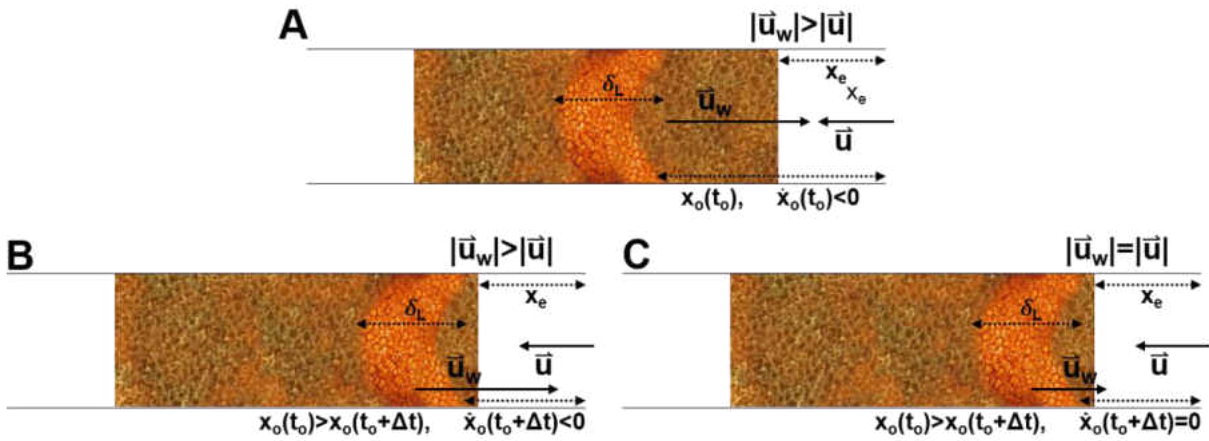


Figure 1-14: A) Conditions of a flame beginning a progression towards the inlet. B) Unstable progression of the flame continuing to flashback conditions. C) Flame settling at some new equilibrium position within the porous media.

Whenever  $\dot{x}_o \neq 0$  the burning nature of the combustion wave will vary due to thermal interactions with the solid phase [25]. When  $\dot{x}_o$  assumes a positive value, the gases are exposed to higher temperature sections of the solid phase increasing the maximum flame temperature and the reaction rate. Conversely, when  $\dot{x}_o$  assumes a negative value gasses will be subject to less

preheating and the reaction rate will diminish. As a result of changes to the reaction rate the magnitude of  $\delta_L$  is subject to change.

### **1.3. Applications of Heterogeneous Combustion**

Heterogeneous combustion has been proposed as a heat source which can replace conventional combustors used in gas turbines and as radiative emitters for combined heat and power, or space heating. However, there are also several novel applications for heterogeneous combustion which have not been observed in literature at the time of this writing include:

- Heat sources to be used with organic Rankine cycles in combined heat and power applications.
- Fuel reformers for fuel cells
- VOC Treatment device for extraterrestrial horticulture
- Gas flares at oil fields, underground mines, and chemical processing facilities
- Chemical processors for hydraulic fracturing
- Case hardening

#### ***1.3.1. Heat Source for Organic Rankine Cycle Combined Heat and Power Systems***

Rankine Cycle turbines are a mature technology, having predominantly operated on steam. However, organic compounds may also be used as the working fluid, and which is denoted as an Organic Rankine cycle (ORC)[42]. Selected working fluids for use with ORC systems may be seen in Table 1-4; from the table it may be seen the boiling temperature, critical temperature, and pressure  $T_{Critical}$  and  $P_{Critical}$ , respectively, are significantly lower than that of water.

<b>Table 1-4: Types of novel organic compounds, and water, for closed loop turbine cycles [42].</b>				
<b>Fluid</b>	<b>M<sub>w</sub></b>	<b>T<sub>BoilAtm</sub> (°C)</b>	<b>P<sub>Critical</sub> (MPa)</b>	<b>T<sub>Critical</sub>(°C)</b>
<b>Water</b>	18.02	99.97	22.064	374
<b>HC-40</b>	50.48	-24	6.681	142.95
<b>HCFC-123</b>	152.91	22.75	3.606	184
<b>HCFC-124a</b>	136.5	-12.03	3.616	122.42
<b>HCFC-142b</b>	100.5	36	4.123	136.85
<b>HFC-152a</b>	66.05	-24.2	4.52	113.29
<b>HC-600a</b>	58.12	-11.7	3.65	134.85
<b>R-401A</b>	94.44	-32.97	4.604	108.01
<b>R-401C</b>	101	-28.4	4.366	113

With such working fluids it is possible to integrate a multi stage heating system which collects heat from HVAC and other equipment within a home or industrial center with a final heating stage powered by a heterogeneous combustor operating in the super lean region to superheat the organic fluid before passing the fluid through a work extraction device and discharging the heat in a condenser to ambient temperatures.

### *1.3.2. Fuel Reformers for Fuel Cells*

Fuel cells are an advanced energy conversion technology in which electrical work is extracted through the oxidation and reduction half reactions at the anode and cathode of the cell [43]. However, most fuel cells are not capable of operating directly fuels with C-H bonds and a fuel preprocessing device is needed. As heterogeneous combustors have been shown to operate efficiently in the ultra rich combustion regime [44], they are aptly suited devices for the pre-processing of fuels with low sulfur content to enable the operation of fuel cell stacks on automotive grade fuels Figure 1-15.

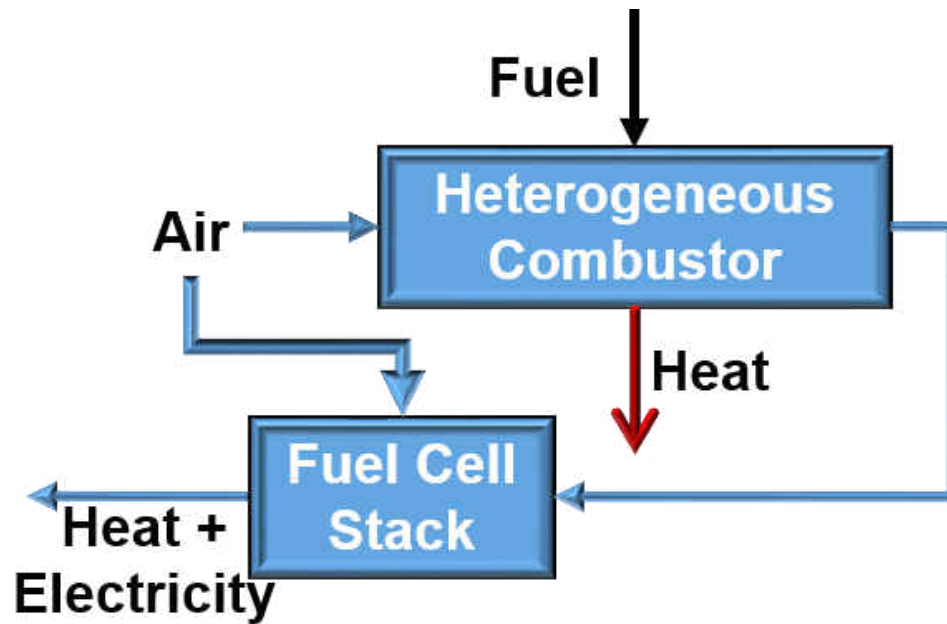


Figure 1-15: Flow Diagram for a Heterogeneous combustor to be used as a fuel reformer for a fuel cell stack

### 1.3.3. *Efficient and Clean Gas Flares*

Gas flares are often employed at chemical production facilities, landfills, and at oil wells to dispose of hazardous gasses to prevent over pressurization within a particular installation. These flares operate in such a way which combustion efficiencies are extremely low and as a result, significant amounts of only partially oxidized compounds are emitted, this may be seen in Figure 1-16. A heterogeneous combustor used in such a situation can enable the burning of such reactant feeds in a series of small reactors, where at each reactor catalysts are specifically tailored to the expected reactant group and simultaneously more air may be injected to the fluid stream, enabling a further oxidation of the reactants.

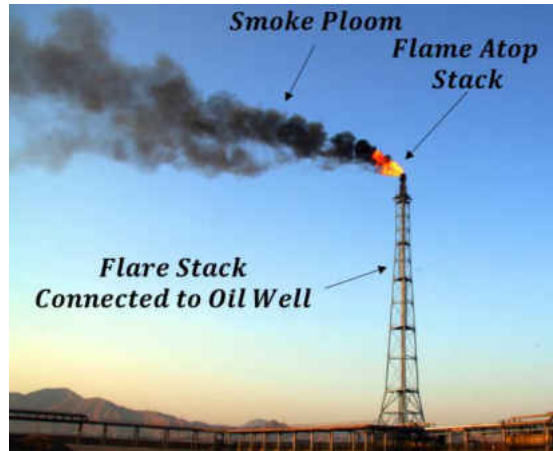


Figure 1-16: Flare stack connected to an oil field.

#### 1.3.4. Chemical Processors for Hydraulic Fracturing

Hydraulic fracturing, or fracking, is the use of water or some other fluid pumped underground to induce fractures into rock layers below a terrestrial or oceanic floor which then enables the extraction of underground oil and natural gas [45]. Often times these fracking sites will use specially designed containment ponds for the storage of fluid which has been recovered from the fracking well, these fluids may contain considerable content of gaseous hydrocarbons which will over time evolve from the fluid reservoir [46].

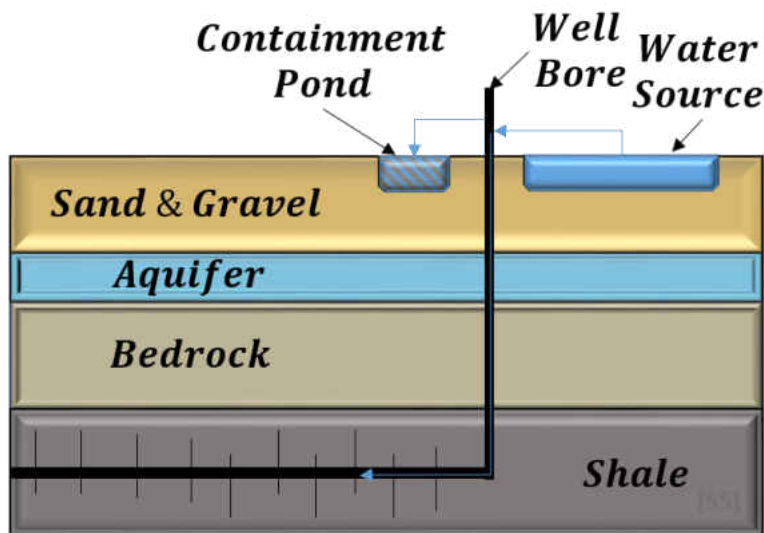


Figure 1-17: Schematic of a hydraulic fracturing well.



Heterogeneous combustion may be used in one of two ways to reduce the volatile nature of such fluid making the hauling of the fluid to an off-site treatment facility unnecessary. In the first method, a heterogeneous combustor which is placed nearby to one of such ponds may have some of the contaminated fluid injected directly to the combustion chamber, instantly vaporizing the fluids and thereby releasing the volatile compounds into the combustion chamber to be used as fuel. A second means of reducing the impact from fracking is to have a small quantity of liquid from the containment pond pumped from its reservoir to a chamber under vacuum allowing atmospheric air to enter the lower layers of fluid to draw out flammable contents from the fracking fluid prior to injecting the oxidizer into a heterogeneous combustion chamber.

#### ***1.3.5. Case Hardening***

Case hardening is a process commonly used to introduce nonmetals, commonly carbon and nitrogen, into the surfaces of metals to achieve a surface layer which has a higher hardness than the underlying metal. A heterogeneous combustor, Figure 1-18, may be used operating under a rich condition of a hydrocarbon fuel, or ammonia as fuel in combination with high pressure to produce a desired content of carbon or nitrogen in the exhaust gasses available for surface diffusion into a metal under high temperatures. A valve system may be used in conjunction to oscillate between rich combustion to maintain a thermally and chemically controlled environment for the object being case hardened.

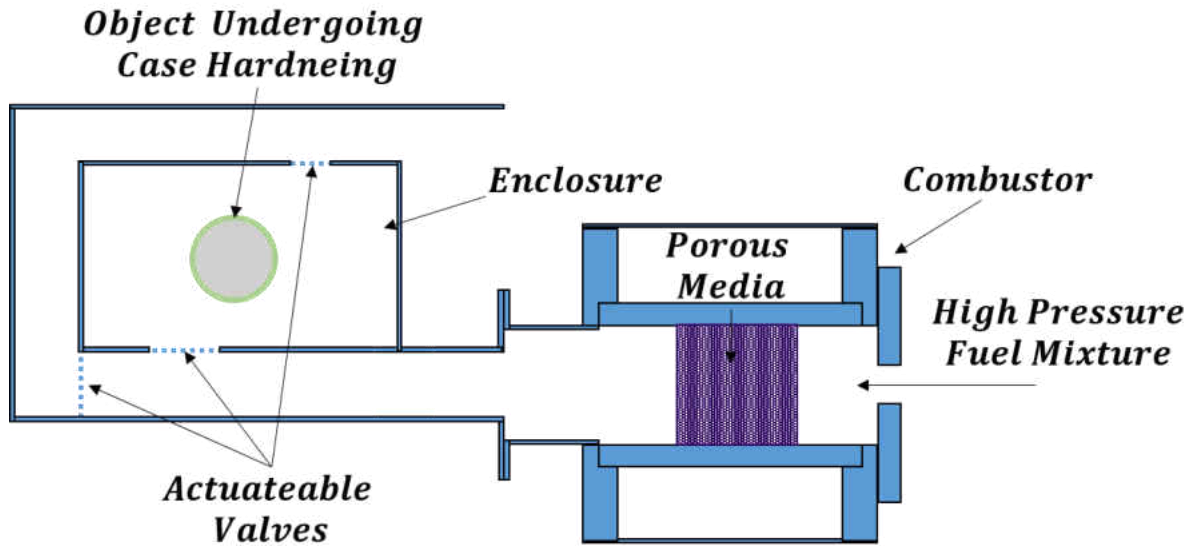


Figure 1-18: Method of case hardening using a heterogeneous combustor.

#### 1.4. Goals of Research

The goals of this research work are threefold

- Demonstrate the design of a flow stabilized heterogeneous combustor.
- Demonstrate the utility of acoustic spectroscopy as a characterization technique to understand phenomena occurring within heterogeneous combustion.
- Examine and characterize performance of heterogeneous combustion utilizing substrates of different chemical composition and with various surface catalyst coatings.

## 2. LITERATURE REVIEW

Heterogeneous combustor design is strongly varied amongst literature, and this is in part due to the limited research in design investigations and existing applications for heterogeneous combustors. No single combustor design is able to provide unlimited application, and while all designs exhibit advantages there are several governing principles which should be considered in the preliminary phases of design. While combustor design is an iterative process, a simple scheme for designing a heterogeneous combustor should consider concepts presented in Table 2-1, and consist of the following considerations sequentially: **1** ignition, **2** intended application, **3** available fuel, **4** required thermal output, **5** emissions limitations, and **6** everything else. Example designs for heterogeneous combustors are available in literature, some of which are presented in Figure 2-2 through Figure 2-6.

**Table 2-1: Design considerations of a heterogeneous combustor.**

- |                                |                                |
|--------------------------------|--------------------------------|
| • Fuel Mixing Mode             | • Fuel(s) and Oxidizer(s) Used |
| • Desired Burning Mode         | • Spatial Requirements         |
| • Pre Heating                  | • Operational Metrics          |
| • Operating Static Pressure    | • Operational Lifetime         |
| • Maintenance                  | • Discardable Components       |
| • Sealing                      | • Emissions                    |
| • Ignition Method              | • Ignition Location            |
| • Plant Integration            | • Ambient Conditions           |
| • Measurement and Health Check | • Cost                         |

Ignition is the introduction of a “*spark*” to the unlit fuel mixture which induces the self propagation of the flame. Ignition may be assisted by a choke, or fuel mixture enrichment circuit which raises the equivalence ratio to just greater than one [47]. Common ignition methods are presented in Figure 2-1. High voltage discharges across a pair of electrodes exposed to premixed fuel and air [48], an external pilot flame [49]. Other techniques of ignition employ

photochemical reactions caused by narrow bandwidths of light focused at a small volume to induce dissociation of stable molecular species [50] and the ignition of a flow by a heterogeneous catalyst [51].

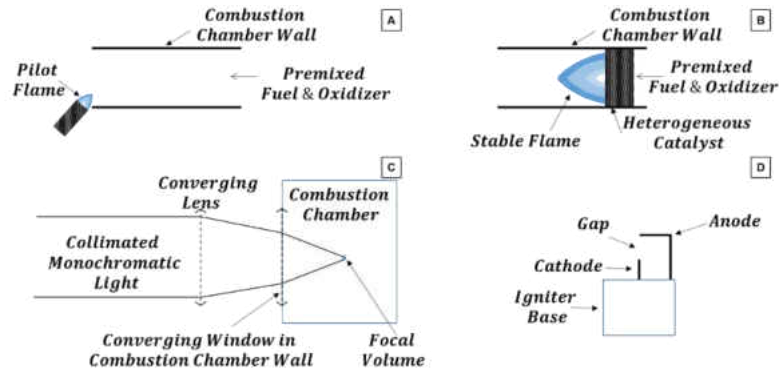


Figure 2-1: A) Ignition by external pilot flame. B) Ignition of a reacting flow by heterogeneous catalysis. C) Laser ignition. D) Conventional spark ignition.

Ignition of the flow within a combustor is necessary for the combustor to be useful, within Figure 2-2, an ignition device in the form of a spark plug within the combustion chamber ensures a reliable means of starting the combustor. The combustor also features an integrated finned heat exchanger to extract thermal energy from the exhaust gasses and water cooling around the combustion chamber to regulate temperature.

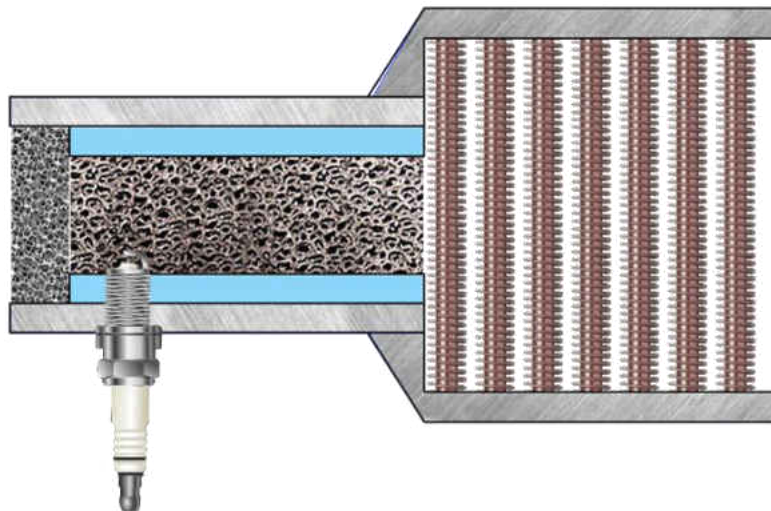
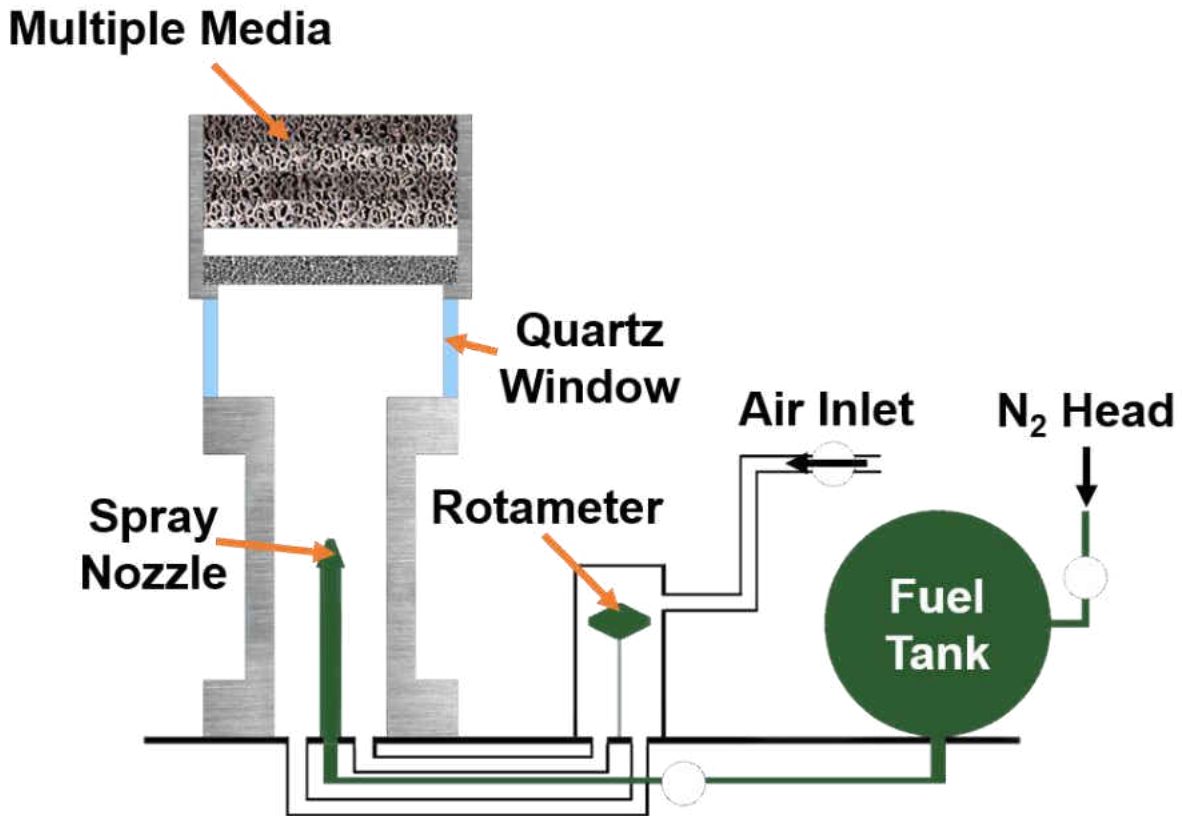


Figure 2-2: Heterogeneous combustor with a spark plug igniter. [52]

The flow of liquid fuel into a heterogeneous combustor adds significant complexity to the operation in a scientific manner. Observing the schematic, Figure 2-3, it can be seen to meter the flow of liquid fuel, nitrogen is used to induce a hydraulic head to a liquid fuel tank. The liquid fuel is then advanced into the combustion chamber using a spray nozzle.



*Figure 2-3: Spray nozzle liquid fueled heterogeneous combustor [53].*

Heterogeneous combustors typically are arranged as a straight flowing tube device. For combustors which are capable of providing significant thermal output, combustor design may make use of shapes aside from the linear profile seen in other combustors enabling a smaller overall footprint. Such a combustor which incorporates two dimensions for the flow path is presented in Figure 2-4.

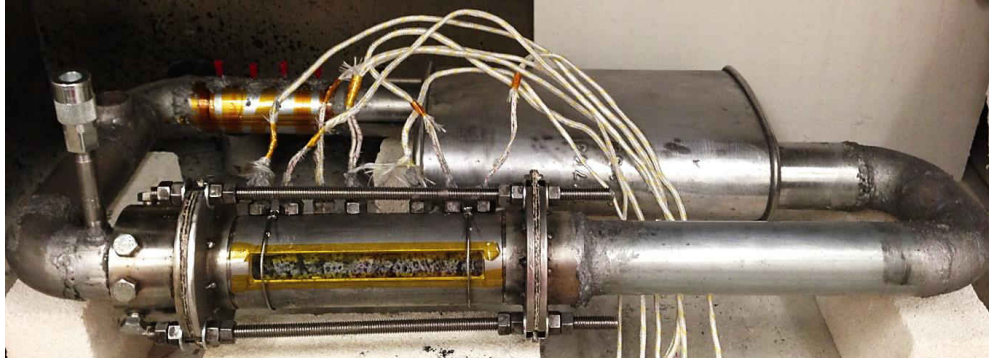


Figure 2-4: Bi-fuel loop shaped heterogeneous combustor [54].

A combustor intended to provide portable combined heat and power is presented in Figure 2-5 where the housing for the combustion chamber features a mounting location for a thermoelectric generator. From this combustor, heat from the exhaust may be used for space heating applications while the device is simultaneously able to provide electrical energy.

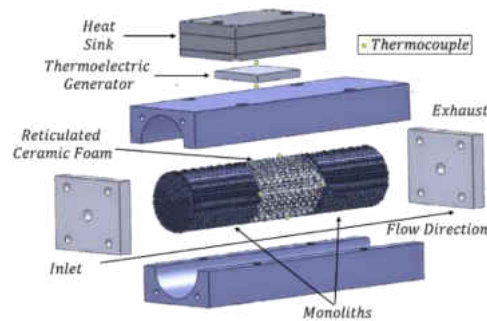


Figure 2-5: Heterogeneous combustor for combined heat and power [28].

Some combustors which are more complex may incorporate multiple stages of reactant delivery and specific attention to the expansion of gasses within the flow channel prior to the combustion chamber. One such example is presented in Figure 2-6. A primary fuel and air inlet before the first combustion media provides a large fraction of the total reactant flow. A second stage reactant delivery is then injected following the first stage in which a small fraction of fuel and air are used to release additional heat and provide another means to control pollutant formation.

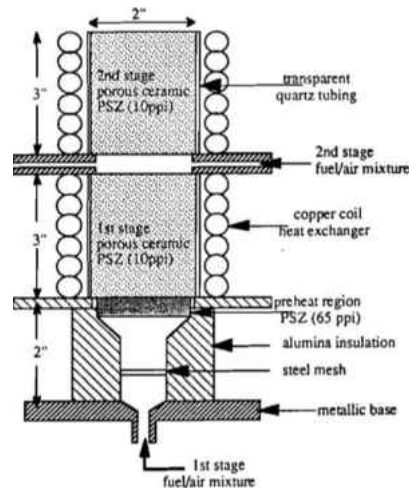


Figure 2-6: Multistage heterogeneous combustor using zirconia media [55].

With such design considerations, and observation of the presented burners, it is necessary to use engineering principles, modeling simulations, and previous combustor design experience; to design a heterogeneous combustor. While novel considerations will always be explored and discussed in literature, heterogeneous combustor design should consider the method by which fuel will be delivered to the combustion chamber 2.1, specifics of the combustion chamber 2.2, and the instrumentation which is used to analyze combustor operation 2.3.

### 2.1. Reactant Delivery and Mixing

As explained in **Error! Reference source not found.** for a flame to exist within a combustion chamber, oxidizer and fuel must be delivered to the combustion chamber. A total pressure gradient must exist across the combustion chamber in which the total pressure at the combustor inlet exceeds that of the outlet. In commercial combustors the necessary pressure rise is achieved using compressors and ducts with variable area cross sections [56]. In addition to a pressure gradient, proficient reactant mixing, and distribution must also occur with minimal losses in total pressure.

Methods of reactant delivery and mixing will impose strict constraints on the performance of the combustor [57]. Ultimately, the engineer must determine the specifics of such methods and

often these designs are proprietary [58]. In heterogeneous combustors with variable degrees of premixing, a monotonically increasing correlation was found between the degree of fuel premixing and thermal output while an inverse correlation was found between the extent of premixing and emissions concentration [59] and thus a premixed fuel/oxidizer scheme is often preferable when considering efficient operation.

For liquid fuels, there are additional considerations which must be addressed as the phase dissimilarity in fuel and oxidizer may greatly affect combustion. If fuel droplets exist upon entrance to the combustion chamber, initiation reactions and burning are limited to the small volume surrounding the liquid where oxidizer may diffuse amongst vaporized fuel, Figure 2-7 [60]. Consequently requiring longer residence times within the combustion chamber to completely oxidize the reactants. In cases where fuel droplet diameter exceeds a critical value the formation of soot in a heterogeneous combustor is even possible [61].

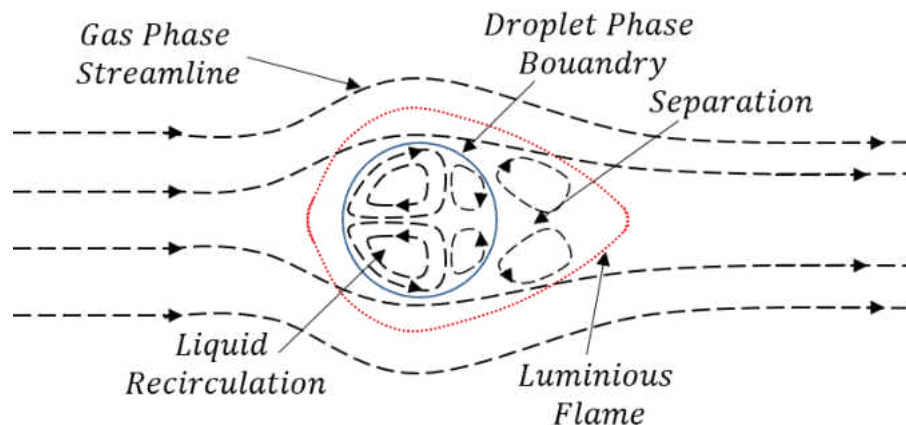


Figure 2-7: Combustion of a liquid fuel droplet in a laminar gas flow [60].

While some heterogeneous combustors have been designed with crude liquid fuel delivery schemes in which a gravity assisted delivery of kerosene through a syringe [62]. To ensure a single phase mixture or finely dispersed aerosol exists upon entrance to the combustion chamber when using liquid fuels, energy must be introduced to the fuel in order to vaporize fuel droplets. Several



techniques have been used to achieve fuel vaporization, including pressurized sprays [53], ultrasonic assisted vaporization [63], injection of the fuel into a supercritical environment [64], or preheating of the fuel prior to entrance to the combustion chamber [65]. Combinations of these and other methods may also be used to vaporize liquid fuel.

With a stressed importance on mixing and delivery, the subsequent consideration is the flow rate and distribution of reactants through the combustor. As various fuels will require different stoichiometric ratios of oxidizer and industrial combustors routinely feature oxygen enrichment or water injection [66, 67] a convenient method for determining the magnitude of a heterogeneous combustor is to account for the amount of air which is delivered to the combustion chamber. A proposed convention of combustor scaling using air flow rates is presented in Table 2-2.

**Table 2-2: Heterogeneous combustor sizing by air flow rate SLPM.**

• Nano	• $x < 1$
• Micro	• $1 < x < 15$
• Mesio	• $15 < x < 100$
• Macro	• $100 < x < 1000$
• Industrial	• $1000 < x$

## **2.2. Combustion Chamber**

The combustion chamber of a heterogeneous combustor must house the flame in a manner which provides safe and reliable operation while simultaneously promoting efficient operation.

2.2.1 Discusses the combustion chamber inlet plenum. 2.2.2 Gives an overview of selection principles pertaining to composition and dimensions of the reticulated foam, and 2.2.3 discusses the design of the chamber housing borrowing design considerations from conventional combustion chambers.

### **2.2.1. Inlet Plenum**

Assuming an efficient means of delivering reactants to the combustion chamber has been implemented, the reacting flow must then be distributed across the combustion chamber cross section. An inlet plenum is a device which enables a smooth transition in the flow profile between the combustion chamber and the narrow diameter channel which supplies premixed reactants to the combustion chamber. In conventional combustors, plenum design is used to maintain a stable flame, and control the position of the flame within the combustion chamber [68-70]. As with conventional combustion, the fluid dynamics of a heterogeneous combustor play an important role in determining the characteristics of combustion. Characterization of flow fields is an expansive, with several optical and numerical techniques used to accurately characterize and design this crucial component [57].

As flame position within the combustion chamber is dependent upon design of the inlet plenum, it is paramount to design a plenum which produces a known velocity and pressure profile of the flow. When designing an inlet plenum it is necessary to consider the composition and velocity of mixtures which are introduced to the combustion chamber, as changes in Reynolds Number produce characteristic recirculation regions for given plenum geometries, Figure 2-8, [71]. For inlets which deliver gasses above local sonic velocities, other considerations are needed [72]. Plenum designs may also be used to control flow of fluid in the azimuthal direction within the combustion chamber, such azimuthal swirl may enable a reduction of combustion chamber volume for a fixed reactant flow rate and mixture composition [73].

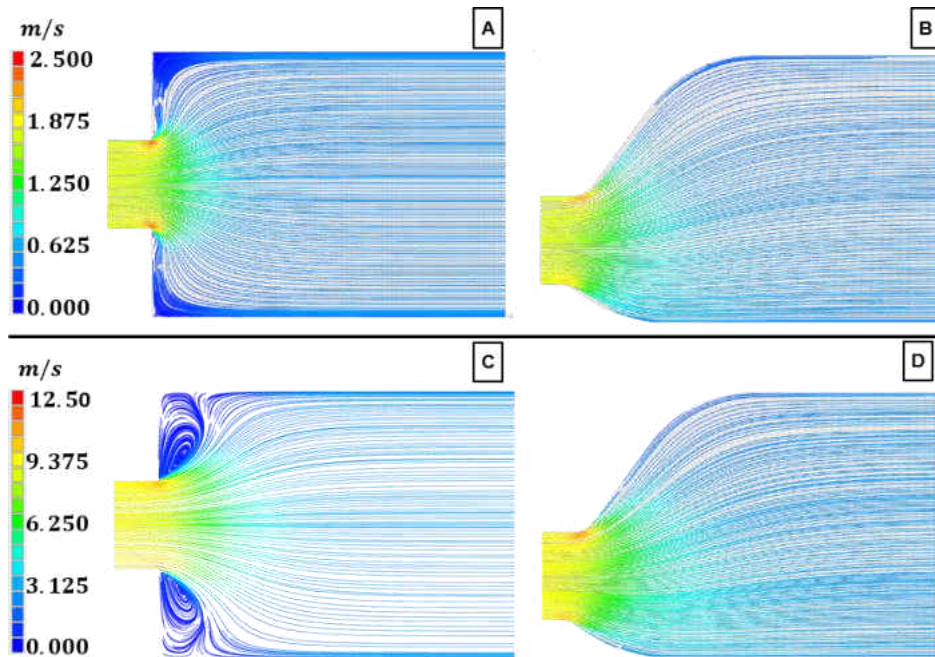


Figure 2-8: Flow of air at 300K and 1 atm through 2D Ducts corresponding to Reynolds numbers of (upper) 4000 and (lower) 20000.

As there is limited penetration of heterogeneous combustion in industrial applications at the time of writing, the available literature presenting designs of heterogeneous combustors is limited to nano~mesio scale heterogeneous combustors seen in research emphasizing simplicity and ideal boundary conditions. A common feature of research combustors is the implementation of a ceramic monolith, Figure 2-9, within the plenum. The monolith conditions the flow to exhibit a near uniform velocity profile across the combustion chamber cross section.

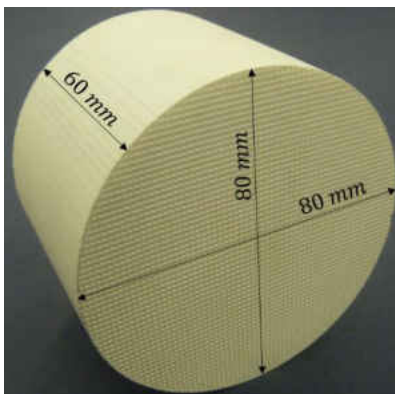


Figure 2-9: Monolith structure featuring many small flow channels.

While these monoliths are able to also act as a flashback arrestor due to the high surface to flow cross section area, at appreciable flow rates, a significant amount of shear force will be exerted on the fluid passing through the structure, inducing a total pressure drop [28, 74, 75]. Additionally studies have shown a stabilization effect at the interface between ceramic components [53], and thusly monoliths have pronounced effects on the observed phenomena and range of stable conditions at which the combustor may operate. For combustors which do not feature a monolith at the combustion chamber inlet, the inhibition of the flame proceeding towards the inlet indefinitely may be controlled by “high” flow velocities.

### ***2.2.2. Reticulated Foam Properties***

From 1.2, it has been shown the emplacement of a solid phase has pronounced effects on combustion through enhanced dispersion and heat recirculation. The use of a reticulated foam is the novel foundation of heterogeneous combustors and thusly attention should be paid to its selection criteria. Several manufactures are able to provide reticulated ceramic foam of various composition and dimensions.

Selection of a reticulated foam requires many considerations. It is important for the foam to remain a solid phase and if no coatings are used chemical stability under operating conditions, mandating the use of refractory compounds. Properties for common materials are presented in Table 2-3 where  $T_{max}$  is the maximum stable temperature,  $R_T$  is thermal shock resistance, and  $\alpha$  is the linear coefficient of thermal expansion. While many vendors are able to provide reticulated foams, only certain pore densities may be available and the dimensions of the foams must be within ability of the manufacturer.

**Table 2-3: Properties of selected refractory ceramics [76].**

	Al <sub>2</sub> O <sub>3</sub>	SiC	ZrO <sub>2</sub>
$T_{max}$ in air (°C)	1900	1600	2300
$k$ ( $\frac{W}{m \cdot K}$ ) at 1000°C	5~6	20~50	2~4
$\epsilon$ at 1727°C	0.28	0.90	0.31
$\alpha$ ( $10^{-6} \cdot 1/K$ ) over 20~1000°C	8	4~5	10~13
$R_T$ ( $10^{-3} \cdot 1/W$ )	3	23	1

Within literature a range of pore densities are used, and the common indication of pore density is *pores per inch ppin* and ranges from 10~45 ppin [77]. Pore size exhibits pronounced effects on both dispersion and heat transfer within the flow [17]; for small pore sizes the radiative heat transfer becomes limited though intrafacial heat transfer between the gas and solid phase increases as well as conduction within the solid phase. Based upon expected flow rates and mixture heating values, considerations may be taken to size the pores of the media accordingly.

After a material has been identified, features of the solid must be evaluated. Quality porous media should contain little to no clogged pores, invariant pore clustering, and maintain sufficient structural integrity. For heterogeneous combustors for which catalysts will be employed, it is also advisable to determine the nominal size and distribution of structural features of the surface of the solid phase. Using BET techniques, specific surface area of solids may be experimentally determined through the adsorption of gas on a solid surface [78].

Across literature, reticulated ceramic foams have been used in heterogeneous combustors having either rectangular or circular cross sections, and various lengths [17]. While design calculations are paramount, it is difficult to ascertain the location of the flame position from calculations alone. Foam depth is the single most important consideration for determining if the flame will maintain a position within the foam [17]. A longer foam will provide a larger range of stable equivalence ratio and flow rate combinations but will also induce significant thermal losses

from the combustion byproducts if the foams length is excessive. Therefore careful selection should be considered when determining the depth of the porous bed.

Regardless of the cross section's shape, the cross section area will ultimately determine the expected maximum mass flow rates and the ability of the solid phase to radiate heat along its axis. To appropriately size the porous media cross section consideration of the fuels used, static pressure and the expected range of equivalence ratios must be considered as these parameters influence the laminar flame speed. Determination of rough characteristics should be implemented using reactor models available in literature [79].

### ***2.2.3. Chamber Housing***

Combustion chamber housings must withstand the intense conditions of combustion. Across literature it is common to see steels and ceramics which may be transparent enabling optical access [80, 81]. The foremost importance of the combustion chamber is to enable an access method for ignition. The chamber housing must also provide a satisfactory means reaction containment. In combined heat and power units the housing may also simultaneously enabling use of heat produced from the combustion chamber for electricity conversions and other processes [82, 83].

Combustion chambers must last for a sufficient designated life, for engines which have lifetimes of only a few minutes this is obviously a different consideration than those used in turbine power plants which must last for years [84, 85]. Considering combustion chambers which must have a “*longer*” lifetime, the combustion chamber is designed in such a way that provides stable housing of the flame while maintaining its structural integrity.

These “long” life combustion chambers in conventional combustors are often coated with highly corrosion and heat resistant thermal barrier coatings which act to reduce the temperature of the load bearing components of the combustion chamber [86]. Active cooling in the form of film cooling is also used to provide a buffer layer of inert gasses between the flame and exposed wall of the combustion chamber [87]. Additional convective cooling may be also used on the exterior of the combustion chamber to remove excess heat [85]. Chamber housings may also actively control combustion through exhaust gas recirculation and staged reactant introduction [55]. All of these techniques of control and design may be considered in heterogeneous combustion chamber designs.

### **2.3. Instrumentation and Measurements**

Instrumentation and diagnostics for heterogeneous combustion are convoluted. The nature of the solid phase inherently imposes difficulties in acquiring accurate measurements which derive from only one phase and simultaneously the inclusion of measurement techniques disturbs the nature by which combustion occurs [19]. Even with such complications from the porous media, measurements may be taken. The most common method by which data is collected for heterogeneous combustors is through thermocouples within the combustion chamber. Though optical, acoustic, pressure, and chemical analyses are also seen in literature [81, 88].

#### ***2.3.1. Temperature Measurements Using Thermocouples***

Within literature, thermocouples are the most common means of measuring temperature within heterogeneous combustion. Thermocouples measure temperature through the thermoelectric effect which is known to occur in a particular quantity upon the junction of two dissimilar alloys; for K-type thermocouples these metals are alumel (red wire) and chromel (yellow wire) alloys. However

the use of thermocouples as a temperature measurement device is prone to error [89]. Heat transfer between the thermocouple and the surroundings result in the temperature recorded not inherently being the temperature which is desired. Referring to Figure 2-10, a thermocouple exposed to some flow with a *free stream temperature*  $T_\infty$  and *free stream velocity*  $\vec{u}_\infty$  is subject to convection. Radiative heat exchange with nearby surfaces and conduction through the thermocouple leads also simultaneously occur. As a result of the multi-mode heat transfer, the recorded temperature is a combination of gas & solid phase temperatures with some offset accounting for conduction from the thermocouple bead.

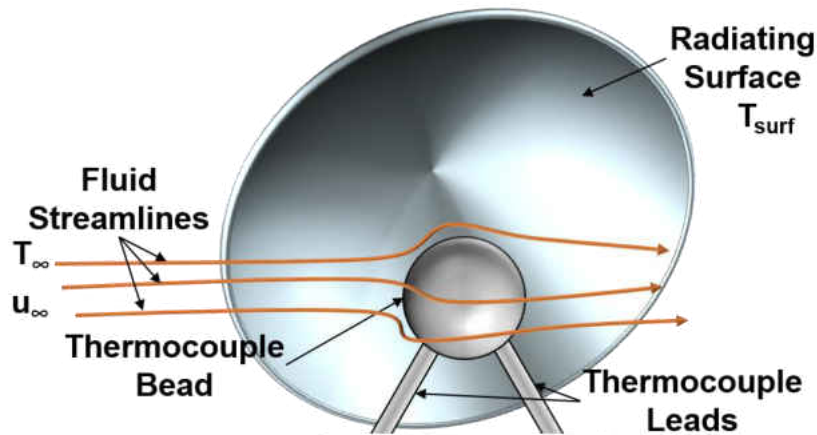


Figure 2-10: A thermocouple bead placed in a flow with some prescribed conditions while simultaneously being exposed to a surface.

### 2.3.2. Photographic Imaging

While it is the most fundamentally simple means of observation, a photograph is able to reveal substantial information. Photographing a hot object may even reveal temperature distributions along the surface as all objects emit radiation based on the temperature of their surface. A fraction of this energy is transmitted across wavelengths in the visible spectrum; hence as to why objects become visible when at a certain temperature range. For a heterogeneous combustor a simple optical system may resolve two-dimensional spatial temperature profiles when a calibration source



is used [90]. To consider a photographing technique for scientific observations in heterogeneous combustion aside from optical access, the only necessary component of understanding is that of the emission of thermal radiation.

Thermal radiation is an expansive subject and for further information textbooks are available [91]. The electromagnetic spectrum is broken into several ranges of *wavelengths*  $\lambda$ . Wavelengths may also correspond to different *wavenumbers*  $\bar{\nu}$  or *frequencies*  $f$  of light through relations (2-2) and (2-3).

$$c_0 = 299\,792\,458 \text{ (m/s)} \quad (2-1)$$

$$f = c_0 / \lambda \quad (2-2)$$

$$\bar{\nu} = 1 / \lambda \quad (2-3)$$

Objects which are perfect spectral emitters and absorbers are termed blackbodies. Blackbodies exhibit radiative properties of equal intensity which is independent of direction from the surface normal. The *Hemispherical Spectral Emissive Power*  $e'_{b\lambda}$  of intensity is presented as equation (2-6), where  $C_1$  and  $C_2$  are empirically derived constants [91]. Level curves of which across several temperatures are presented in Figure 2-11

$$C_1 \equiv 0.595\,521\,97 \cdot 10^8 \left( \text{W} \cdot \mu\text{m}^4 / \text{m}^2 \cdot \text{sr} \right) \quad (2-4)$$

$$C_2 \equiv 14\,387.69 (\mu\text{m} \cdot \text{K}) \quad (2-5)$$

$$e'_{b\lambda}(\lambda, T) = \frac{2 \cdot C_1}{\lambda^5 \cdot \left( e^{C_2 / \lambda \cdot T} - 1 \right)} \quad (2-6)$$

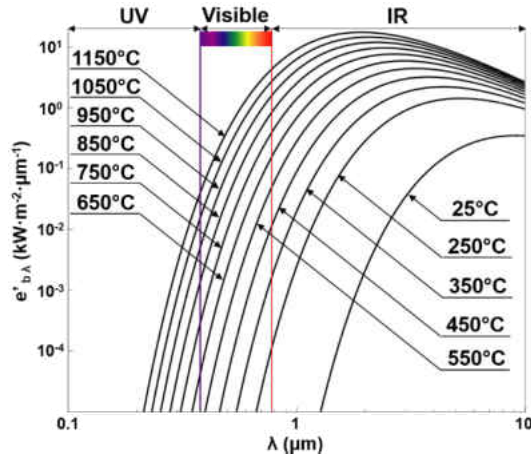


Figure 2-11: Level curves of hemispherical black body emissive power.

From observation of Figure 2-11, it is seen there is an increasing emissive power with temperature, coupled with a shift in the peak intensity to shorter wavelengths. For solid objects across the temperature range of the porous media used in heterogeneous combustion, there is a monotonically increasing fraction of radiation emitted in the visible spectrum with increasing temperature. By placing a charge coupled device or other optical detector in a line of sight with the porous media, temperature of the solid phase may be analyzed on a two dimensional plane by correlating intensity of [R G B] color values to a black body at prescribed temperature.

### 2.3.3. *Ex-Situ Gas Chromatography*

The most common form of chemical species analysis used in heterogeneous combustion is through the analysis of exhaust gasses by a gas chromatograph or GC. Gas chromatography is a means of separating components of a mixture by molecule type with the purpose of obtaining information about the concentration and types of molecules within the mixture [92]. GC's are comprised of three primary components: **1** a sample collection device, **2** the column, and **3** the detector.

A flow schematic of a Dual-Column GC is presented in Figure 2-12. Notice the use of carrier gas, helium, which is used as both a “reference” gas and as an inert environment to protect the detector from oxidation. For this GC, the carrier gas which is always flowing through the sample columns is used to supplement the flow which is delivered from the sample injection ports.

The sample collection device is responsible for introducing the test mixture to the GC. For gas samples, it is commonplace to observe a sampling valve which is a mechanical device which directs the sample into the GC only at desired times. With the use of a mechanical valve, a pressure gradient is required to force the sample from the sample holder into the GC. In some experimental systems, a gas sample storage tank may be used to provide time averaged samples of exhaust gasses for analysis [81]. A typical diagram of such valve sold under the trade name of a Valco-valve, is pictured in Figure 2-13.

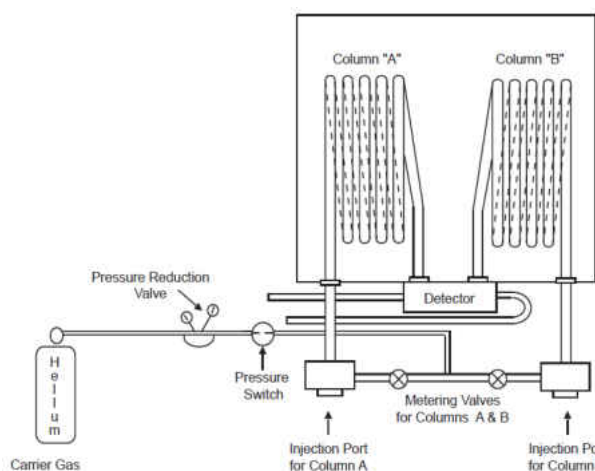


Figure 2-12: Diagram of a two Column Gas chromatograph.

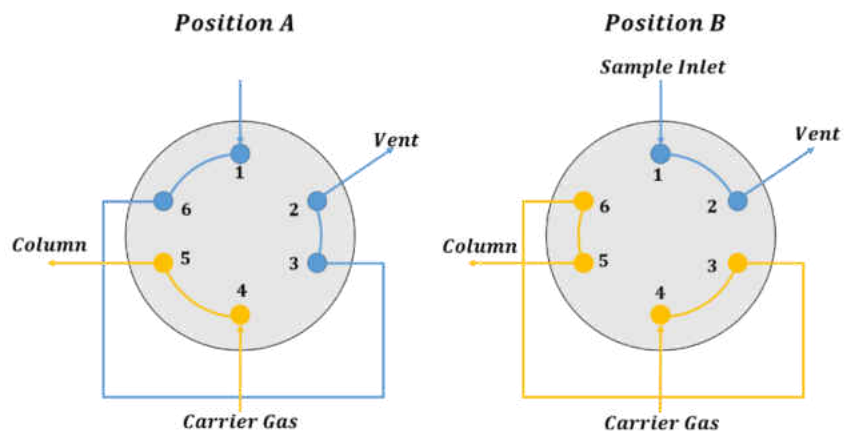


Figure 2-13: Flow schematic diagram of a Valco-valve.

The column used in a GC is responsible for separating components of the sample. A GC column is a long enclosed flow channel with a solid phase which the sample flows through. Molecular components exhibit different viscosities and thus through molecular interactions with the stationary phase the components of the sample may be separated out [92]. Specifics of the column's stationary phase composition will determine what compounds are able to be separated by the column.

Lastly it is the detector which is able to identify the compounds. While there are a plethora of detectors, the most common detector is a *thermal conductivity detector TCD* for which a schematic is placed in Figure 2-14. TCD's are most commonly used for the analysis of light and permanent gasses [92]. A TCD is a nondestructive detector, preserves the sample, where a Wheatstone bridge, with some constant voltage or constant current source used to heat resistors exposed to the flow, referred to as filaments. The balanced current or voltage between the two legs of the bridge is then monitored. A signal arises on a TCD when gasses passing over the filaments exhibit a thermal conductivity which differs from the reference gas flow. Select gas thermal conductivities are presented in Table 2-4.

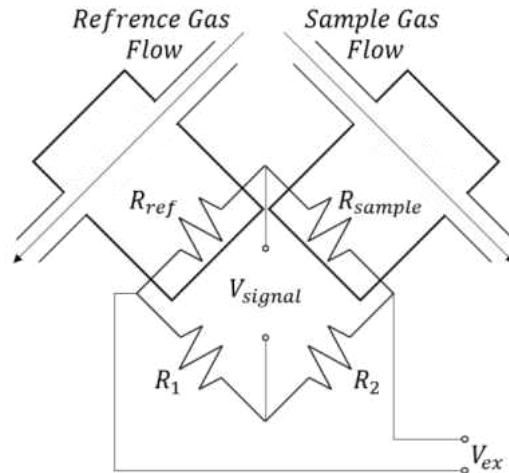


Figure 2-14: Diagram of a TCD detector.

Table 2-4: Thermal conductivities of select gases at 400 K [92].

Gas	$k_f (W/m \cdot K)$	Gas	$k_f (W/m \cdot K)$
$H_2$	0.230 4	$NO$	0.033 1
$CH_4$	0.049 1	$N_2O$	0.026 0
$NH_3$	0.037 4	$CO$	0.032 3
$O_2$	0.033 7	$H_2O (g)$	0.027 1
$N_2$	0.032 3	$CO_2$	0.025 1
$Ar$	0.022 6	$He$	0.190 6

#### 2.3.4. Acoustic and Pressure Measurement Techniques

Other techniques of measurement of combustion characterize the resonance modes, which are characterized by the formation of vortical flame structures of a characteristic pattern, by observing pressure and acoustic variations [93]. The characterization of these resonance modes is important as resonance can cause the flame to extinguish, or worse cause catastrophic failure of the combustor [94]. These vortical structures, or instabilities within the flame may be characterized using acoustic signals [95]. Acoustic signals propagate as waves through isotropic medium [96]. Analyzing only a single point in space the amplitude of the *deviation from the time averaged absolute static pressure* is  $\Delta P$ , (2-7) which is comprised of many individual waves in unison each with *their own amplitude of variation  $p_n$ , frequency  $f_n$ , and phase  $\Phi_n$* .

$$\Delta P(t) = \sum p_n \cdot \sin(2\pi f_n \cdot t + \Phi_n) \quad (2-7)$$

However, the collection of an acoustic signal must take into account: the emission source, receiver, and environment through which the acoustic wave will propagate. Within

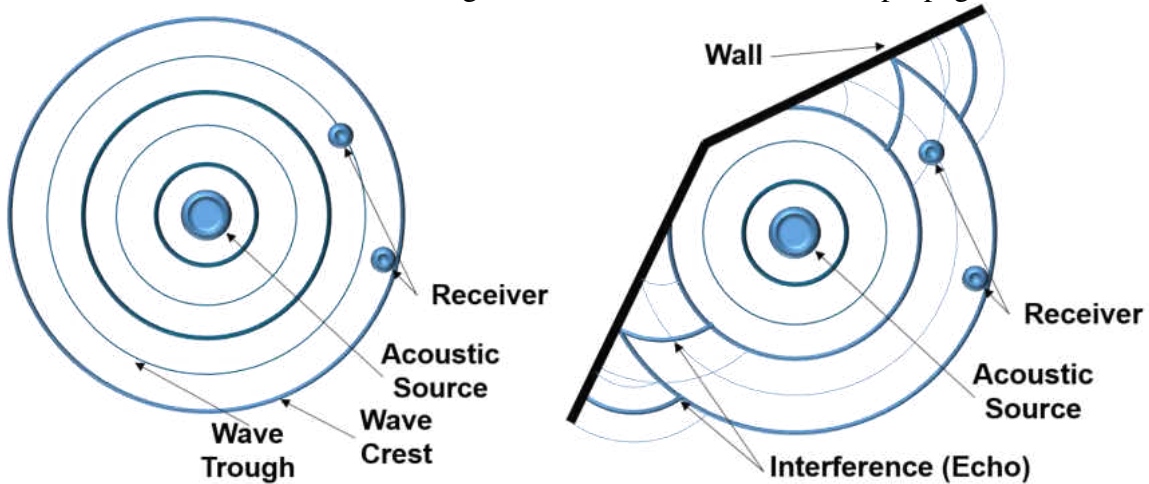


Figure 2-15 a wave propagating freely through a real isotropic medium will only be attenuated as the wave propagates from the source, receivers which collect the signal will collect unique signals with phase and amplitude, for a given frequency, a function only of the path by which the waves travel from the source. Conversely, if there is a nearby object which causes a reflection of the wave, stacking of the original wave and the reflection of the original wave from the wall will cause interference in the form of echo. As a result, the receivers which were placed at various locations relative to the source will also exhibit a difference in the collected signal, due to the quantity of interference collected by each wave.

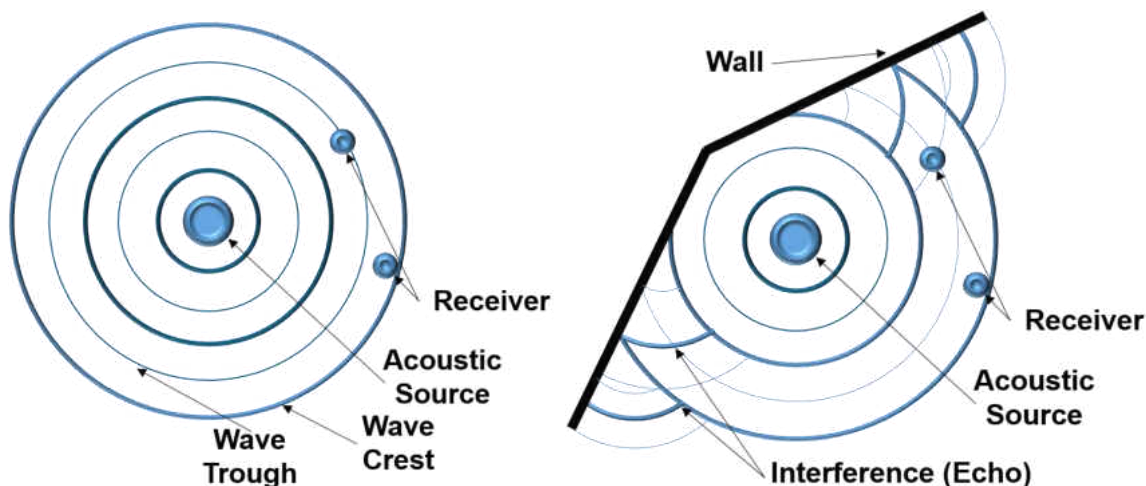


Figure 2-15: Acoustic wave propagating in an isotropic medium with no interference from the surroundings or receivers. Versus an acoustic wave propagating through an isotropic medium with interference in the form of echo due to the interaction of the wave with the wall.

By analyzing time series data collected from acoustic receivers in the frequency domain, via a Fourier Transform and relating the signal to other measurement devices. It is possible to characterize the amplitude of given frequencies of an acoustic signal enabling subsequent correlations of the acoustic signal with phenomena occurring during combustion.

#### 2.4.Heterogeneous Catalysis

Catalysts are inorganic compounds which lower the necessary activation energy of chemical transformations [97]. A catalyst which is in a phase is dissimilar to that of the primary reaction channel is heterogeneous. While heterogeneous catalysis may be applied to a broad spectrum of applications ranging from aramid production [98] to water purification and pharmaceuticals [99, 100]; within the scope of this work catalysts are used to assist in the oxidizing and/or reducing reactions of species formed during the combustion of methane.

While having understanding of a simple mechanism describing the adsorption and desorption of an adsorbate from the catalyst is necessary, there is still the chemical phenomena of what happens between adsorption and desorption. For adsorbates which have formed a bond on the

surface, the adsorbate may: *1* dissociate on the catalytic surface, *2* react with gas phase species, *3* react with other surface species, *4* return to the gas phase, or *5* in the case of a strong bond deactivate the catalyst site [101]. It is from these aforementioned possibilities which the complex reaction mechanisms of heterogeneous catalytic reactions may be derived.

#### *2.4.1. Substrate Reactivity*

Within the literature, a broad variety of solid media have been studied as a porous support material for heterogeneous combustion. Porous ceramic medias comprised of materials such as  $\text{Al}_2\text{O}_3$  [52],  $\text{ZrO}_2$  stabilized with  $\text{CaO}$  [102],  $\text{MgO}$ ,  $\text{Y}_2\text{O}_3$  [53], zirconia toughened mullite [103],  $\text{SiC}$  [104], or  $\text{SiSiC}$  [80], have been implemented as flame holders to enhance combustion. Of the aforementioned media, it has been established that  $\text{Al}_2\text{O}_3$  ceramics provide a catalytically inert surface [28], and in this case the media surface does not contribute to the chemical reaction pathways involved in the combustion process but simply serves as a means to store and redistribute heat within the flame enabling: higher net reaction rates, an elongated flame, and improved flame stability [38]. However, a catalytically active ceramic media is of interest for heterogeneous combustion as a catalytically active surface can enable additional chemical reaction pathways, facilitating increased combustion temperatures, lower light off temperatures, and reductions in the concentration of undesired exhaust gas species [75, 105, 106]. It was established that  $\text{SiC}$  and  $\text{ZrO}_2$  porous ceramic might possess catalytic activity toward methane combustion within porous media and a number of research papers were published with performance results which suggest that both  $\text{SiC}$  and  $\text{ZrO}_2$  based ceramic surfaces promote combustion and are active participants in the combustion process [107-109].



#### 2.4.2. Cerium Oxide Based Catalysts

CeO<sub>2</sub> based ceramics are well known and important catalysts for the oxidations of hydrocarbons [110]. The catalytic behavior may be attributed to the ceria lattice, which contains a high concentration of highly mobile oxygen vacancies and can therefore act as a local source or sink for oxygen involved in combustion reactions taking place on the ceria surface [110, 111]. The doping of CeO<sub>2</sub> with Gd<sub>2</sub>O<sub>3</sub> generates a significant number of oxygen vacancies presented by defect formation reaction  $Gd_2O_3 = 2Gd'_{Ce} + \ddot{V}_O + 3O_O^x$  in Kröger-Vink notation [112], which increases the turnover frequency of the catalyst even further [113]. Detailed studies of adsorption and interaction of light hydrocarbons, such as methane, with CeO<sub>2</sub> have been published [114-116]. It was established that the activation of methane occurs over CeO<sub>2</sub> surfaces through either surface coordinatively unsaturated (cus) oxygen or surface lattice oxygen anions, which both are surface active oxygen species [110, 114]. In addition to surface active oxygen species, acid-base sites are also important in the adsorption and reactions of hydrocarbons on ceria surfaces [117]. Crystallographic imperfections, such as steps, terraces, and kinks; which are considered low coordination sites on CeO<sub>2</sub> surfaces, and are where the formation of acid-base pairs are strongly favored. The presence of such defects significantly promotes the abstraction of H atoms from the hydrocarbons' C-H bonds, enabling the formation of active CH<sup>3•</sup> and H<sup>+</sup> ions on the CeO<sub>2</sub> lattice surface [115]. Formation of such ions lead to the subsequent adsorption of hydrocarbon radicals from the gas phase and unsaturated hydrocarbons bonding predominately with strong acid sites on the ceria surface which may then undergo reactions with adsorbed O<sup>2-</sup> and O<sup>-</sup> ions, promoting complete methane oxidation [110].

The deposition of catalytically active Gd doped CeO<sub>2</sub> on ZrO<sub>2</sub> based porous ceramic supports can improve the stability of CeO<sub>2</sub> nanopowders for powder loadings less than 15 wt% on the support surface [118]. Under such low catalyst concentrations, the support will prevent loosely distributed powders from sintering and coarsening at high operational temperatures [119] and, thus, the high catalytic activity of CeO<sub>2</sub> during methane combustion will be preserved. It is also well known that a combination of CeO<sub>2</sub> and ZrO<sub>2</sub> oxides can create a rather stable ionically conductive ceramic material which itself could act as a catalyst for the combustion of methane [120, 121].

#### ***2.4.3. Perovskite Oxide Catalysts***

LaCoO<sub>3</sub> based perovskites are remarkable materials with unusual electric [122], magnetic [123], mechanical [124], optical [125], and catalytic behavior [126]. LaCoO<sub>3</sub> itself is a parent compound of a broad ABO<sub>3</sub> perovskite system, where the La<sup>3+</sup> cation can be substituted with Sr, Ca, Ba or some rare earth metals that is mixed electronic and oxygen-ion conductor with exceptional thermal stability, electronic structure, ionic conductivity, electron mobility and redox behavior [127]. It was reported that Sr or Ce substituted LaCoO<sub>3</sub> showed high catalytic activity for methane oxidation reaction [128] and catalytic combustion of methane over pure LaCoO<sub>3</sub> and Sr substituted La<sub>1-x</sub>Sr<sub>x</sub>CoO<sub>3</sub> proved that cobaltites exhibited very high oxidation activities comparable with the activity of Pt/Al<sub>2</sub>O<sub>3</sub> combustion catalysts [129]. It was shown that low surface areas along with a high sinterability of LaCoO<sub>3</sub> perovskite catalysts are the major limitation for use of perovskite oxides as efficient heterogeneous catalysis in methane combustion [130], therefore the introduction of a material with a large surface area deposited on a thermally stable

support is considered as a highly beneficial way to improve the performance and characteristics of heterogeneous combustion.

#### *2.4.4. Tungsten Carbide/Palladium Catalysts*

One such catalyst of interest is tungsten carbide (WC). WC is a readily available and low cost material which was previously tested for oxygen reduction and fuel oxidation reactions as cathode and anodes in fuel cells [131, 132]. It was determined [133-135] that although the performance of WC is inferior in direct comparison with platinum and other noble metals, its low price and its insensitivity to catalyst poisons like H<sub>2</sub>S and CO [136, 137] make it a promising alternative to the noble metal catalyst for application in fuel cells. Since the electrochemical half-reactions which occur on fuel cell electrodes are paramount to combustion, catalysts which are promising for FCs are also worthy of investigation in combustion.

WC has been shown to exhibit Pt- like behavior in surface catalysis, where the chemisorption of hydrogen occurred on WC surfaces at room temperature, along with other promising chemical reactions [138]. At the same time, the stability and electrocatalytic activity of WC was significantly improved by addition of transition metals, such as Ta; the addition of Ta to WC enhanced the ORR activity of the WC catalyst while also reducing the quantity of oxygen bound on the catalyst surface [139].

While WC is a catalyst worthy of investigation, palladium (Pd) metal and its oxide (PdO) are well known as efficient promoters of combustion reactions, where it was established that Pd based catalysts enables the simultaneous oxidation of NO<sub>x</sub> and complete oxidation of CO to CO<sub>2</sub> in quartz tube catalytic reactors [140-143]. Under reaction conditions, combustion of methane over Pd based catalysts has been shown to be strongly related with formation of PdO due to the ability

of Pd to uptake oxygen from the gas phase. It was shown that both methane and hydrogen will adsorb to Pd and PdO surfaces at room temperatures [144, 145], and Pd/PdO are able to fully convert stoichiometric CH<sub>4</sub> and O<sub>2</sub> mixtures to CO<sub>2</sub> at temperatures as low as 200 °C [146]. It was also found that in addition to the ability of Pd to exchange oxygen with the gas phase, oxygen ion exchange with a ceramic substrate carrying Pd particles greatly impacts catalytic performance of Pd metal in combustion reactions [147]. It was established that an active oxygen exchange between the Pd/PdO catalyst surface and ZrO<sub>2</sub> substrate is the mechanism responsible for high turnover frequencies of H<sub>2</sub>O and CO<sub>2</sub> during methane combustion, significantly facilitating the catalytic reactions which form on the catalyst surface to substrates like Al<sub>2</sub>O<sub>3</sub> which exhibit significantly lower O<sup>2-</sup> ion conductivities [148-150]. Therefore use of fast oxygen conducting ceramics, such as ZrO<sub>2</sub> stabilized with Y<sup>3+</sup> or Sc<sup>3+</sup> tri – or Ca<sup>2+</sup> or Mg<sup>2+</sup> di-valent atoms, would enhance Pd/PdO catalyst performance even further.

### 3. COMBUSTOR APPARATUS, CATALYST APPLICATIONS and EXPERIMENTAL METHODS

#### 3.1. Introduction

The heterogeneous combustor used within this work Figure 3-1 contains over 100 individual components and is the product of my own design with the assistance of four senior design groups and counting whom worked closely with me on the development of specific components.

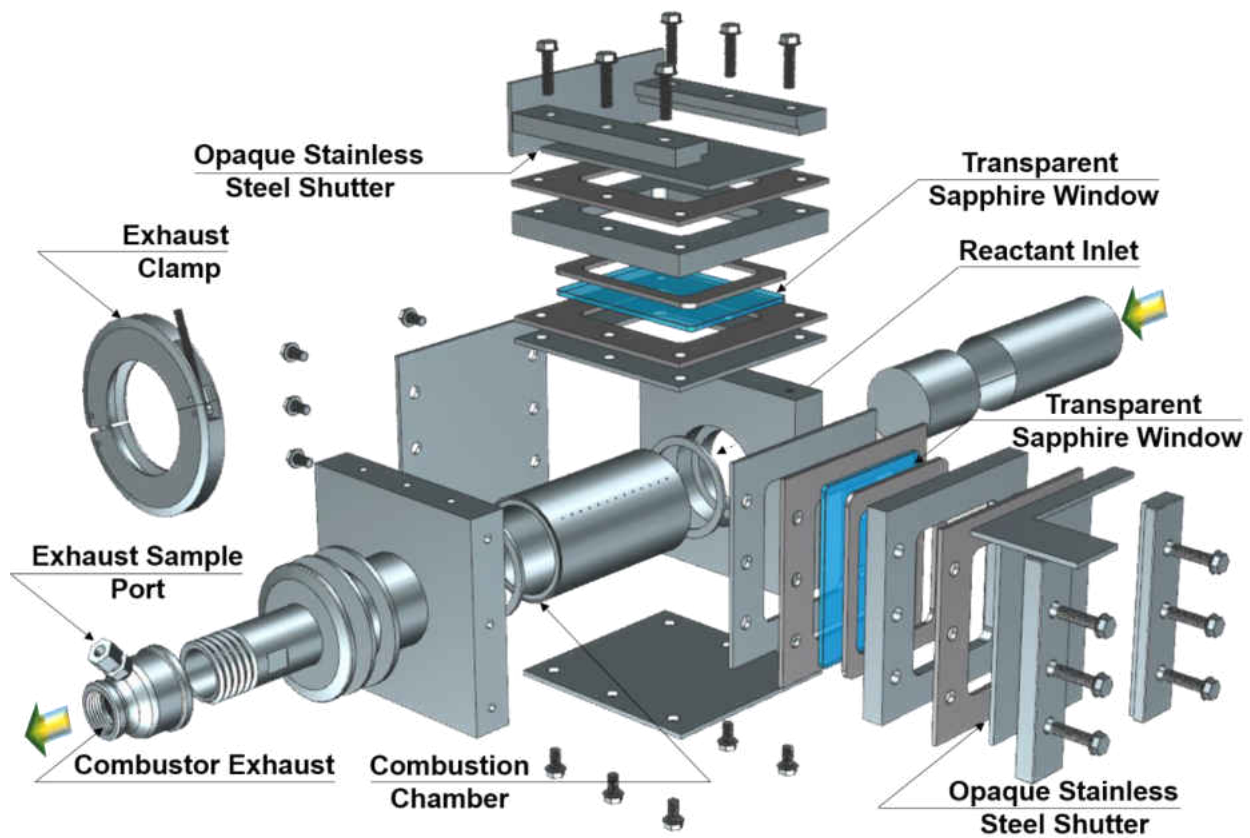


Figure 3-1: Exploded view of combustor

Construction of the device hardware was executed in stages. Following previous experimental and numerical investigations [54], dimensions and flow rates of this combustor dubbed *Thor's Hammer* were defined. The second developmental stage consisted of: the inclusion of observation

windows in the external chamber housing, a liquid fuel delivery apparatus, and a large heat exchanger for the subcritical heating of water.

A schematic presentation Figure 3-2 and a photograph of the developed chamber in operation is shown in Figure 3-3. Some of the factors that were considered in the design of the combustion chamber were (i) method of ignition, (ii) flow rate limits, and (iii) dimensions of the porous media, and simplicity of design. The locations of 13 thermocouples along the length of the combustion chamber and also two thermocouples placed at the inlet and at the exhaust are also shown, which are used to collect temperature profiles during combustion as a function of time.

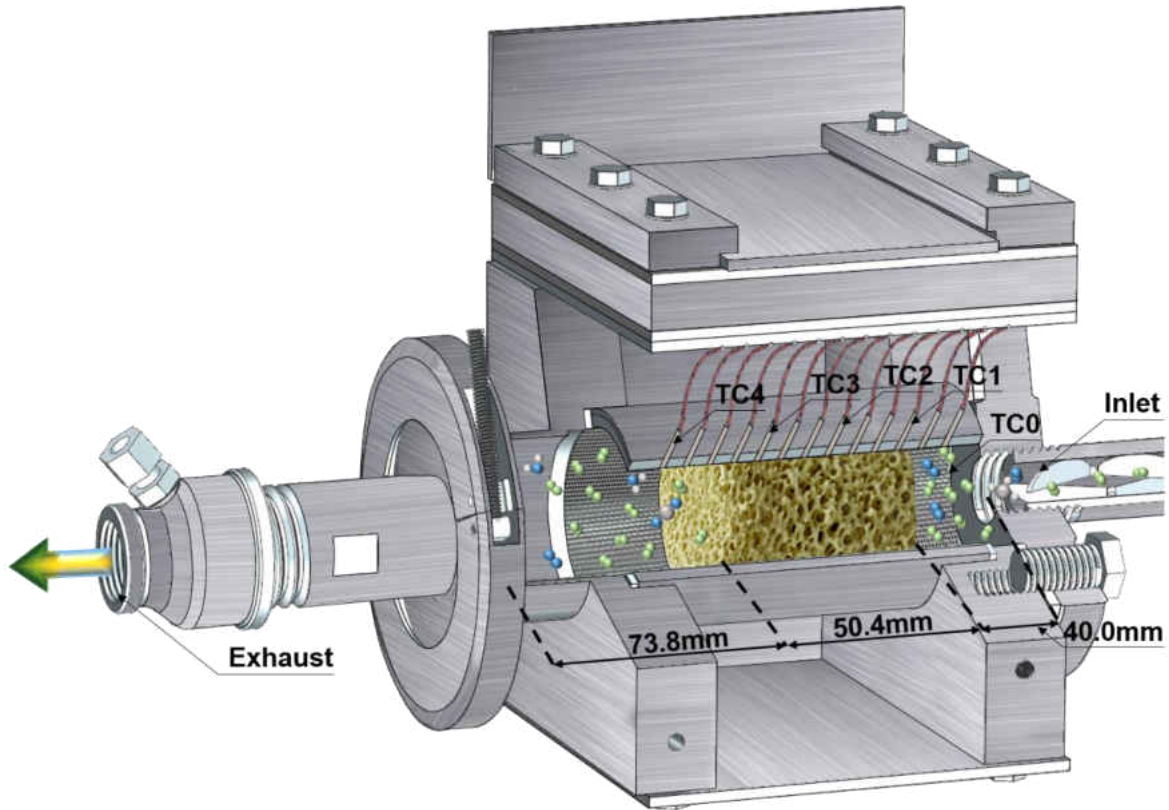


Figure 3-2: Schematic of the combustion chamber

The incorporated sapphire viewing windows and stainless steel shutters, can be used to visualize the temperature distribution on the outer surface of the stainless steel combustion chamber when

the shutters are open enabling determination of the approximate location of the flame within the combustion chamber. The photograph taken of the outer surface of the stainless steel combustion chamber radiating heat, through the sapphire window with the front shutter open, reveals the approximate location of the combustion zone as shown in Figure 3-3. However, if the stainless steel inner combustion chamber were to be replaced by a sapphire tube, direct flame visualizations or the incorporation of advanced spectroscopy techniques could be made [19].

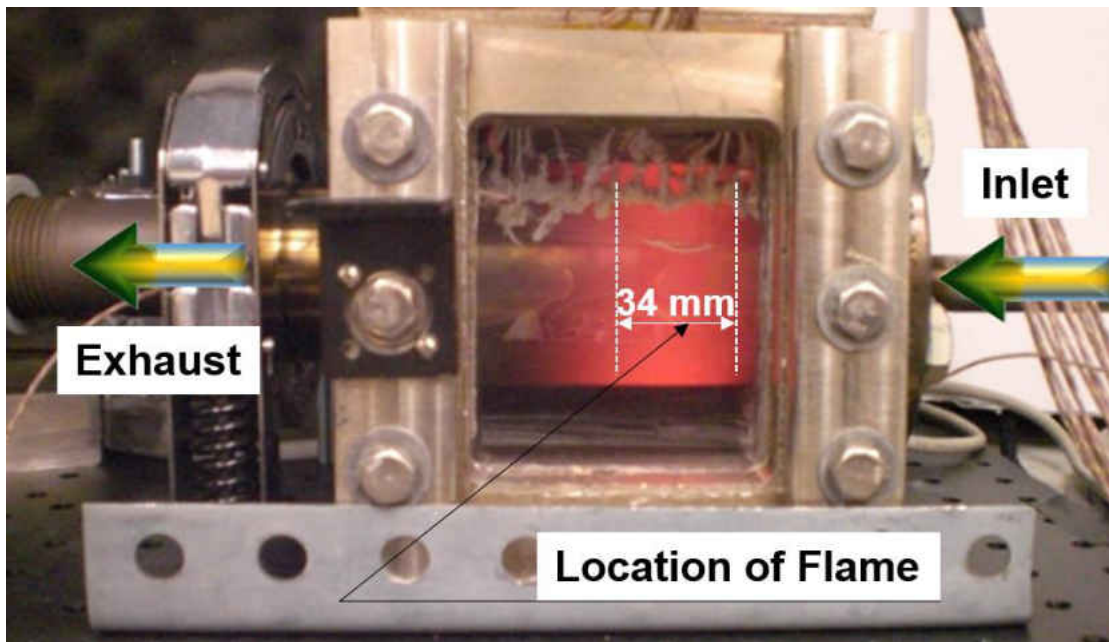


Figure 3-3: Photograph of the experimental combustor in operation; the approximate flame

Figure 3-4 presents side view photographs of the combustion chamber, where the Figure 3-4A presents the chamber with both top and side shutters closed, and Figure 3-4B presents the chamber with the shutters removed revealing the sapphire optical windows which can be used for observation of temperature distribution inside. The 13 axial combustion chamber thermocouple wire leads are also visible in Figure 3-4 A and B and an optical micrograph of a thermocouple built for temperature measurements along the combustion chamber is shown in Figure 3-4C. Axially placed thermocouples are positioned 6.87 mm apart within small bores along the outer radius of

the combustion chamber axis. Each thermocouple is prepared with an alumina double bore tube (AdValue Technology LLC: Tuscon, USA) through which K-Type 30 GA wire (Omega Engineering: Stamford, USA) is drawn. Thermocouple beads are manufactured via spot welding and have a diameter of approximately 700  $\mu\text{m}$ . Each thermocouple within the bore is then exposed indirectly to the combustion environment, which occurs across a SAE 316 stainless steel wire mesh, with each thread being approximately 115  $\mu\text{m}$  in diameter. A schematic of the thermocouple is located relative to the porous ceramic media is shown in Figure 3-4D. Signals from the thermocouples were recorded via a NI 9213 thermocouple DAQ (National Instruments: Austin, USA) within LabView (National Instruments: Austin, USA) at a rate of 8 Hz.

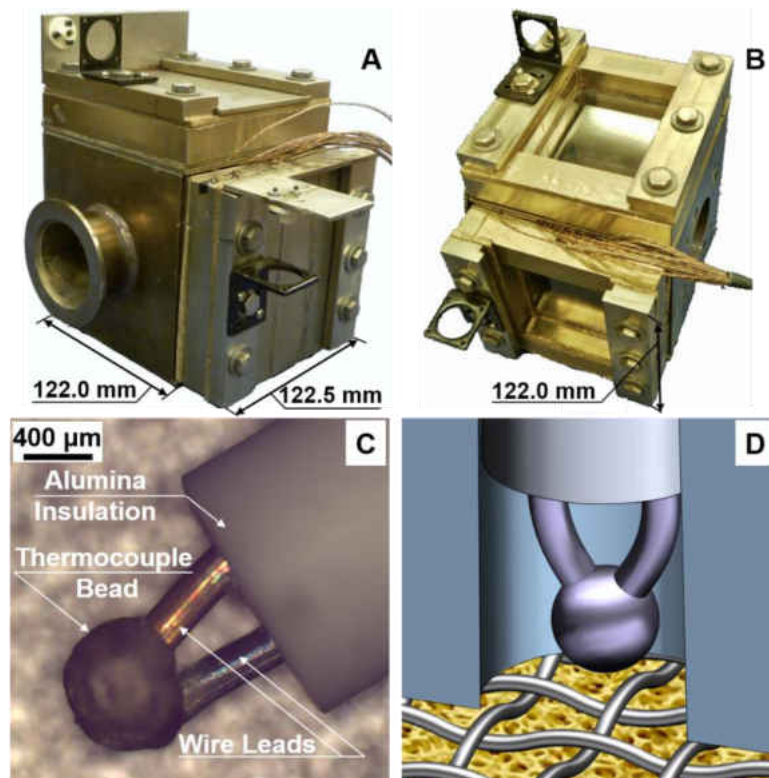


Figure 3-4: (A) Isometric view of combustion chamber exhaust side with shutters closed. (B) Isometric view of combustion chamber inlet side with shutters open exposing alumina windows. (C) Optical micrograph of the thermocouple designed for use along the combustion chamber axis. (D) Axial thermocouple schematic showing the separation of thermocouple probe from porous media via a wire mesh.



Three types of porous media (ASK Chemicals: Hilden, DE) were considered to be used in the combustion chamber. One type of media chosen was alumina, as it is known to be catalytically inert in combustion [28], and two others MgO stabilized  $ZrO_2$  and SiC were chosen as they are potential candidates to promote heterogeneous combustion [107, 151]. The manufacturer reports the porosity of all three types of porous media as 10 pores per inch [152]. A photograph of the  $Al_2O_3$ , MgZrO<sub>2</sub> and SiC three porous media are shown in Figure 3-5. Before being inserted in the combustion chamber, the porous media was wrapped in a steel wire mesh in order to minimize degradation and to prevent the hard ceramic media from scratching the inner surface of the stainless steel combustion chamber. The porous media placed within combustion chamber provides housing to the flame and is located at a 40mm span away from the reactant inlet, where the flame position within the chamber is controlled via the reactant flow rate through the combustion chamber and the flame's interactions with the solid media. Therefore, a design of the combustor developed in this work is unique, as by placing the porous ceramic media at a certain distance away from the reactant inlet allowed the flame to be forced and kept inside of the porous media by simply the reactant flow rates with no extra flow conditioning device being employed. From an analysis of designs of such heterogeneous combustors published in the literature [80, 153-155] such flow conditioning devices, placed along with porous ceramic media, were used to for the flame inside. For example, a metal plate with finely distributed small channels was used in [80] to prevent the flame from advancing. A “low” porosity “ceramic” section was used as a flashback arrestor in [154, 155].

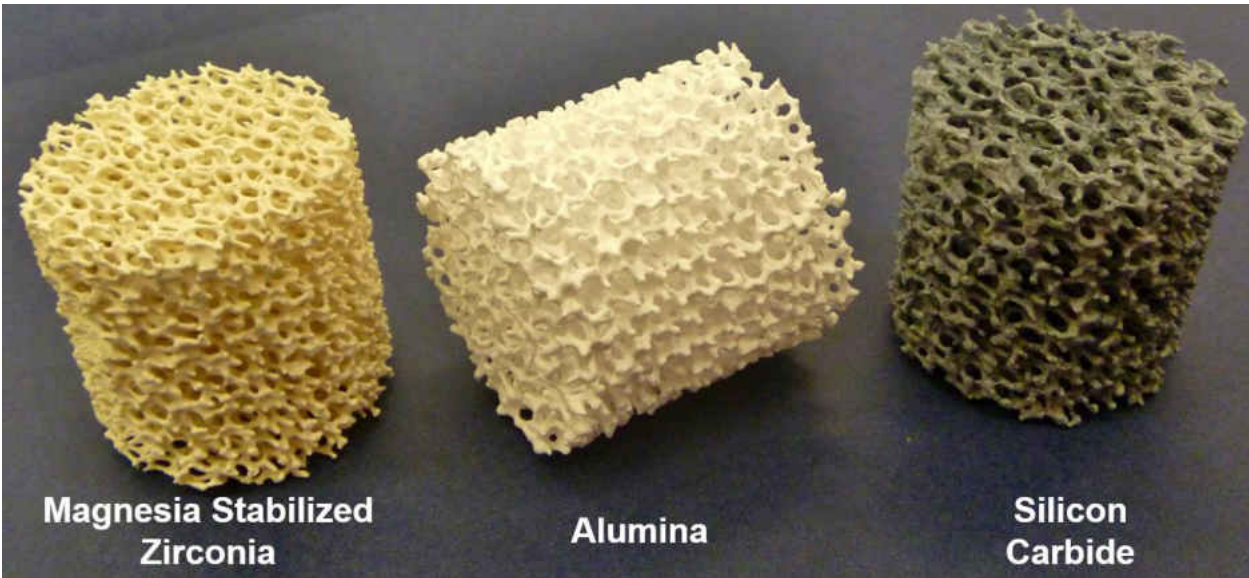


Figure 3-5: A photograph of MgO stabilized ZrO<sub>2</sub>, Al<sub>2</sub>O<sub>3</sub>, and SiC porous ceramic media used for combustion experiments inside of the combustion chamber to contain a flame. The porous ceramic cylinders contain 10 pores per inch and have 50mm in diameter and 50.4mm in length.

### 3.2.Methods of Reactant Delivery and Control

In order to operate porous combustor, the mixture of fuel and air gases must be constantly delivered to the inner combustion chamber. To do this, an innovative reactant delivery nozzle was proposed and developed in this work. In order to deliver reactants in a highly controlled manner to the fuel delivery nozzle a reactant control and metering system was developed, and the block diagram of the reactant delivery path is shown in Figure 3-6. In this reactant delivery system, laboratory air is drawn into compressors and stored in two large reservoirs. Pressure regulators are used to control the discharge of air from the reservoirs before it passes through a two stage dryer. A secondary storage tank, with bypass, is then utilized to reduce the amplitude of pressure fluctuations in the dried air. A split in the air line then directs air toward two additional pressure regulators resulting in: a low flow line in which “fine air” is controlled using an FMA-3200 series flow controller (Omega Engineering: Stamford, USA), and a high flow line in which “coarse air” is controlled using an Aalborg GFC47A-VDL6-C0 flow controller (Aalborg: New York, USA).

Following the Aalborg flow controller, the coarse air passes through a tertiary storage and bypass line to further minimize pressure fluctuations before delivering air to the delivery nozzle. Methane is drawn from a parallel set of methane cylinders before undergoing a double pressure regulated stepdown and subsequent flow rate control is achieved using an Aalborg GFC17S-VAL6-C0 flow controller (Aalborg: New York, USA). Methane and fine air are then mixed in a manifold before entering the delivery nozzle.

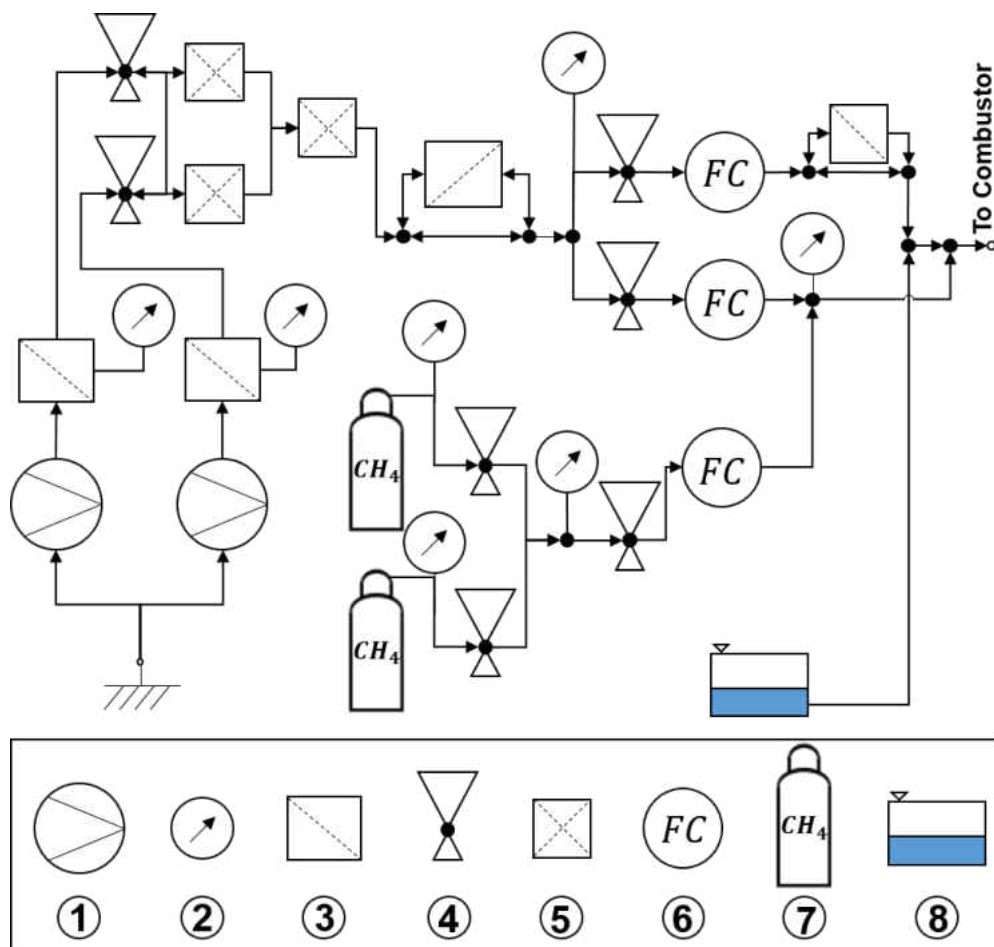


Figure 3-6: Block diagram of reactant delivery path. (1) compressor, (2) pressure gauge, (3) reservoir, (4) pressure regulating valve, (5) dryer, (6) flow controller, (7) methane cylinder, and (8) liquid fuel reservoir.

The delivery nozzle is comprised of several components: a siphon nozzle, four supplemental inlet ports, inlet cap, reducer, coupler, KoFlo Tube Mixer (KoFlo Corporation: Cary USA), and

Inlet Flange; which together function to bring a single phase mixture of homogeneous composition into the combustion chamber, as seen in the assembly diagram of the delivery nozzle and its corresponding cross section view Figure 3-7. While the delivery nozzle was designed to handle both liquid and gaseous fuels, in the current work only gaseous mixtures were used.

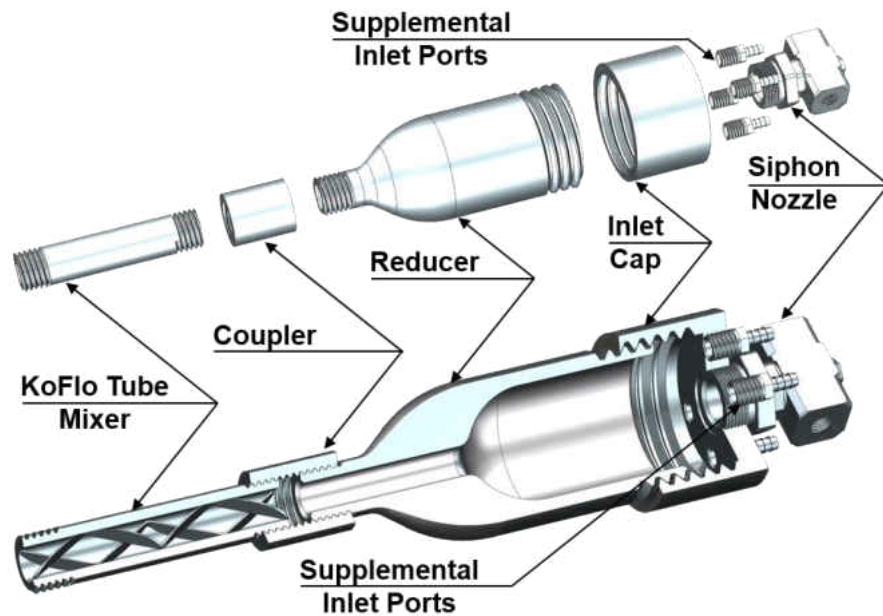


Figure 3-7: Assembly model and cross sectional view of fuel delivery nozzle.

For delivery of the liquid fuel, a special BETE XFA air atomizing siphon nozzle (BETE: Greenfield, USA) was utilized, which provides two inlets, one inlet for liquid fuel and another inlet for air Figure 3-8A. During operation, air leaving the siphon nozzle passes over a small concentric opening, which leads to the liquid fuel inlet of the siphon nozzle. Air at high flow velocity induces shear stresses around the liquid fuel opening thus creating a 10 kPa maximum vacuum at the liquid fuel inlet allowing the liquid fuel to be delivered to the cavity bounded by the inlet cap and reducer Figure 3-6. As the opening of the siphon nozzle, which liquid fuel is delivered, is very small and equals to a  $900 \pm 25 \mu\text{m}$ , the droplets of fuel which are coming to the reducer are fine enough that they create an aerosol, consisting of liquid fuel and air, which

emanates from the center of the inlet cap. In order to prevent the liquid droplets within the aerosol from condensing on the walls of the reducer, mixtures of gaseous  $\text{CH}_4$  and air, distributed via the four supplemental inlet ports of the inlet cap, were used to create a buffer layer preventing the aerosol spray from impinging on the solid surfaces of the reducer before they enter the KoFlo tube mixer Figure 3-8B. Once within the tube mixer, specifically designed baffles provide a tortuous path for reactants to travel, ensuring the complete vaporization of any remaining liquid fuel droplets and even dispersion of reactants entering the combustion chamber. Two photographs of the inlet cap from different perspectives are presented in Figure 3-9 A and B with an additional photograph of the assembled delivery nozzle is presented in Figure 3-9 C.

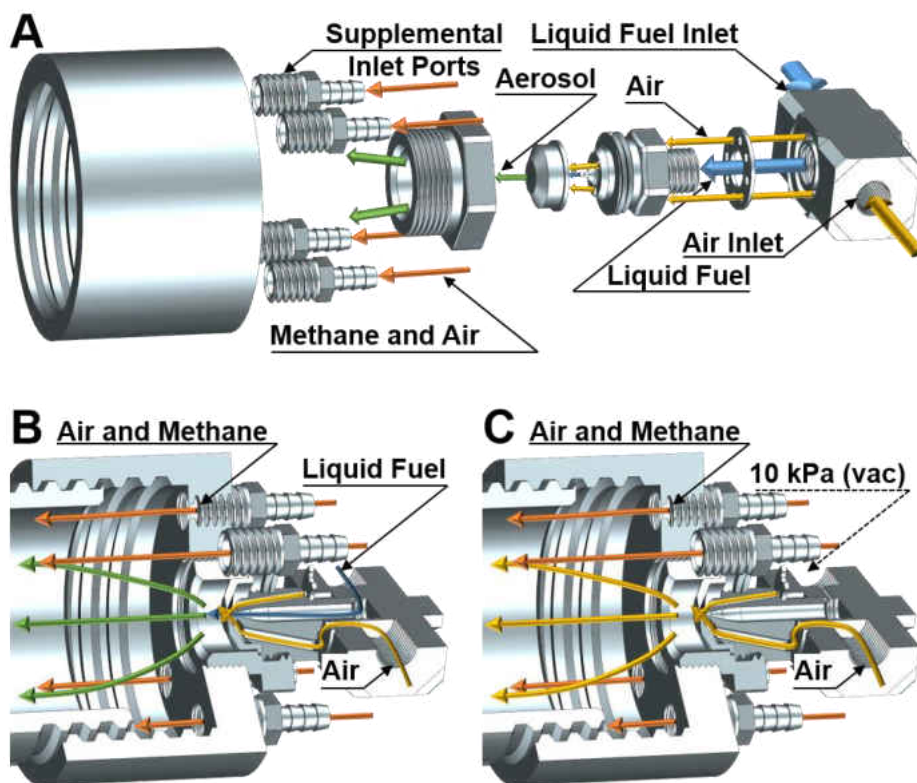


Figure 3-8: (A) Exploded reactant flow diagram of siphon nozzle. (B) Reactant flow path when both liquid fuel and methane are simultaneously used. (C) Reactant flow path when only methane fuel is used.

In the case when only gaseous fuel/air mixtures were utilized, as it was in the experiments presented in the current work, the following pathway was used to deliver gases to power the combustion chamber. Premixed air and methane entered the reducer via four supplemental inlet ports with a concentration of 10 SLPM of air, and 2.25~4 SLPM of methane. Simultaneously 37.5 SLPM of air was additionally delivered via the siphon nozzle. Such scheme of delivery of gasses ensured that sufficient flow rates of gases were maintained to operate the combustion chamber. After gases entered and mixed in the reducer, they pass through the KoFlo tube mixer where further homogenization of the mixture occurs, and then they go further directly into the combustion chamber. A schematic of the gaseous reactant pathway is presented in Figure 3-8B.

Reactants entering the combustion chamber from the delivery nozzle were expected to exhibit swirl about the axis of the combustion chamber due to the geometry of the KoFlo Tube Mixer as well as recirculation due to the sudden expansion at the combustion chamber inlet [156]. These parameters, swirl and recirculation, further homogenize the gaseous temperature and composition over the volumes where they occur. Swirl, in addition to reducing the angular variation in gas composition and temperature induces centrifugal forces into the fluid, accelerating the rate at which the velocity profile becomes uniform in the axial direction. Fluids exiting a sudden expansion will exhibit a central core in which the dynamic pressure is uniform and positive, meaning the fluid within this region flows along the axis with a uniform velocity profile. Within some axial span from the expansion, which varies with flow Reynold's number, a radial dynamic pressure gradient exists. At some radial position within this region the dynamic pressure will become negative, meaning the fluid will locally flow against the axial direction. Within this region



recirculation is said to occur [157]. Regions in which recirculation occurs will exhibit nearly constant temperature and composition due to the mixing of gases.

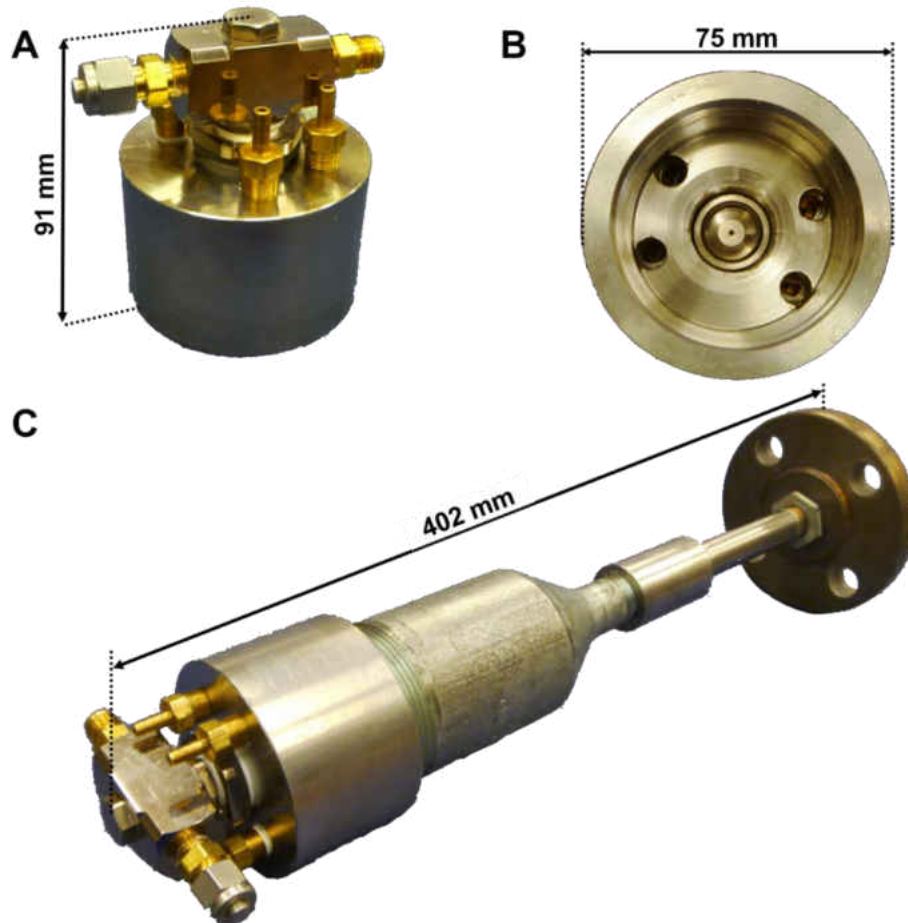


Figure 3-9: Photos of (A) Inlet Cap assembled with siphon nozzle and supplemental inlet ports attached, liquid fuel inlet is capped off; (B) underside view of fuel inlet cap. (C) Assembled fuel delivery nozzle.

To accurately characterize the swirl and recirculation experienced at the sudden expansion where the reactant delivery nozzle discharges into the combustion chamber, a CFD analysis was performed to verify that recirculation would not overlap the space within the combustion chamber where the combustion media would be placed. A flow domain was generated and analyzed within Siemens NX 8.5 (Siemens: Munich, DE) which replicated the geometry of the coupler, tube mixer, and empty combustion chamber consisting of 1.8 million tetragonal quadratic elements and a

nominal wall surface roughness of 115  $\mu\text{m}$ . The inlet boundary condition imposed at the coupler assumed dry air at 26.85  $^{\circ}\text{C}$  with an axial velocity profile and a mass flow rate of 60 SLPM, which is considered as the maximum flow rate for the existing instrumentation of the combustor and when the recirculation region would occupy the largest volume within the combustion chamber. At the exit boundary condition, an atmospheric criterion was assumed. From this simulation, Figure 3-10, the recirculation region was found to extend 25 mm into the combustion chamber enabling a 15 mm span for the flow profile to normalize before entering the porous media which is placed 40mm from the combustion chamber inlet.

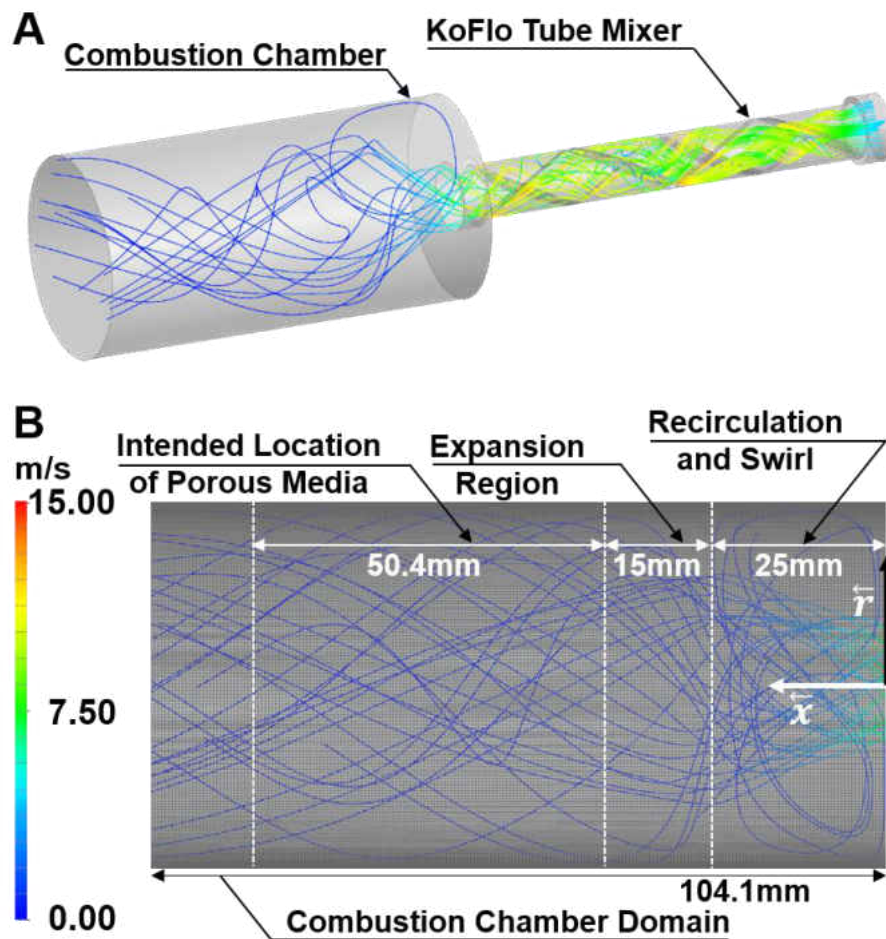


Figure 3-10: (A) Isometric view of flow streamlines and flow domain. (B) Side profile view of flow streamlines combustion chamber showing the length of recirculation.



### 3.3. Ex-Situ Instrumentation

Aside from the combustion chamber and reactant dispersion components of this combustor, several other instrumentation devices were also included to collect important supplementary data on system operation Figure 3-11 A and B. Thus, the experimental setup includes (i) a microphone, (ii) a CCD camera; and (iii) an exhaust sample port which is connected to a gas chromatograph to analyze the composition of exhaust gases.

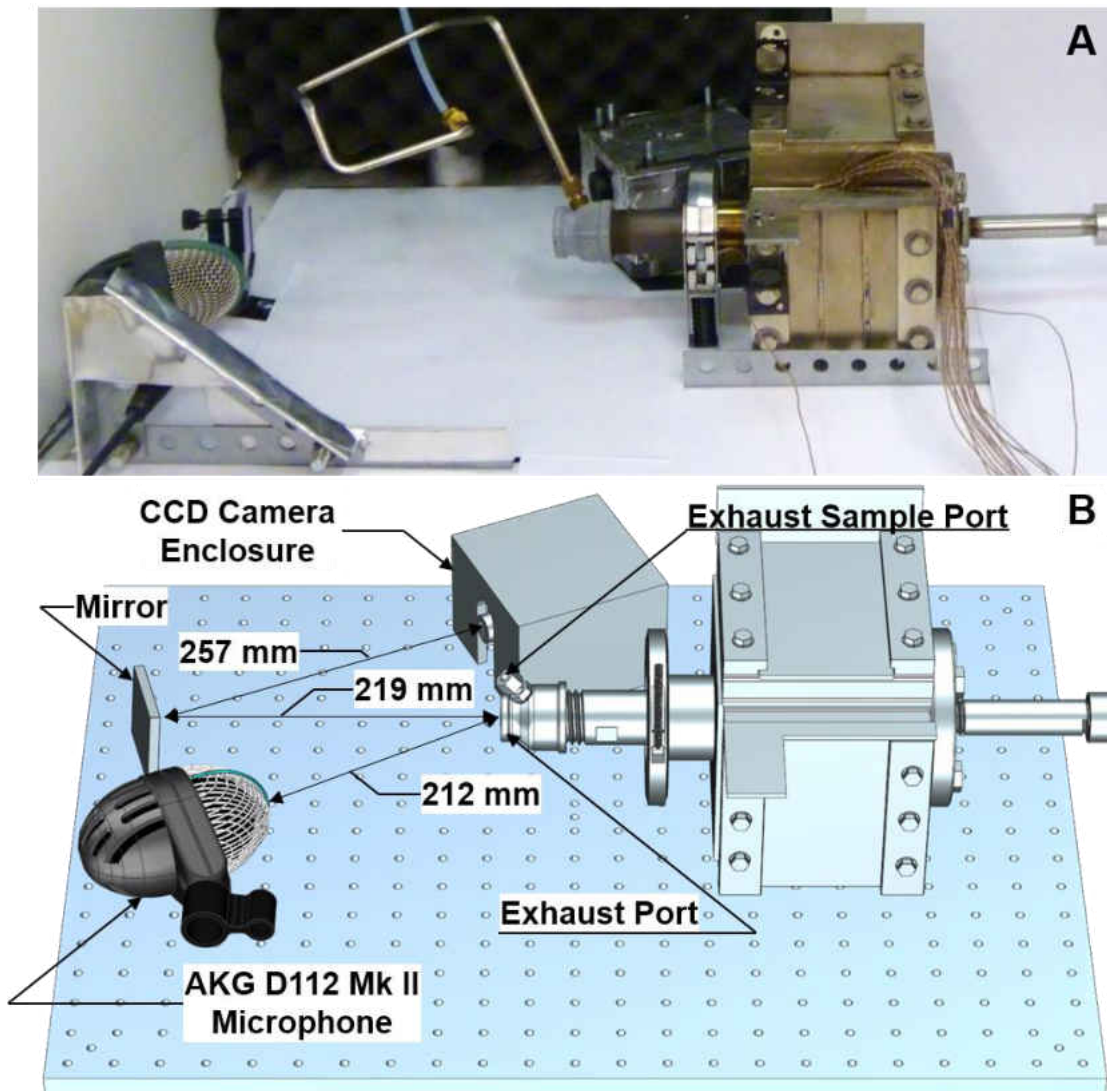


Figure 3-11: (A) A photograph of the heterogeneous combustor aligned with instrumentation devices within a fume hood. (B) A schematic for the location of the microphone, mirror, and CCD camera relative to the combustor exhaust port in the experimental set up.

### ***3.3.1. Acoustic Measurements Setup***

Acoustic measurements were recorded using an AKG D112 MkII (AKG Acoustics: Vienna, AT) microphone mounted at a fixed location on an optical breadboard using a modally tuned mounting bracket. The optimal position of the microphone relative to the exhaust port of the combustion chamber was found by taking an acoustic signal at different locations and finding the location with the best optimal fidelity. Time signals were recorded from the microphone at 192 kHz with a 24-bit sampling depth utilizing a Fenix HT OMEGA sound card (HT OMEGA: Ontario USA) and LabView software (National Instruments: Austin, USA). As the fume hood where the combustor and microphone were placed in has flowing air; it was expected some background noise would be present due to both the flowing air and the induced excitations of the fume hood panels. To reduce the interference of the background noise present in the enclosure which housed the combustion chamber, metallic foil tape was placed along various free edges around the fume hood enclosure to provide additional structural damping. Additionally, echoes within the fume hood were controlled through the placement of noise absorbing foam panels over the exposed metal surfaces of the fume hood. A schematic of experimental set of the combustor with included microphone's location is presented in Figure 3-11 B.

### ***3.3.2. Optical Measurements Setup***

Optical observations through the combustion chamber exhaust were made using a Sanbent D200 CCD camera (Shenzhen Meikeda Electronic Co.: Shenzhen, CN) with a non-magnifying lens aligned with an aluminum optical mirror (ThorLabs, Inc: Newton USA) and the combustion chamber exhaust Figure 3-11 B. To record optical emissions using the CCD, the combustor exhaust was aligned with the mirror. Using adjustments on the mirror and CCD camera, additional

alignments were made to ensure a quality alignment of the combustion chamber exhaust relative to the mirror surface. Images were recorded using the LabView Vision Acquisition Suite at variable frame rates. During ignition a high frequency recording mode at a rate of 15 Hz was used to capture fine details, though during operation of combustor images were recorded at a fixed interval with 60 seconds between each frame; regardless of the rate of data acquisition the camera's exposure time was maintained at 0.066 ms.

### ***3.3.3. Gas Chromatography***

Exhaust samples from this combustor were taken through the special access port which enabled gasses to be drawn from the combustor exhaust. Exhaust gas samples were drawn through a 6 port Valco Valve, with an attached sample tube, using a vacuum pump. Simultaneously, a helium carrier gas supplied at a rate of 25 ml/min was delivered to one column of the Gow-Mac 200 Gas Chromatograph (GC) (GOW-MAC Instrument Co.: Bethlehem, USA) , with a 30' Haysep D/B 100 column while an additional helium reference flow was supplied at a rate of 25 ml/min. When exhaust gas analysis was to be conducted, the position of the Valco-Valve (Valco Instruments: Houston USA) was switched and the carrier gas was used to push the exhaust sample from the sample tube into the GC. Samples were analyzed utilizing a tungsten-rhenium thermal conductivity detector (TCD), which produced a voltage output signal; Signals from the TCD were recorded using a NI-6210 DAQ (National Instruments: Austin, USA) and LabView software.

Within Figure 3-12 chromatograms of pertaining to samples of Air and exhaust are compared using the above mentioned GC setup, the insert shows that the only peaks within either chromatogram occur before 10 min. When air was sent through the GC, a single peak was observed at 3.90 min with a width of 1.42 min. Whereas when exhaust gases were sampled while the

combustion chamber was operating at  $\dot{V}=41.65\pm 0.61$  SLPM and equivalence ratio  $\phi=0.90\pm 0.02$  with immersed SiC media. The chromatogram pertaining to the exhaust sample exhibits two peaks. The first peak in the exhaust sample occurs at 4.58 min, and has a width of 2.54min. Whereas the second peak occurs at 7.23 min and has a width of 2.04 min. From the analysis of the chromatograms, the GC/TDC/sampling system incorporated to the combustor does function properly; however, the column does not exhibit the proper selectivity to accurately separate out the gaseous species of interest.

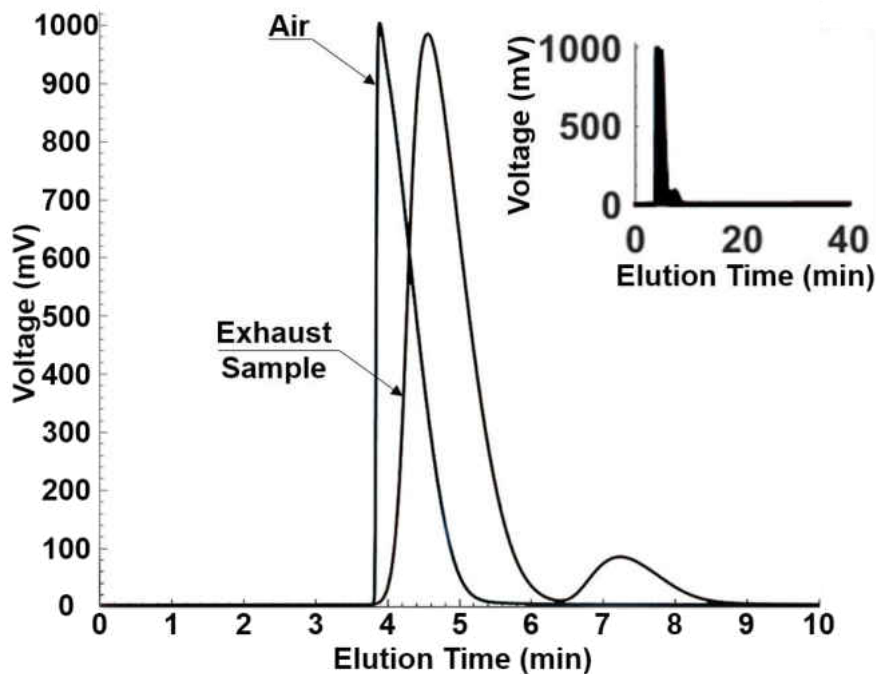


Figure 3-12: Chromatograms of exhaust samples and air using the GC/TDC/sampling system incorporated to the heterogeneous combustion chamber.

### 3.4.Characterization of Selected Substrates

Within this work, 3 substrates: silicon carbide SiC, magnesia stabilized zirconia (MgO-ZrO<sub>2</sub>, MSZ), and  $\alpha$ -alumina ( $\alpha$ -Al<sub>2</sub>O<sub>3</sub>) were characterized as promoters of heterogeneous combustion. All of the substrates utilized a fixed porosity of 10 ppin, a length of 50.4mm and a diameter of 50.0 mm.

### 3.4.1. Silicon Carbide

Within Figure 3-13, an X-ray diffraction pattern, along with SEM micrographs of the SiC media surface are presented. From analysis of the diffraction pattern, there are many prominent peaks which have been characterized as one of two materials: either SiC or quartz ( $\text{SiO}_2$ ) ( $Fd\bar{3}m_1$ ) [158].the material contains several polytypes of Silicon carbide [159-162]. It is difficult to determine the exact phase composition of SiC as the majority of the peaks among the various polytypes overlap in a non-linear manner. From micrographs within the figure of the SiC surface, it can be seen that the surface of the SiC is highly contoured showing many surface pores and surface kinks.

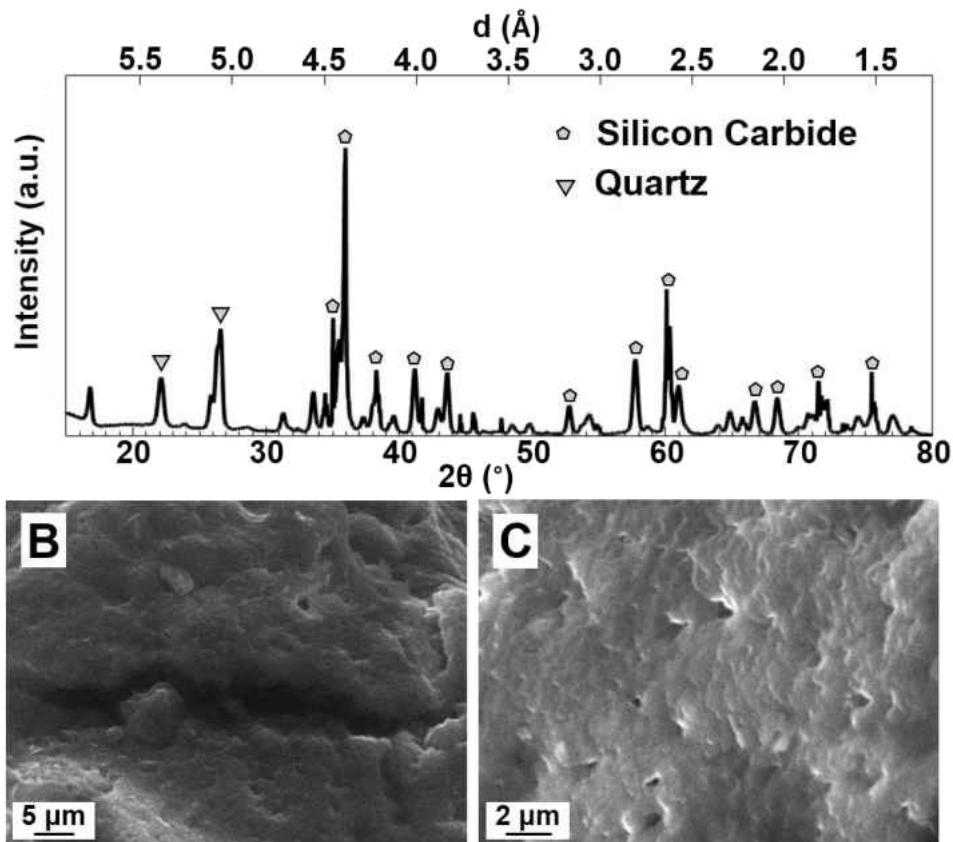


Figure 3-13: (A) XRD pattern of SiC. (B and C) Scanning electron micrographs of SiC.

### 3.4.2. Magnesia Stabilized Zirconia

The X-ray diffraction pattern of powdered MSZ substrate is shown in Figure 3-14 A. Only two ZrO<sub>2</sub> phases, tetragonal (*P4<sub>2</sub>/nmc*) [163] and monoclinic (*P2<sub>1</sub>/c*) [164], can be found in this diffraction pattern. While no other distinct peaks are visible, the presence of some amount of cubic phase within a mixture of tetragonal and monoclinic phases may not be precluded as tetragonal and cubic phases exhibit significant overlap of their peaks [163, 165].. It is well known that by measuring the intensity of the (111) peak of tetragonal phase and (111) and (11 $\bar{1}$ ) peaks of monoclinic phases of ZrO<sub>2</sub> located at  $2\theta_{CuK\alpha}=30^\circ, 31.4^\circ$  and  $28.2^\circ$ , the amount of tetragonal phase in the mixture can be estimated [166]. As one can see from Figure 3-14A, the intensity of the (111) tetragonal peak is very small while intensities of (111) and (11 $\bar{1}$ ) peaks of monoclinic phase is very high, thus the amount of tetragonal phase in the batch is very small. The calculations using  $X_m = \frac{I(111)_m + I(11\bar{1})_m}{I(111)_m + I(11\bar{1})_m + I(111)_t}$ , provides an estimate of 93.6 wt% monoclinic for the uncoated MSZ media. This might be a result of the grinding of the sintered porous material in the mortar to produce a fine powder to perform X-ray analysis, where the stress induced tetragonal to monoclinic phase transition was caused by the grinding, thus most of tetragonal phase present in MSZ porous media transformed into monoclinic phase during grinding. Therefore, the diffraction pattern presented in Figure 3-14A does not represent the phase composition of MSZ porous media as received, but it does show that only peaks belonging to two ZrO<sub>2</sub> phases were present. The SEM micrographs of the MSZ surface are shown in Figure 3-14 B and C. As one can see from Figure 3-14 B and C, the twin precipitation or lamellar defects are clearly visible, which are very characteristic features of MgO partially stabilized ZrO<sub>2</sub>, as it is only 3 wt% of MgO used for

stabilizing the tetragonal phase, and therefore both tetragonal and monoclinic phases are present and co-exist.

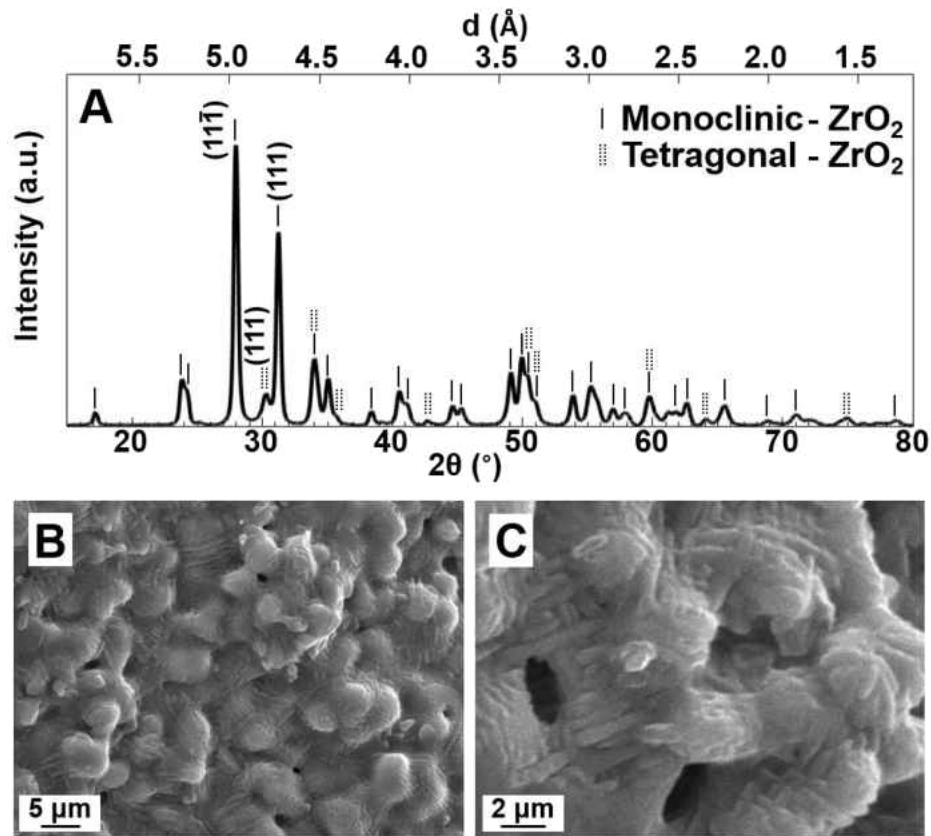


Figure 3-14: (A) X-ray diffraction pattern; (B) and (C) SEM micrographs of the surface of the 3 wt% MgO stabilized ZrO<sub>2</sub> ceramic.

### 3.4.3. Alumina Oxide

From Figure 3-15 an X-ray diffraction pattern, along with SEM micrographs of the  $\alpha$ -Al<sub>2</sub>O<sub>3</sub> media surface are presented. From the XRD pattern, it can easily be seen that the composition of the alumina is phase pure with space group ( $R\bar{3}C$ ) [167]. From the SEM micrographs within the figure, it can be seen that the alumina media is a polycrystalline substance with individual particles on the order of 2  $\mu$ m.

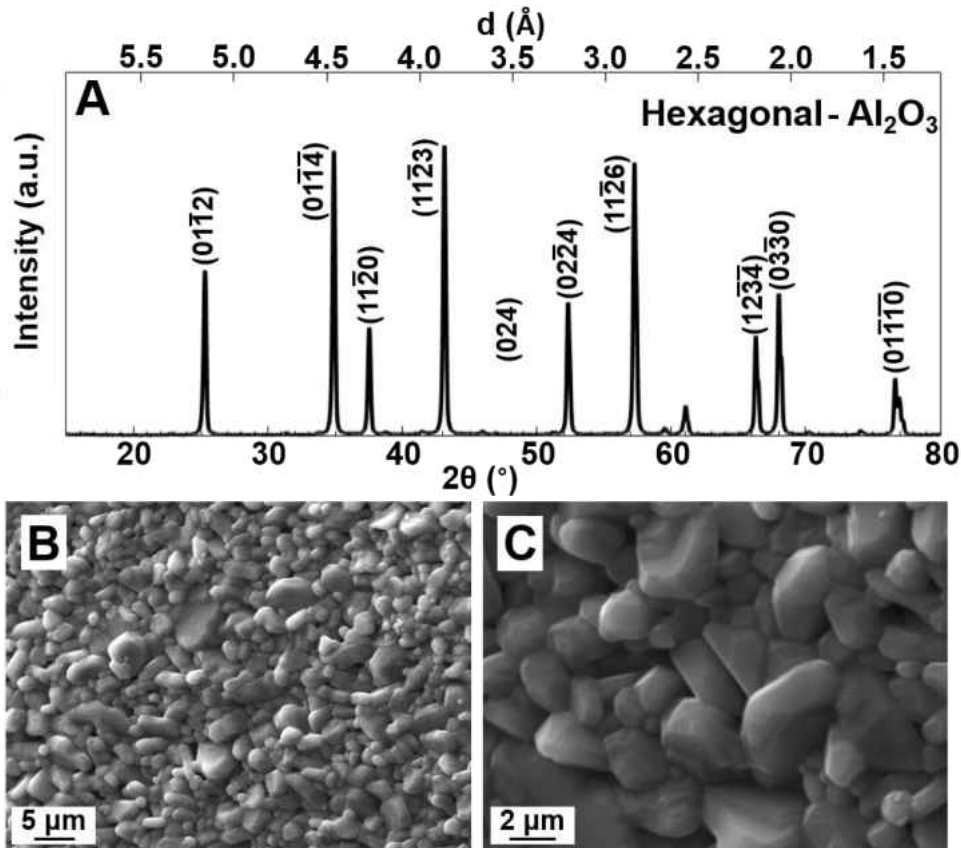


Figure 3-15: (A) X-ray diffraction pattern; (B) and (C) SEM micrographs of the surface of the Al<sub>2</sub>O<sub>3</sub> ceramic.

### 3.5. Catalyst/Coating Characterization

Following characterization of the catalyst and substrate by XRD, EDS, and SEM techniques, combustor performance is evaluated with inserted MSZ media with and without GDC coating.

#### 3.5.1. $Ce_{0.8}Gd_{0.2}O_{1.9}$

An X-ray diffraction pattern of GDC is shown in Figure 3-16A, where only peaks of the cubic CeO<sub>2</sub> fluorite phase can be seen ( $Fm\bar{3}m$ ) [168], indicating that the catalyst powder used in the current experiment is phase pure. SEM micrographs of the GDC powder at two different magnifications are shown in Figure 3-16 B and C, where one can see that the powder is very fine with particle size on the order of 0.1-0.2 μm. EDS analysis of the catalyst confirmed the presence



of only Gd and Ce metals with the peak of C showing due to the composition of the carbon tape used to mount the powder for analysis.

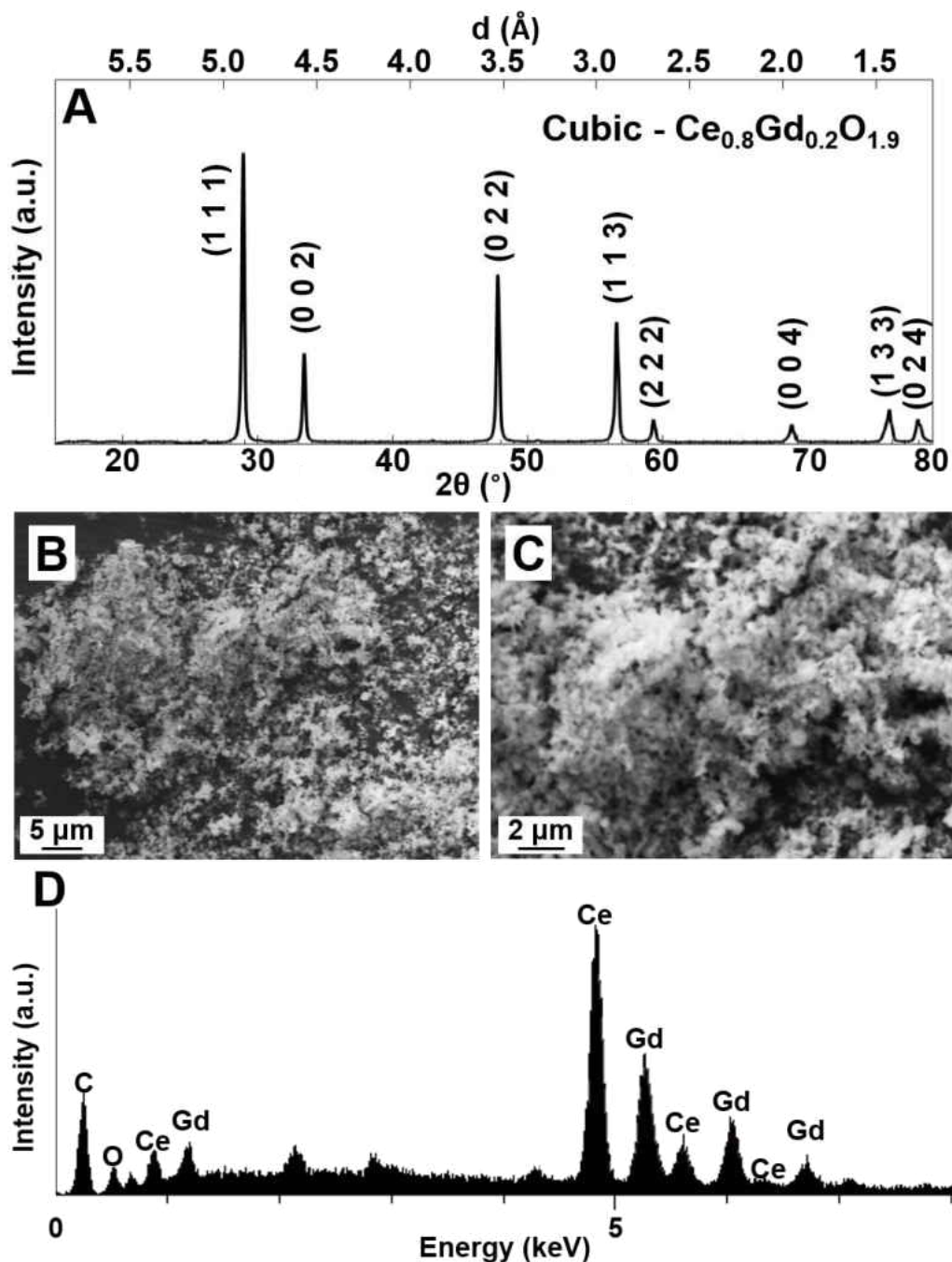


Figure 3-16: (A) X-ray diffraction pattern; (B) and (C), SEM micrographs and (D) EDS of  $\text{Ce}_{0.8}\text{Gd}_{0.2}\text{O}_{1.9}$  catalyst powders used for coating the 3 wt% MgO stabilized  $\text{ZrO}_2$  porous media.

An X-ray diffraction pattern of MSZ media coated with GDC powder is shown in Figure 3-17 A. Since only a small amount of GDC powder was present on the surface of MSZ porous media after dip coating and calcination, X-ray diffraction does not show any GDC as its concentration is below the detection limit of the instrument. Similarly, to the diffraction pattern of pure MSZ, the (111) peak of tetragonal  $\text{ZrO}_2$  had a very low intensity, which was caused by a stress induced tetragonal to monoclinic phase transition during grinding of  $\text{ZrO}_2$  porous media. It was estimated that 94.3 wt% of monoclinic phase was found after grinding. Micrographs of MSZ porous media surfaces coated with GDC powder is shown in Figure 3-17 B and C. As one can see, the loading of GDC powder onto surfaces of the MSZ porous media was quite low, as the majority of the  $\text{ZrO}_2$  surface remains uncoated. It is known that at the loading of about 15 wt%, a monolayer of the powder should form on the coated surface [118], so it is estimated from SEM micrographs that less than 5 wt% of GDC powder was applied in the dip coating process. By comparing the size of GDC particles in the as-received powder (Figure 3-16 B and C) and those deposited on the MSZ surface (Figure 3-17 B and C) after calcination at 1100 °C for 4 hours twice, one can notice that no significant growth of the GDC particles occurred as the GDC particles deposited on the surface are still less than 1  $\mu\text{m}$  in size. The selected area EDS analysis (Figure 3-17 D) from the surface of the GDC coated MSZ media confirmed the presence of  $\text{ZrO}_2$  as well as GDC materials. However, as the EDS analysis does not show the presence of Mg (Figure 3-17 D) it can be concluded that the composition of the MSZ media is not homogeneous.

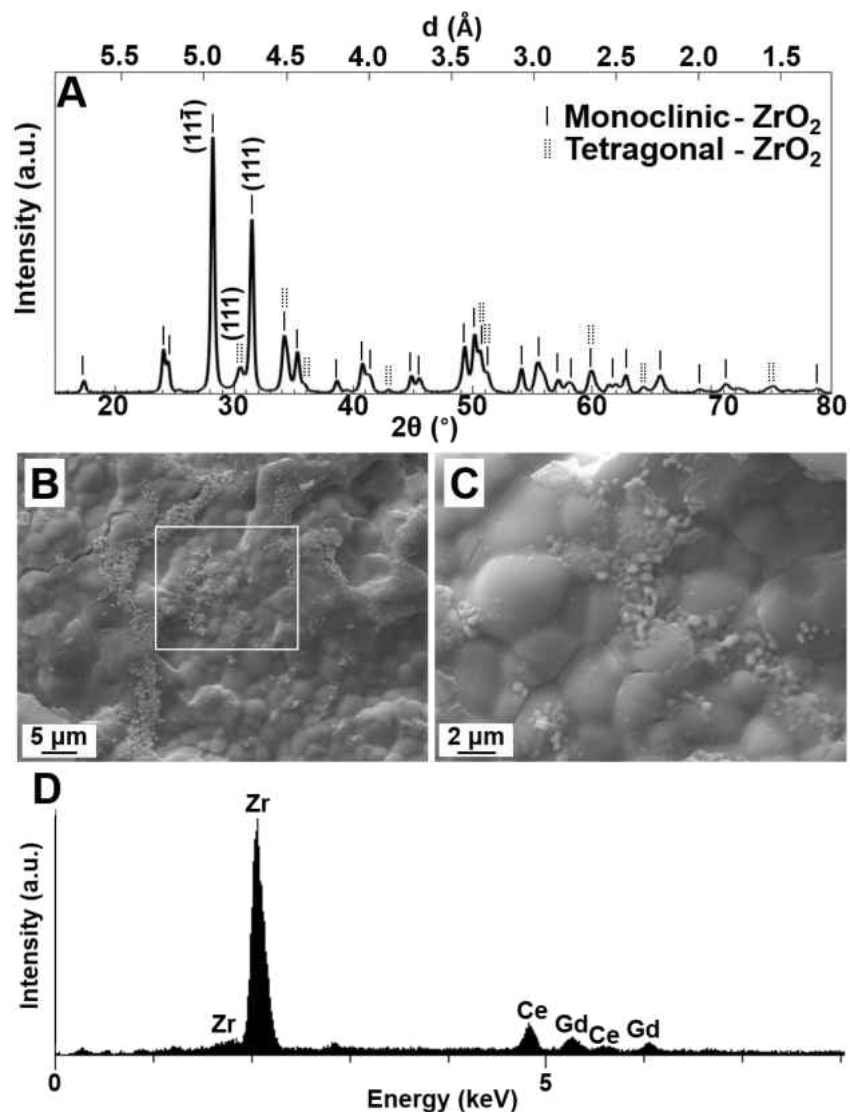


Figure 3-17: (A) X-ray diffraction pattern; (B) and (C) SEM micrographs and (D) EDS spectrum of the 3 wt% MgO stabilized  $\text{ZrO}_2$  porous media with  $\text{Ce}_{0.2}\text{Gd}_{0.8}\text{Ce}_{1.9}$  coating.

### 3.5.2. *La Based Perovskites*

From Figure 3-18 through Figure 3-21, X-ray diffraction patterns, SEM micrographs, and EDS spectra are presented for each of the lanthanum based perovskites evaluated as catalysts and correspond to  $\text{LaCoO}_3$ ,  $\text{La}_{0.80}\text{Ca}_{0.20}\text{CoO}_3$ ,  $\text{La}_{0.75}\text{Sr}_{0.25}\text{Cr}_{0.95}\text{Ru}_{0.05}\text{O}_3$ , and  $\text{La}_{0.75}\text{Sr}_{0.25}\text{Fe}_{0.95}\text{Ru}_{0.05}\text{O}_3$ , respectively. From each of the XRD patterns it can be seen that each perovskite is phase pure.

From the micrographs it can be seen that the catalyst powders are large agglomerations of individual particles.

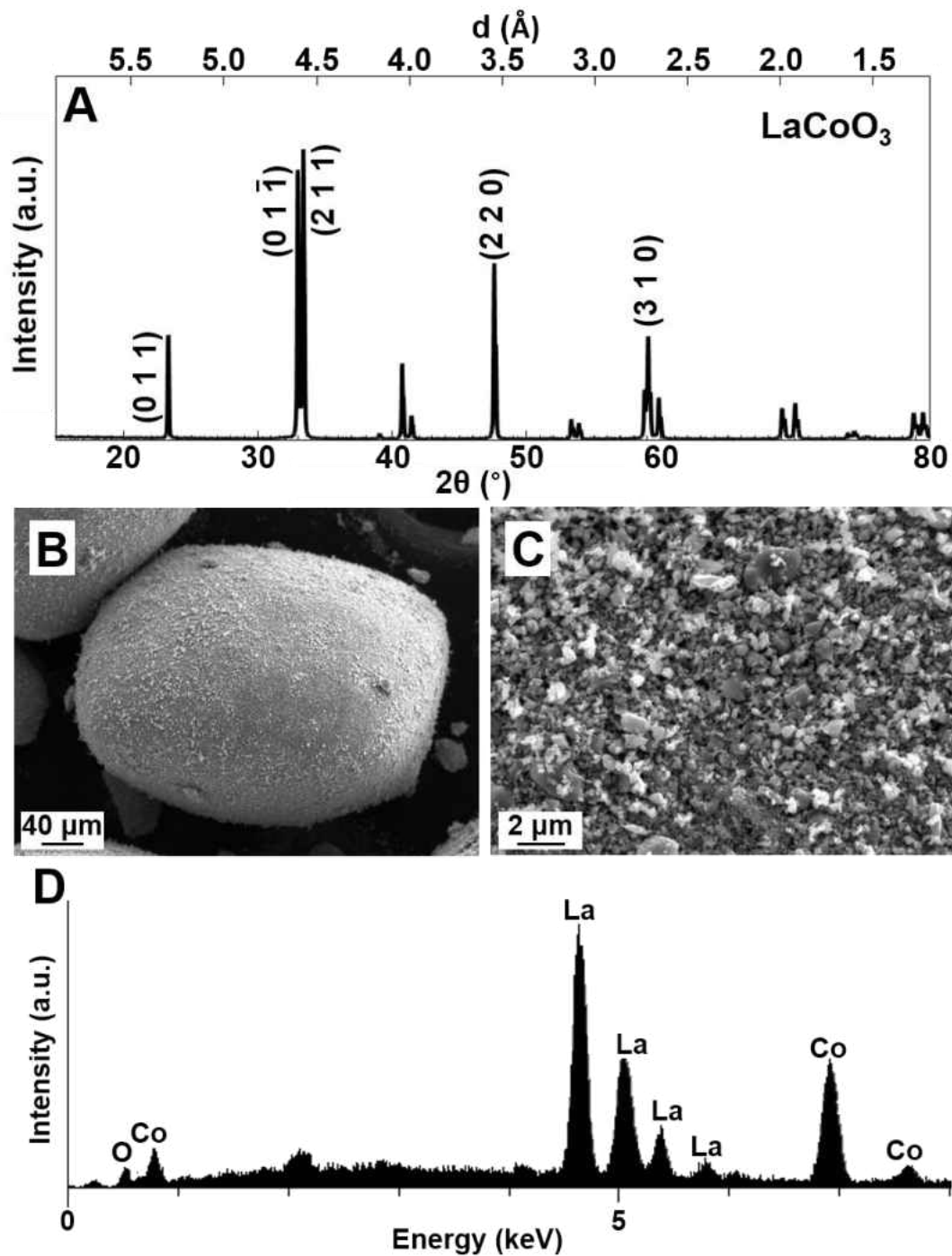


Figure 3-18: A) XRD pattern, (B and C) SEM micrographs, and D) EDS spectra of LaCoO<sub>3</sub>.

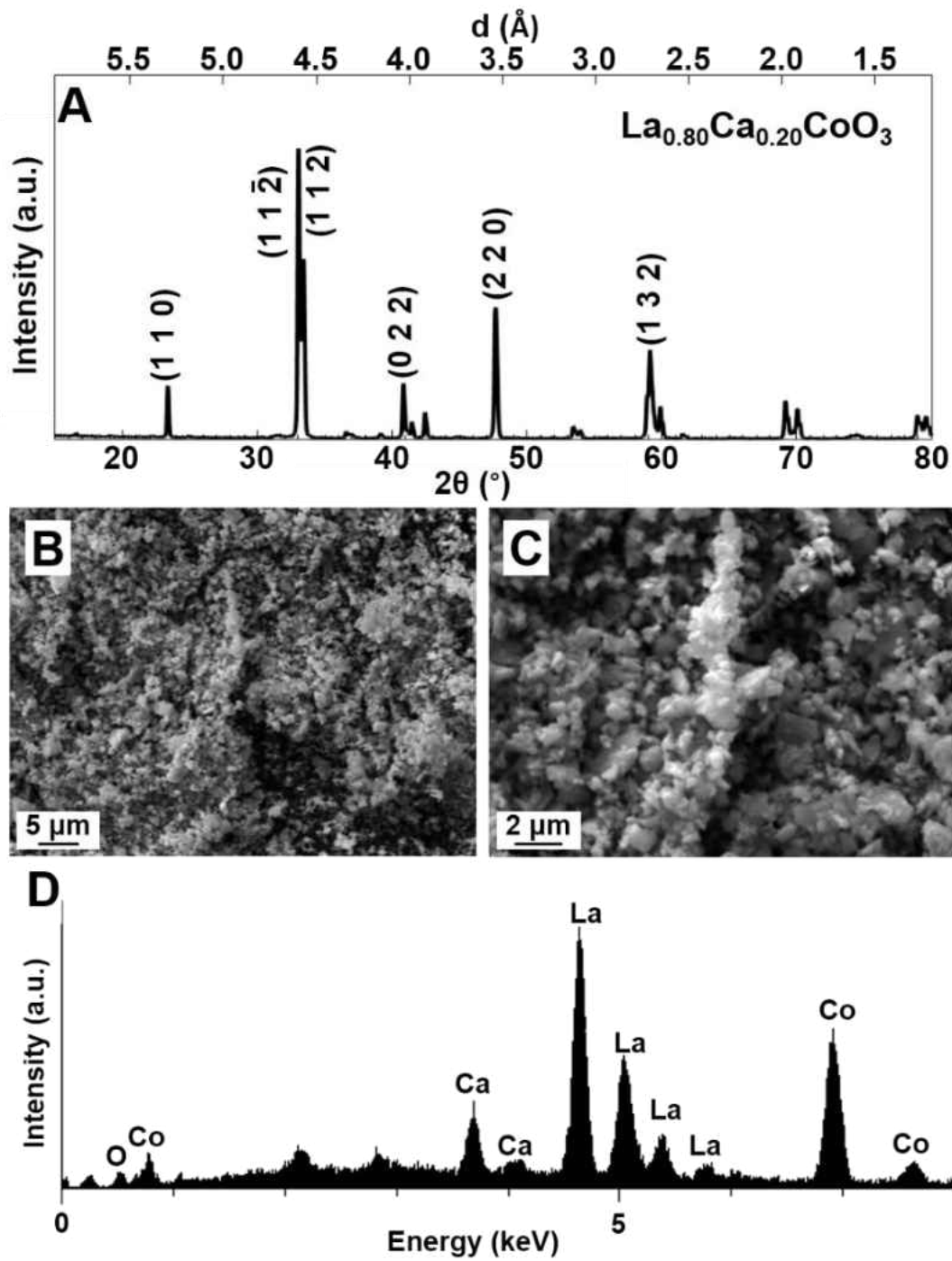


Figure 3-19 A) XRD pattern, (B and C) SEM micrographs, and D) EDS spectra of  $\text{La}_{0.80}\text{Ca}_{0.20}\text{CoO}_3$

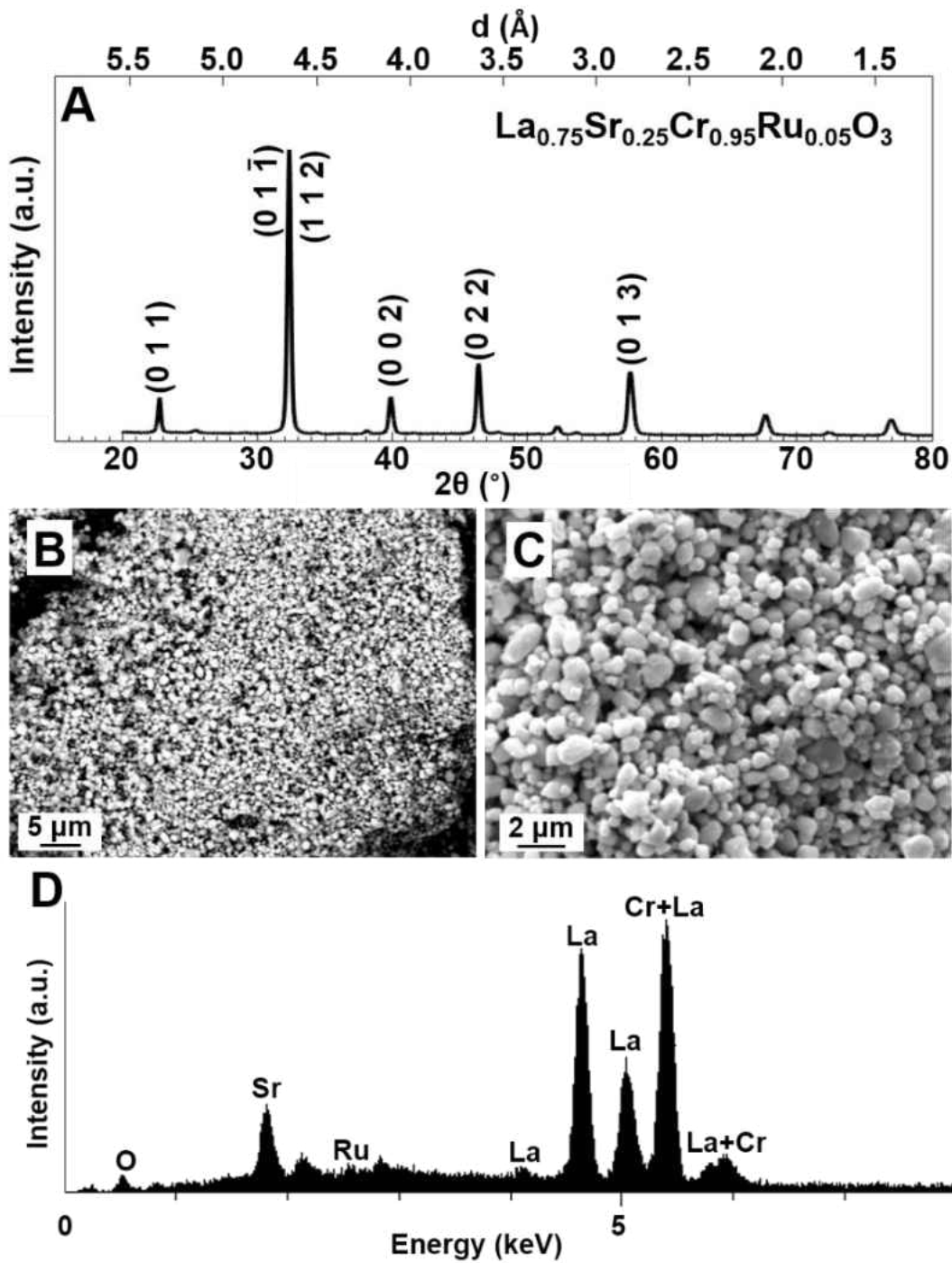


Figure 3-20: A) XRD pattern, (B and C) SEM micrographs, and D) EDS spectra of  $La_{0.75}Sr_{0.25}Cr_{0.95}Ru_{0.05}O_3$ .

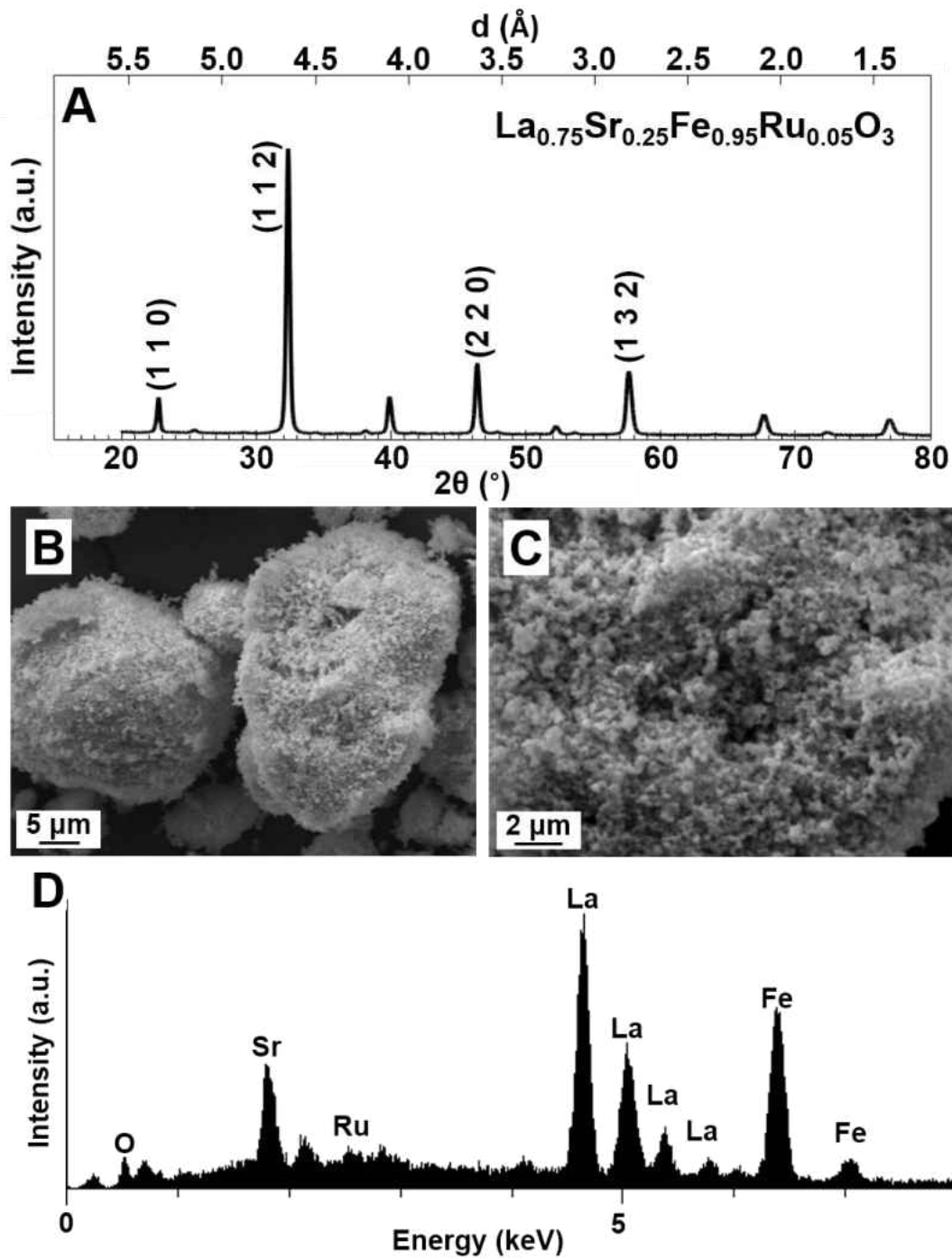


Figure 3-21: A) XRD pattern, (B and C) SEM micrographs, and D) EDS spectra of  $\text{La}_{0.75}\text{Sr}_{0.25}\text{Fe}_{0.95}\text{Ru}_{0.05}\text{O}_3$ .

A representative coating of the perovskites on the substrates is shown in Figure 3-22, which presents information on the  $\text{LaCoO}_3$  catalyst coating through multiple means. An XRD pattern presented in A shows the relative mass fraction of the  $\text{LaCoO}_3$  catalyst on the surface of the MSZ media. Within B and C SEM images of the  $\text{LaCoO}_3$  coated MSZ surface are shown, and in D the EDS spectra of a selected region within the micrographs. From the figure it can be seen the  $\text{LaCoO}_3$  coating has a significantly higher mass fraction than the GDC as it is measureable within the diffraction pattern. However, even with this higher mass fraction of catalyst coating, regions of GDC and uncoated MSZ can still be seen.

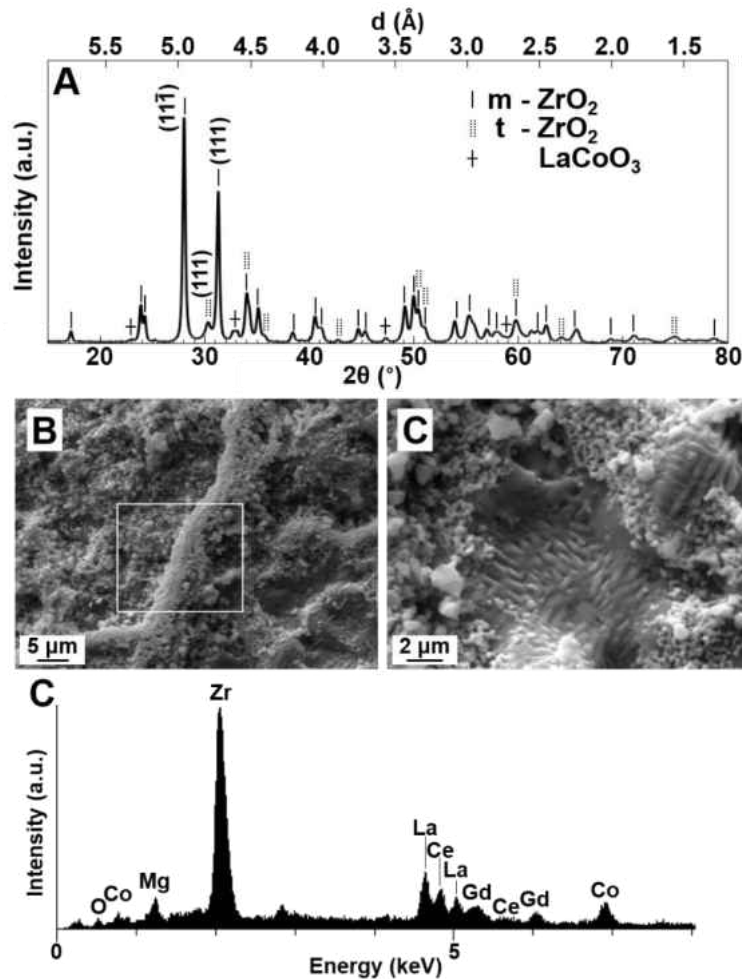


Figure 3-22: A) XRD pattern, (B and C) SEM micrographs, and D) EDS spectra of  $\text{LaCoO}_3$  on GDC coated MSZ media.



### 3.5.3. *Tungsten Carbide Enhanced Palladium*

Pd enhanced WC catalyst particles were prepared using a mechanochemical route [169]. Dip coating was used to deposit WC-Pd particles onto the surface of partially stabilized MgO-ZrO<sub>2</sub> (MSZ) porous media [152, 170]. The catalytically enhanced MSZ porous media was further tested using a previously developed porous combustor system.

The powdered Pd enhanced WC particles were prepared using mechanochemical route. Pd metal foils 0.5-0.75 mm thick and 5-10mm in length were milled in a WC grinding vial using WC balls as a source of WC. Within the vial, impacts of the WC balls acted to reduce the size of the Pd foils and transform them into small particles, while causing fracturing of the outer grains from the WC balls. The high energy ball milling was employed using SPEX 8004 ball mill (SPEX Sample Prep: Metuchen, USA).

Procedures of catalyst particle synthesis is as follows: (1) mixing ascorbic acid (C<sub>6</sub>H<sub>8</sub>O<sub>6</sub>) (0.100±0.0025g), Pd metal scraps (0.200±0.0035g) and sodium chloride (anhydrous NaCl) (1.000±0.0060g) into SPEX tungsten carbide (WC) lined grinding vial. Four 12.7mm WC balls were placed in the vial to be used in the grinding process. The total grinding time was 4 hours; however, a periodic grinding procedure was used and grinding of the batch took 8 hours, since the vials shook at 1200 cycles/min for 30 minutes, followed by a 30 minute dormant period to reduce the temperature of the vial and its contents. In this method, ascorbic acid was used as a stabilizing agent keeping the Pd particles separate by coating their surfaces and helping to reduce the surface energy of the Pd. Ascorbic acid also acted as a reducing agent to facilitate the extraction of WC from the vial, added NaCl to the vial functioned as a diluting agent with virtually no contribution to the high energy grinding process.

After milling, the solid product extracted from the vials was a black fine powder of WC-Pd metal particles with ascorbic acid on the surface coated with a layer of NaCl. Small WC-Pd particles had a black color due to intensive light scattering. This black powder was further mixed with deionized water and excited ultrasonically to prepare a proper suspension for dialysis to remove  $\text{Na}^+$  and  $\text{Cl}^-$  ions as well as any unbound ascorbic acid. Once the aqueous suspension was prepared, it was transferred into dialysis tubes, which were placed into a large basin of deionized water and allowed to sit for 80 hours. Following the dialysis process, the fine powder was separated from the aqueous solution using a vacuum filtration system where the product was collected using a polycarbonate nuclepore membrane filter (name of the manufacture, GE). After vacuum filtration the final product of fine WC-Pd particles coated with the surface passivating layer of ascorbic acid was placed into a Petri-dish and placed into an oven at 80 °C for four hours to remove any residual water.

The produced powder was characterized using X-ray diffraction (XRD, PANanalytical Empyrean, Almelo NL), X-ray Fluorescence (XRF, PANanalytical Epsilon 1, Almelo NL), and scanning electron microscopy (SEM, Zeiss EVO-10MA, Oberkochen DE) with an energy dispersive x-ray spectroscopy detector (EDS, IXRF Systems, Austin USA) to determine phase, chemical composition, and morphology of the powder.

A simple and efficient dip coating method was utilized to deposit catalytically active WC-Pd particles onto the surfaces of the MSZ porous ceramic media used as a space holder of the flame in heterogeneous combustion [170]. Commercially available MSZ highly porous ceramic matrix which is comprised of 97 wt-%  $\text{ZrO}_2$ , 10~20 % cubic phase with the remaining  $\text{ZrO}_2$  in the monoclinic phase, and 3 wt% MgO was used as a media to support the combustion reactions [152].

The MSZ media had a porosity of 10 pores per inch (ppin) with a length of 50.4mm and a diameter of 50.0mm. Before dip coating, the whole media is immersed in an ultrasonically excited acetone bath followed by a drying process to remove any organic residue and debris from the media surface which would compromise the catalyst coating process. A suspension of approximately 1g WC-Pd powder was mixed with 200 ml deionized water under ultrasonic excitation and the MSZ porous media was immersed into the WC-Pd in water suspension for 15 seconds. To achieve an even distribution of WC-Pd particles on the surface of ceramic matrix, the immersion process was repeated 20 times, between each immersion the media was allowed to drip dry in air for about 2 minutes after each immersion in the catalyst suspension. Such repeated immersion of ceramic media into suspension of WC-Pd particles in water ensured the consistent and homogeneous color of the media, which would not change after consequent last 5 immersions. In Figure 3-23, a comparison of the MSZ before and after catalyst coating is presented.

A photograph comparing the coated and uncoated MSZ media with Pd enhanced WC catalyst is shown in Figure 3-23.

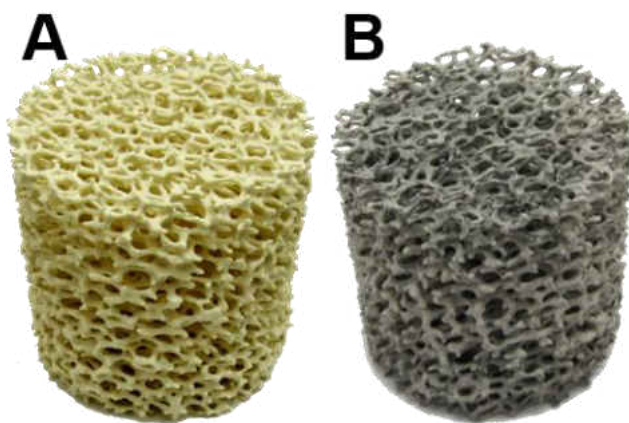


Figure 3-23 (A) Uncoated MgO-ZrO<sub>2</sub> media. (B) Pd enhanced WC coated MgO ZrO<sub>2</sub> media.

A scanning electron micrograph of the WC-Pd fine particles assembled into a significantly larger agglomerate is shown in Figure 3-24. As one can see from Figure 3-24, the size of the individual particles is between 0.2 and 0.3  $\mu\text{m}$  which comprise an agglomerate on the order of 100  $\mu\text{m}$ . An EDS analysis performed on the surface of the agglomerate shows the presence of W as a major element supplemented by Co, O, and C; as WC alloy consist of WC particles bound in a matrix of metallic Co. In addition to W, C, O, and Co; Pd was also detected in the batch as expected.

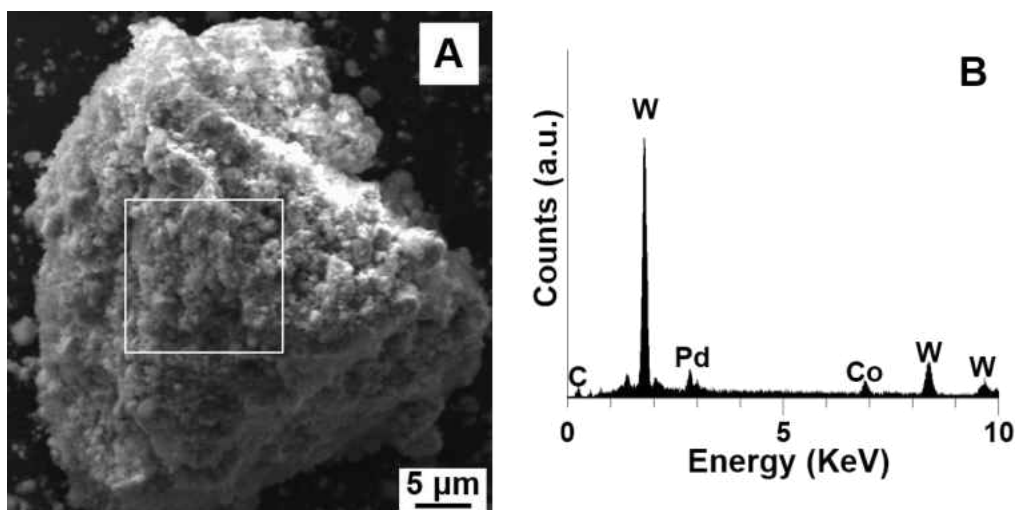


Figure 3-24: (A) SEM SE micrograph of WC-PD catalyst powder showing detail of crystallite surface and location of EDS. (B) Selected area EDS of WC-Pd catalyst powder.

An X-ray diffraction pattern of the synthesized WC-Pd powder is shown in Figure 3-25. While major peaks of the pattern were identified as belonging to WC ( $P\bar{6}m_2$ ) [171], the minor and much weaker peaks were identified as belonging to  $\text{Co}_3\text{O}_4$  (F-43m) [172], PdO ( $P4_2/mmc$ ) [173] and Pd ( $Fm\bar{3}m$ ) [174]. XRF analysis of the chemical composition of the powder revealed that WC and Pd provides more than 95 wt% of the total quantities, with such impurities as P, Cl, C, Ge and Hf providing the rest. The quantity of major elements were as follows: W-83.7 wt-%,

Co-5.5 wt-%, and Pd – 6.0 wt-%. It is of note that this particular XRF instrument is unable to accurately characterize concentrations of elements lighter than sodium.

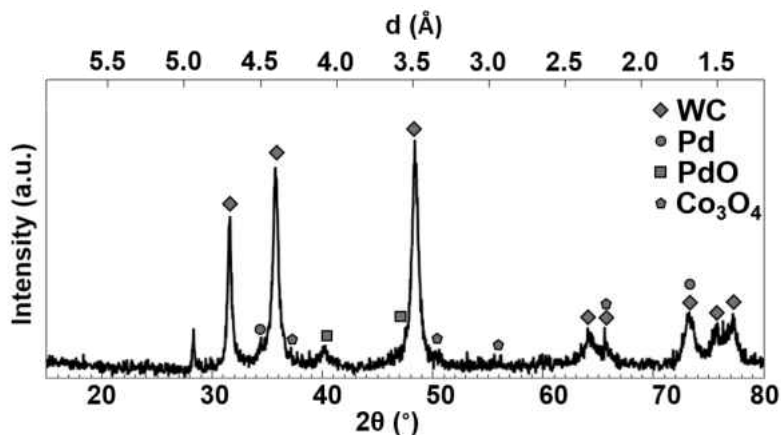


Figure 3-25: X-Ray Diffraction pattern of the WC-Pd catalyst powder.

Within Figure 3-26, secondary electron and back scattered micrographs are presented which show the surface morphology and Z contrast of the Pd enhanced WC coating on the surface of the MSZ media along with an EDS of the area within the micrograph.

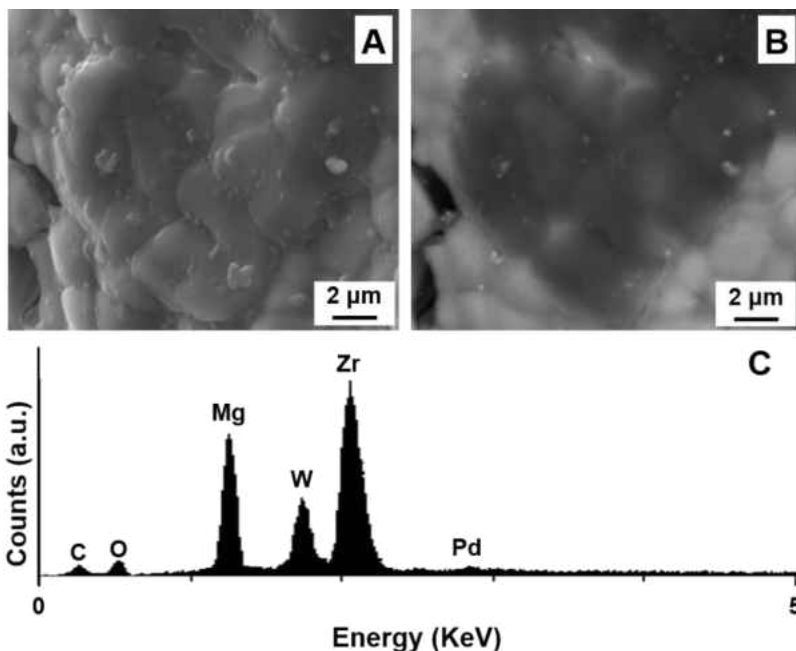


Figure 3-26: Scanning electron micrographs of the surface of MgO-ZrO<sub>2</sub> porous media coated with WC-Pd. (A) secondary electron and (B) back scattered detector micrograph. (C) EDS of the region of surface depicted in the micrographs.

### 3.5.4. Zirconium Diboride

ZrB<sub>2</sub> powders were milled using a procedure described elsewhere [175] to reduce the particle size of the as received powders. These powders were characterized via XRD, SEM, and EDS techniques. Such information is presented in Figure 3-27. From the micrographs, it can be seen that individual crystals are on the order of 2 microns with many abruptly terminating surfaces.

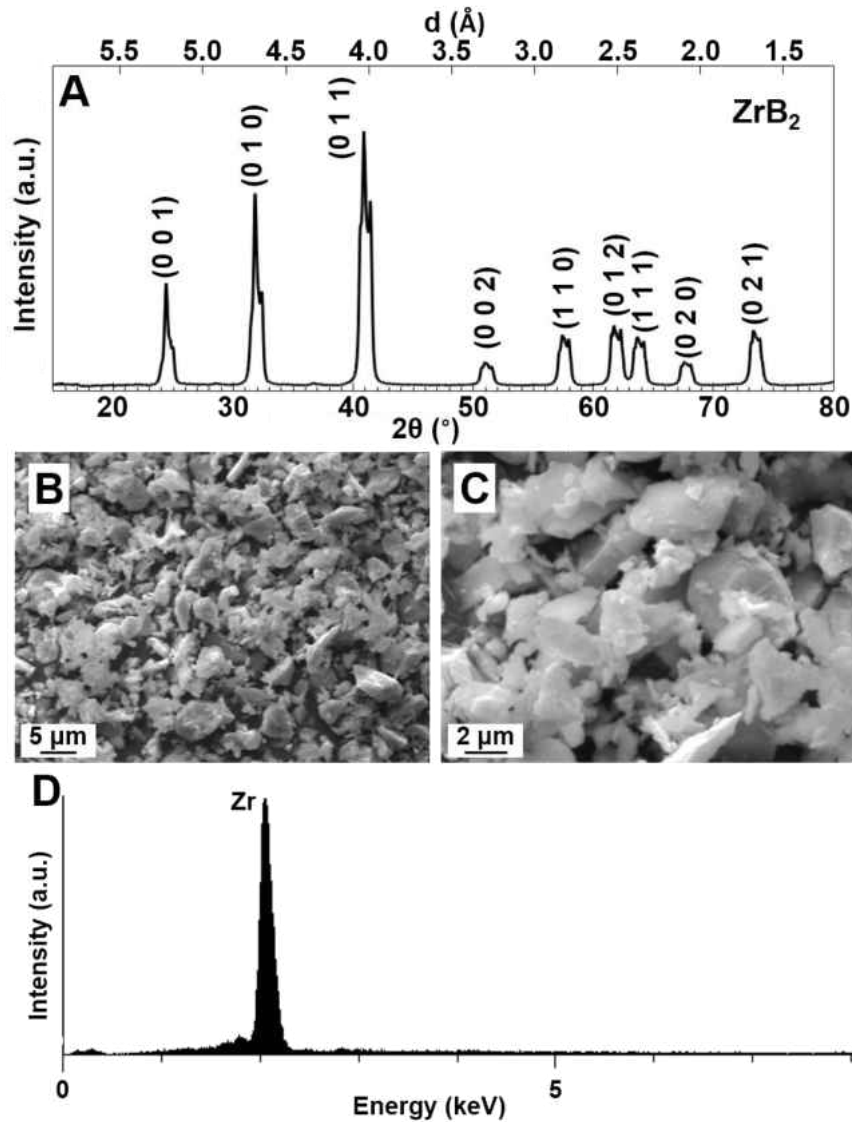


Figure 3-27: (A) BSD Electron micrograph image of catalyst coated surface, with selected area EDS shown. (B) Close up BSD electron micrograph of EDS region. (C) BSD micrograph of EDS region. (D) SE micrograph of EDS region.

From within Figure 3-28, SEM micrographs reveal the coated surface of the ZrB<sub>2</sub> catalyst on the MSZ media. The corresponding EDS in the figure shows the presence of Mg and Zr atoms, B is unrecognizable by the detector.

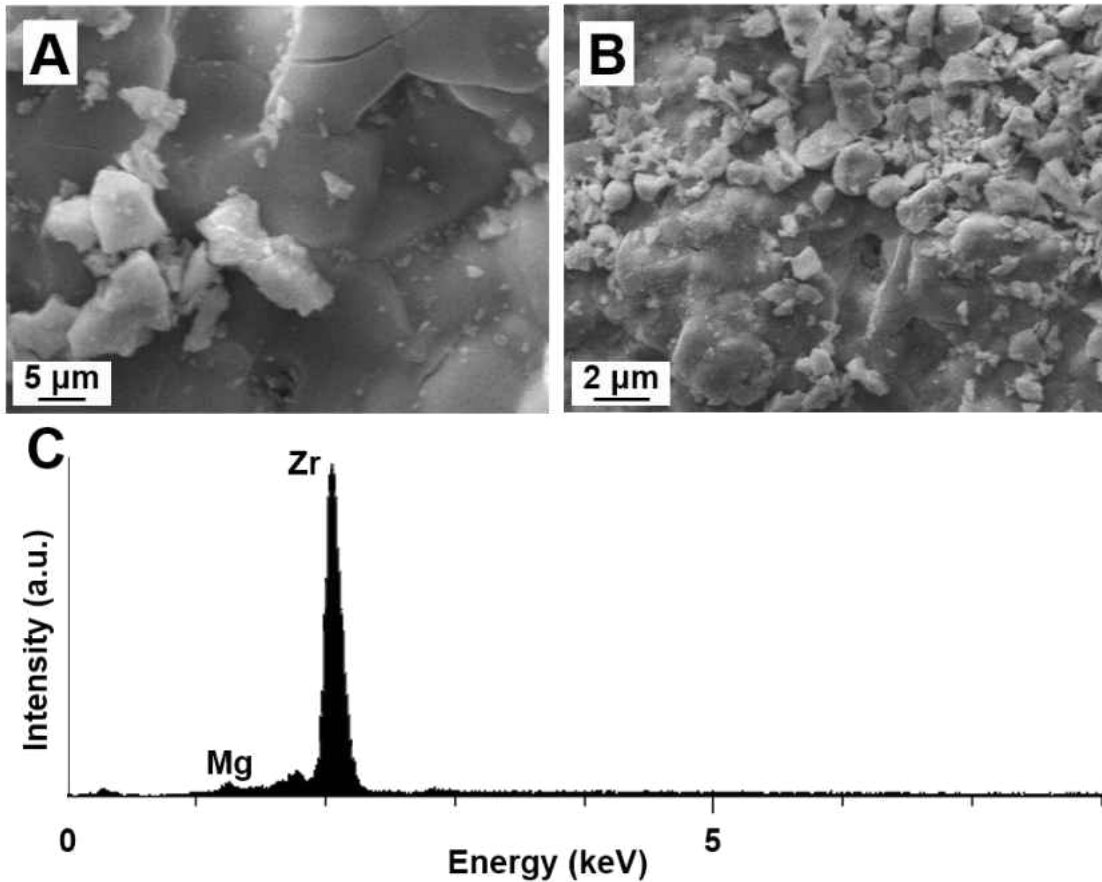


Figure 3-28: (A and B) SE Electron micrograph image of the ZrB<sub>2</sub> catalyst coated MSZ media surface, with selected area EDS shown. (C) EDS spectra of regions within micrographs.

### 3.6. Summary

A heterogeneous combustor was designed and developed allowing for the utilization of different highly porous ceramic media to house and regulate a flame. A unique combustor design enables control of the flame position within the porous media by regulating reactant flow rates, unlike in all other combustors presented in the literature thus far, where the only way to keep the flame inside the porous media was by employing flow-conditioning devices to prevent the flame

from moving outside of the porous media. The heterogeneous combustor system within this work consists of the combustor chamber, reactant storage and metering system, the reactant delivery nozzle as well as exhaust sampling port through which the gases can be tested using an externally connected gas chromatograph. In order to collect the relevant data needed to perform analysis of how the combustor operates, several instrumentation methods were incorporated into the experimental setup, such as (i) temperature measurements by thermocouples, (ii) acoustic emissions measurements by a microphone, (iii) optical imaging using CCD camera, and (iv) analysis of exhaust gas composition using a gas chromatograph with a thermal conductivity detector.



## 4. EXPERIMENTAL OBSERVATIONS

### 4.1. Introduction

Within this research topic the heterogeneous combustor designed and presented in chapter 3 was operated as the environmental chamber to evaluate heterogeneous catalyst coated onto MSZ media. To present the results herein, the combustion chamber was operated for a total of nearly 500 hours without the need to replace any components. Experimental results obtained using  $\alpha$ -Al<sub>2</sub>O<sub>3</sub> media are presented in Table 4-1. Within the table a list of reactant flow rates and equivalence ratios are presented these reactant flow rates and equivalence ratios are maintained for all of the different experiments performed within the given tolerances.

**Table 4-1: Experimental results obtained using the developed heterogeneous combustor, where the maximum measured temperature and equivalence ratio along with total, air and methane flow rates are presented as a function of time when the data points were collected with an  $\alpha$ -Al<sub>2</sub>O<sub>3</sub> immersed media.**

<b>t (min)</b>	<b>T<sub>max</sub> (°C)</b>	<b><math>\phi \pm 0.02</math></b>	<b><math>\dot{V}</math> (SLPM)</b>	<b><math>\dot{V}_{air}</math> (SLPM)</b>	<b><math>\dot{V}_{CH_4}</math> (SLPM)</b>	<b>S.S.</b>
<b>0.0</b>	-	1.00	27.15±0.61	24.57	2.58	No
<b>4.2</b>	279.7±3.2	1.00	27.15±0.61	24.57	2.58	No
<b>23.5</b>	630.6±5.2	0.80	51.59±0.61	47.56	4.00	No
<b>90.0</b>	728.8±5.9	0.75	51.31±0.61	47.56	3.75	Yes
<b>100.4</b>	723.2±5.9	0.73	51.21±0.61	47.56	3.65	Yes
<b>119.6</b>	713.7±5.8	0.71	51.11±0.61	47.56	3.55	Yes
<b>129.7</b>	704.4±5.7	0.69	51.01±0.61	47.56	3.45	Yes
<b>143.5</b>	692.7±5.7	0.67	50.91±0.61	47.56	3.35	Yes
<b>163.4</b>	678.9±5.6	0.65	50.81±0.61	47.56	3.25	Yes
<b>185.5</b>	665.0±5.5	0.63	50.71±0.61	47.56	3.15	Yes
<b>206.4</b>	651.8±5.4	0.61	50.61±0.61	47.56	3.05	Yes
<b>228.4</b>	638.4±5.3	0.59	50.51±0.61	47.56	2.95	Yes
<b>257.4</b>	626.3±5.2	0.57	50.41±0.61	47.56	2.85	Yes
<b>272.7</b>	617.2±5.1	0.55	50.31±0.61	47.56	2.75	Yes
<b>294.2</b>	601.6±5.0	0.53	50.21±0.61	47.56	2.65	Yes
<b>369.2</b>	536.9±4.6	0.51	50.11±0.61	47.56	2.55	Yes
<b>449.0</b>	313.7±3.3	0.49	50.01±0.61	47.56	2.45	Yes
<b>459.8</b>	256.7±3.0	0.47	49.92±0.61	47.56	2.36	No

While operating the combustor at lower equivalence ratios, there is a severe instrumentation limit and it becomes difficult to distinguish the presence of a flame and therefore it is difficult to directly measure the lower light-off temperatures of the catalyst at these prescribed flow rates. It is apparent that temperatures recorded are well below the adiabatic flame temperatures for mixtures at these equivalence ratios and thus it is my belief that even while the combustor was operating near the lean limit, a significant fraction of methane was not oxidized. While it may be possible to utilize the catalyst and substrates combinations at lower equivalence ratios than what is tested here, additional instrumentation is needed.

#### **4.2. Observations of the Combustor Using Al<sub>2</sub>O<sub>3</sub> Media**

A typical time dependent temperature distribution within the combustion chamber measured over the course of the entire experiment as a function of equivalence ratio is shown in Figure 4-1. Results presented in Figure 4-1 can be broken into three stages: (i) ignition; (ii) heating up; and (iii) fuel flow rate/equivalence ratio reduction. Ignition, which occurs at 30 seconds into the experiment, is followed by the heating up stage, which takes ~18.6 minutes following the ignition event. The remainder of the experiment was conducted under increasingly lean conditions to determine the lowest possible equivalence ratio, where the flame is still stable for the given media composition, dimensions, porosity, and external heat loss. Both axial temperature measurement of the combustion chamber and acoustic profiles are utilized to confirm the existence of a stable flame. As one can see from Figure 4-1, the lowest possible lean limit of the stable flame was observed at  $\phi=0.49\pm 0.02$  since a subsequent decrease in equivalence to  $\phi =0.47\pm 0.02$  induces a rapid decrease in the temperature across the combustion chamber, until the minimum necessary reaction rates for combustion could not be sustained.

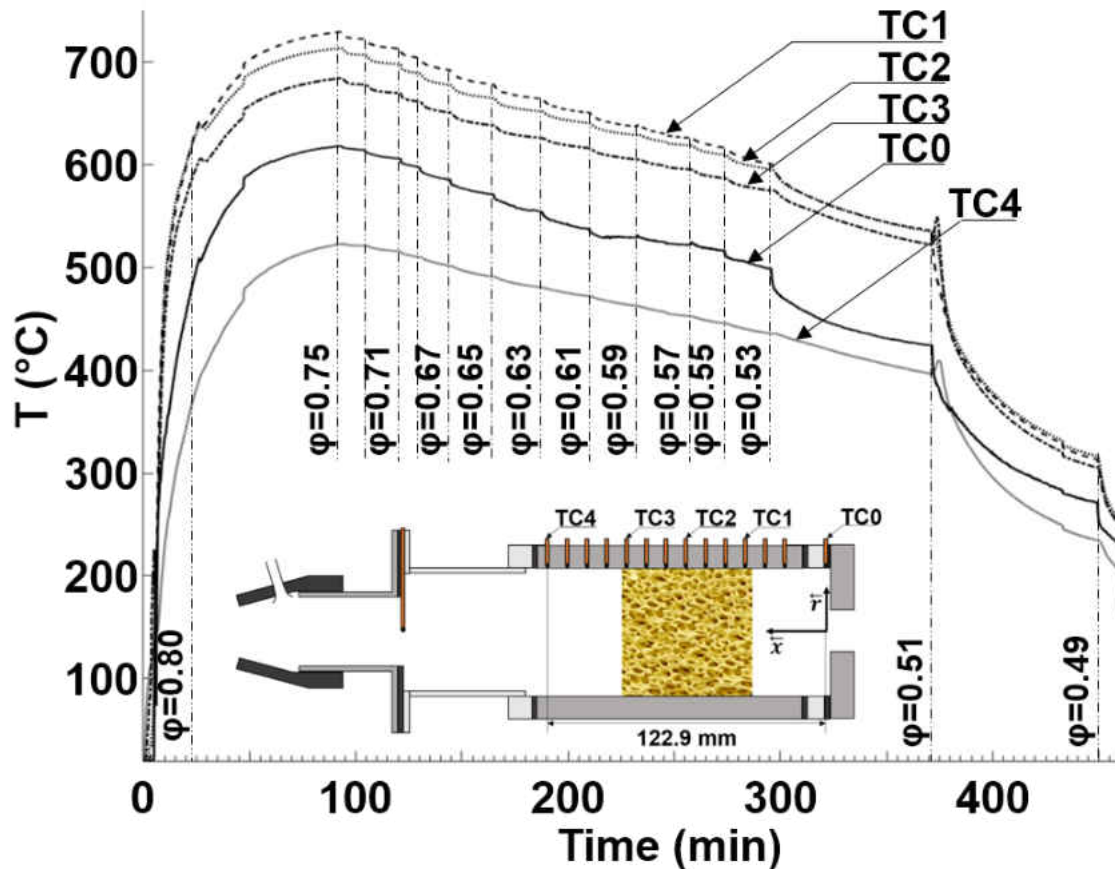


Figure 4-1: Time evolution of selected thermocouples, shown with steady state burning delineations at each equivalence ratio.

At the beginning of the experiment, a mixture of air and methane with  $\phi=1.00\pm 0.02$  and total flow rate of  $\dot{V}=27.15\pm 0.61$  SLPM was passed through the combustor from the inlet. A pilot flame was inserted into the combustor exhaust, which ignited the gaseous mixture (Figure 4-2 A-1). Once ignited the laminar flame speed of the stoichiometric mixture would exceed the total reactant flow rate, causing the flame front to propagate from the exhaust side of the combustion chamber toward the inlet, Figure 4-2 A-2; until the flame is finally settled between the porous media and reactant inlet (Figure 4-2 A-3). While the flame is transient immediately following ignition, temperatures observed within the combustion chamber are highly chaotic, fluctuating as the flame moves (Figure 4-2 B); simultaneously during this period no acoustic signal

between 200 and 500 Hz observed (Figure 4-2 C). Once the flame reaches a stable position between the porous media and combustion chamber inlet, the first acoustic emission signal at 4.1 minutes is observed featuring a high amplitude peak at 318.6 Hz, and is loud enough that the noise can easily be recognized by the human ear.

When the acoustic signal at 318.6 Hz appeared at 4.1 minutes into the experiment, the air and methane flow rates are quickly increased within 30~60 seconds to the total flow rate of  $\dot{V}=51.59\pm 0.61$  SLPM while simultaneously reducing the equivalence ratio to  $\phi=0.80\pm 0.02$ , causing the flame to propagate into the combustion media Figure 4-2 A-4. Such a rapid change in the reactant delivery is performed in order to prevent damage to the combustion chamber by standing acoustic waves [176]. These waves, which are composed of many simultaneous modes or unique oscillations, can exist with a stable spatial structure producing a distinct acoustic emission which is a linear combination of each individual mode [177]. It is also possible that, if sufficient intensity of a given mode pertaining to chemical reaction waves are present, then, a self-excitation of additional acoustic modes can occur [10, 178]. In conventional combustors, excitations of certain acoustic modes can lead to sub-optimal combustor performance and damage to the combustion chamber; in the case of heterogeneous combustors, an additional concern is the possibility of acoustic pressure variations fracturing the porous ceramic immersed within the combustion chamber [179].

The acoustic emission signal recorded at 8.8 min (Figure 4-2 C) when  $\phi=0.80\pm 0.02$  and the total flow rate was  $\dot{V}=51.59\pm 0.61$  SLPM shows two prominent peaks centered at 348.1 Hz and 380.9Hz with two substantially weaker peaks between [200Hz, 245Hz] and [269Hz, 330Hz] indicating the flame location is now submerged within the span of the porous media inside the

combustion chamber. Similarly, confirmation of the flame location can be made via the temperature profiles in Figure 4-2 B when temperatures measured by thermocouples TC1 and TC2 show rapid increase, and obviously these temperatures are the highest ones within the combustion chamber across that time period. It should be noted, that as time progresses from 8.8 min to 19.3 min with no changes being made to the total reactant flow rate or equivalence ratio, that the intensity and symmetry of the 364.8 Hz peak increases. This flow rate is maintained up to 23.5 minutes of the experiment, when a further decrease in the methane flow rate is made, bringing the equivalence ratio to  $\phi=0.75\pm0.02$ .

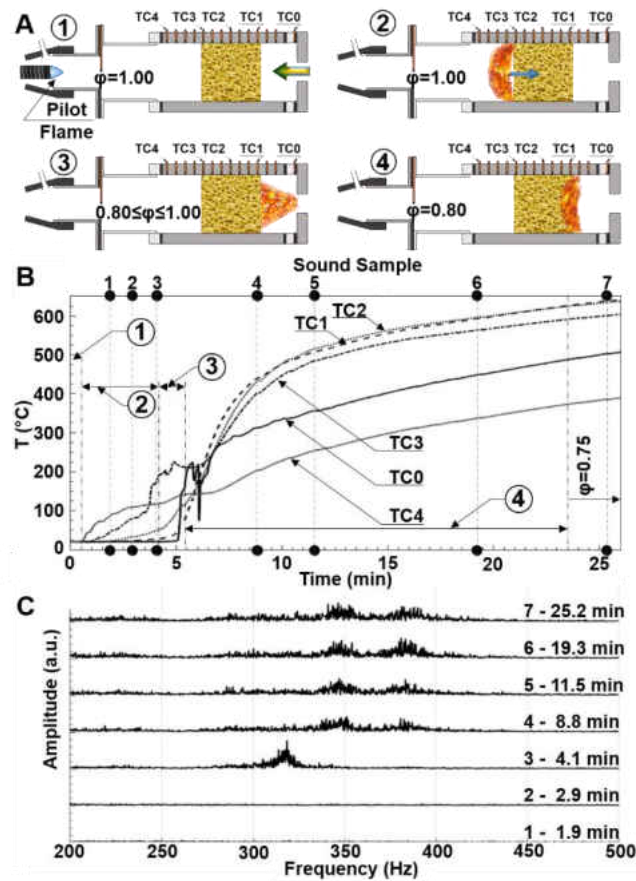


Figure 4-2: (A) Flame at various positions within the combustion chamber shortly after ignition. (B) Time evolution of selected thermocouples during ignition and warm up. (C) Acoustic profiles at selected times.

Within the presented experimental work the longest period of time required for the temperature to reach a steady state is when the equivalence ratio was instantaneously changed from  $\phi=0.51\pm 0.02$  to  $\phi=0.49\pm 0.02$ , with  $\phi=0.49\pm 0.02$  being the lowest equivalence ratio which maintained a stable flame within the experimental combustor using an  $\alpha\text{-Al}_2\text{O}_3$  porous media. These results obtained during the last 83 minutes of the experiment are presented in Figure 4-3. As one can see from Figure 4-3 all five thermocouples located along the combustion chamber showed almost no change in temperature for a short period, about 2.5 minutes, at the beginning of this stage this quasi-isothermal period was followed by another short period of time, 4.9 minutes, in which temperatures increased, as measured by thermocouples TC3 and TC4 located toward the exhaust, while temperatures decreased, as measured by thermocouples TC0, TC1, and TC2 located closer to the inlet of the combustion chamber. Such fluctuation in temperature distribution indicates that the flame front moves rapidly toward the exhaust. Following the rapid repositioning of the flame, while the equivalence was  $\phi=0.49\pm 0.02$ , the temperatures measured by thermocouples TC1, TC2, and TC3 become increasingly uniform indicating that the intensity of the flame becomes nearly constant through the length of the porous media. Following this flame redistribution, a continued gradual temperature decrease is observed at all of the thermocouples until a steady state is finally achieved at 449.0 minutes.

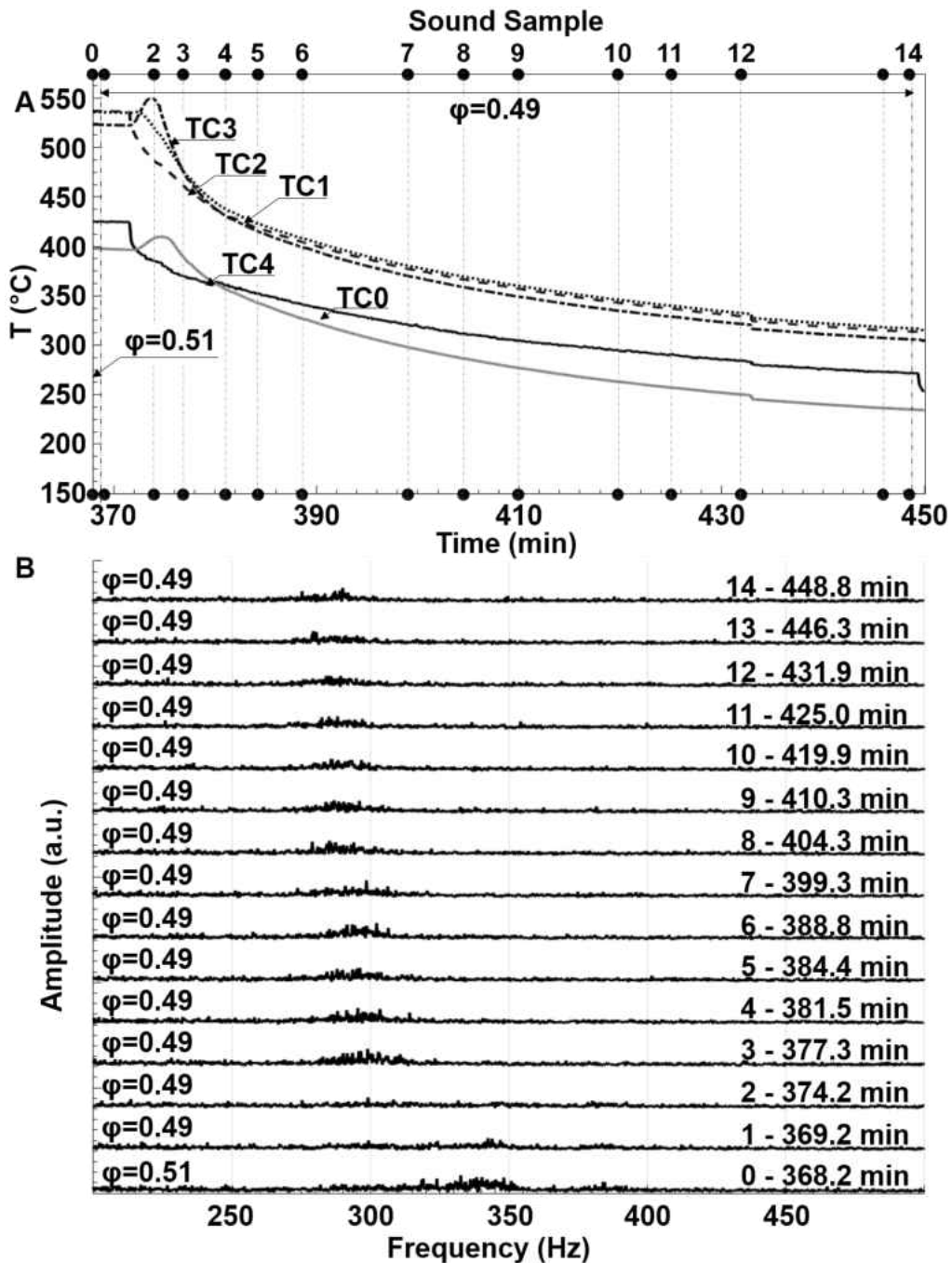


Figure 4-3: A) Time evolution of selected thermocouples within the combustion chamber between the achieved steady state at  $\phi=0.51$  to  $\phi=0.49$ , vertical lines on the plot indicate when acoustic profiles were recorded. B) Acoustic profiles recorded at various times as the combustor approaches steady state following the  $\phi=0.51$  to  $\phi=0.49$  transition.

Correlation can be found between changes in temperature measurements, via axial thermocouples, and the corresponding acoustic emission collected simultaneously by the

microphone during this segment of the experiment. At 368.2 minutes, while the equivalence ratio was  $\phi=0.51\pm0.02$ , just prior to being lowered to  $\phi=0.49\pm0.02$ , two very weak and diffuse peaks which were detected in the acoustic emission spectrum. One very broad peak centered at 340.4 Hz and a second peak centered at 384.2 Hz of significantly lower intensity (Figure 4-3 B). However, once the equivalence ratio was decreased to  $\phi=0.49\pm0.02$  at 369.2 minutes of the experiment, these two peaks in the acoustic spectra disappeared for the following recordings taken at 369.2 to 374.2 minutes, which occurred during the time coinciding with quasi-isothermal behavior and subsequent flame propagation (Figure 4-3). Such absence of an acoustic signal over this spectral range was also observed shortly after ignition, while the flame was propagating toward the inlet (Figure 4-2 C) indicating movement or elongation of the flame, which could be characterized by the absence of sound in this spectral range. For the rest of the acoustic measurements, starting from 377.3 minutes, a monotonic decrease in amplitude and shift of peak position to lower frequencies was observed until the steady state was reached at 449.0 min (14).

The time dependent temperature profiles and their more detailed analysis were presented in Figure 4-2, but it is also convenient to analyze axial temperature profiles at different steady states, which correspond to different equivalence ratios. Such axial temperature profiles shown along with the length of the combustion chamber are shown in Figure 4-4, where one can see that the highest temperature of  $725.1\pm5.9$  °C measured at the location within porous media most closely located toward inlet of the combustion chamber was achieved during the combustion of the mixture at  $\phi=0.75\pm0.02$ . As one can see from Figure 4-4, each reduction of equivalence ratio induces a corresponding decrease in temperatures along the whole length of the combustion chamber. When the equivalence ratio ranges between  $\phi=0.75\pm0.02$  to  $\phi=0.59\pm0.02$  the reduction



in temperature along the combustion chamber is almost directly proportional to the reduction in the equivalence ratio.

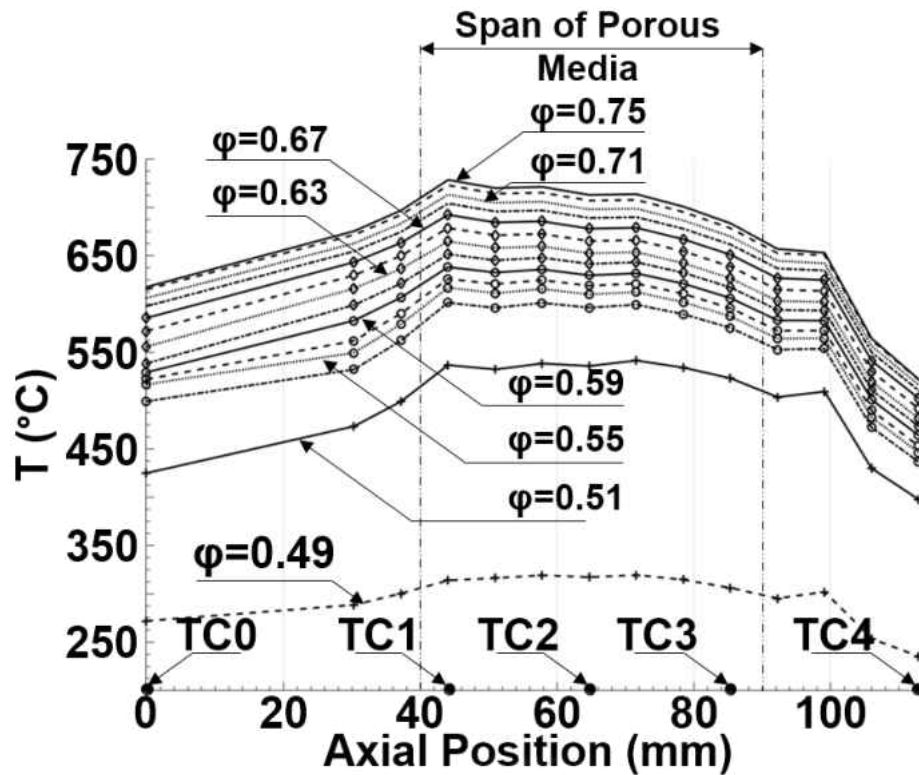


Figure 4-4: Observed temperature profiles across the combustion chamber at given equivalence ratios.

The corresponding acoustic profiles for each steady state are presented in Figure 4-5. As one can see from Figure 4-5, acoustic emissions within the 200 and 500 Hz spectrum can be separated into four distinct peaks, which are more predominantly visible at higher equivalence ratios. Additionally, at equivalence ratios above  $\phi \geq 0.67 \pm 0.02$ , a 4<sup>th</sup> broad and low amplitude peak is present below 250 Hz. With decreases in equivalence, the intensity of the highest frequency peak, centered at 386.4 Hz at  $\phi = 0.75 \pm 0.02$ , decreases monotonically shifting, at the same time, toward lower frequencies and has negligible intensity at  $\phi = 0.51 \pm 0.02$ . Of the other two peaks at 349.0 Hz and the broad and low intensity peak at 296.6 Hz; the one centered at 349.0 Hz at  $\phi = 0.75 \pm 0.02$  is present across all equivalence ratios to the lowest observed stable equivalence ratio,  $\phi$

$\phi=0.49\pm0.02$ . Upon reducing the equivalence ratio, the peak at 296.6 Hz becomes increasingly diffuse. Across the presented shifts in equivalence ratios, the amplitude of peaks in the given frequencies range decreases and the peak position shifts toward lower frequencies with reduction in equivalence ratios. For a heterogeneous combustion chamber operating at steady state using an  $\alpha\text{-Al}_2\text{O}_3$  media at steady state, characterization of such acoustic peaks produced by heterogeneous combustion may give insight on dramatic shifts in the temperature distributions within the combustion chamber, particularly at the lower equivalence ratios  $\phi =0.53\pm0.02$  through  $\phi =0.49\pm0.02$  which exhibit the most pronounced changes in performance.

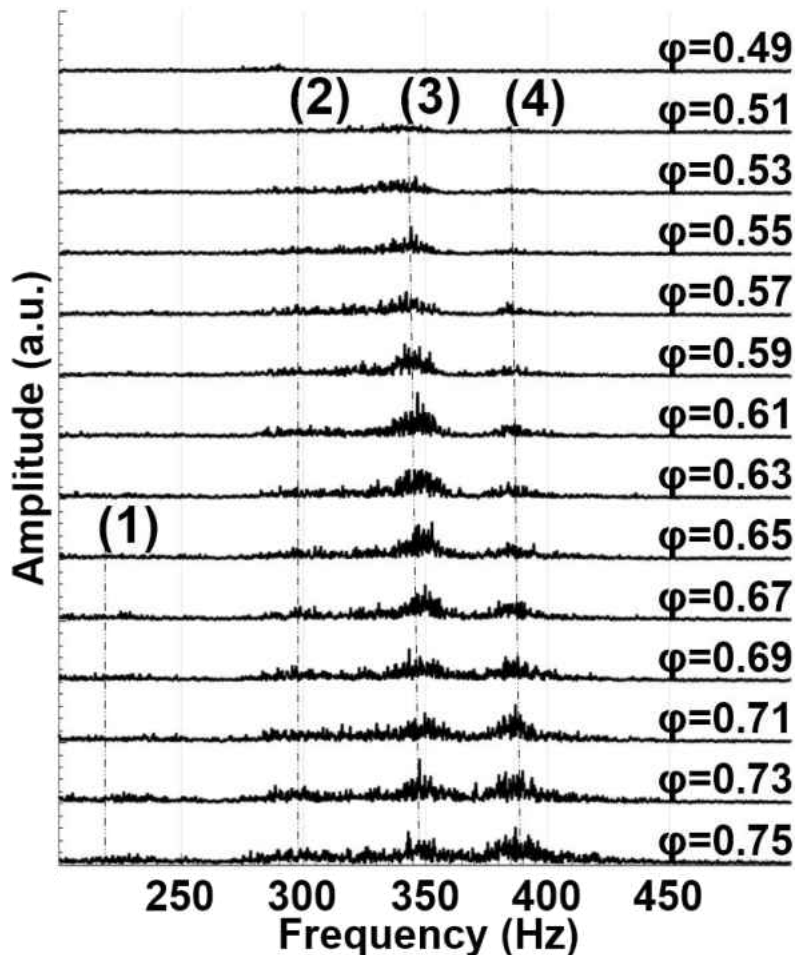


Figure 4-5: Acoustic profiles corresponding to the equivalence ratios presented.

However, when changing the equivalence ratio from  $\phi=0.59\pm 0.02$  to  $\phi=0.57\pm 0.02$  temperature distributions between the combustion chamber inlet and TC1 (44.1 mm) change, as the temperature profile across this span shifts toward lower temperatures it can be assumed that the ignition location of the flame tends closer to the exhaust. As one can see from Figure 4-4, a significant change in combustor performance occurs at equivalence ratios below  $\phi=0.53\pm 0.02$ , as lowering the equivalence ratio beyond  $\phi=0.53\pm 0.02$ , produces increasingly dramatic temperature reductions.

For all temperature measurements, the temperature reported at locations where porous ceramic media is placed, revealed that the variation of temperature across the span of the media is small compared to the maximum temperature within the combustion chamber, be it at  $\phi =0.75\pm 0.02$  or  $\phi =0.49\pm 0.02$ ; and thus, the temperature distribution of the media may be treated as isothermal which is in agreement with analytical models [39]. This isothermal temperature distribution is indicative of the presence of the flame through the entire length of the ceramic media. This is especially visible for the lowest equivalence ratios, where the temperature profile along the length coinciding with the porous media is flat indicating that the flame is diffuse through the entire length of the combustion media.

Photographs of the exhaust port of the combustion chamber taken at steady state operation corresponding to different equivalence ratios are shown in Figure 4-6. As one can see from Figure 4-6, at each equivalence ratio a distinct change in the radiative emissions is clearly visible, where a radiative emissions occur because of light emitted from within combustion chamber from both the porous media and gas phase. Across the probed range of equivalence ratios, a monotonic decrease in the intensity of the emission is recorded. At the higher equivalence ratios

$0.67 \pm 0.02 \leq \phi \leq 0.75 \pm 0.02$ , the entire area of porous media visible through the exhaust has the same color where none of the porous media structure is discernable. In some areas a decrease in the intensity of glowing light from the area immediately surrounding the walls of the exhaust opening can be also seen. At equivalence ratios below  $\phi = 0.65 \pm 0.02$  an increasing portion of the porous media's area becomes discernable, until the majority of the media's structure becomes visible at  $\phi = 0.51 \pm 0.02$ . At  $\phi = 0.49 \pm 0.02$  the flame is still active, however the radiative emissions are already below the detectable limits by the CCD camera.

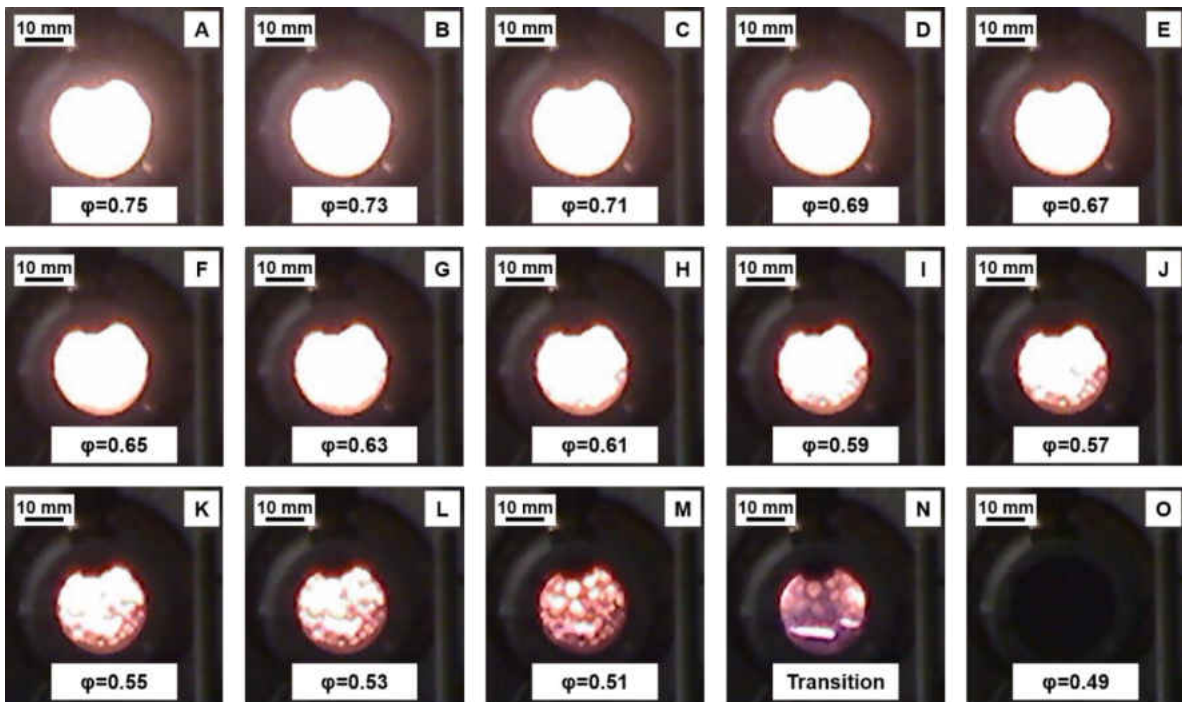


Figure 4-6: Images of the combustion chamber exit plane at given equivalence ratios.

### 4.3. Catalyst/Substrate Performance Characterization

#### 4.3.1. Thermal Performance Overview

Within this study several catalyst and substrate combinations were evaluated, average axial temperature profiles of the experiments are presented in Figure 4-7. As it was found MSZ provided the highest combustion chamber temperatures at lower equivalence ratio, MSZ was used as the

substrate for a catalyst application. Regardless of catalyst or media composition, at higher equivalence ratios the temperature profiles of all evaluated catalysts fall within a 100°C range of each other and thus, it can be assumed that the majority of the chemical reactions occurring within the combustion chamber do so within the gas phase.

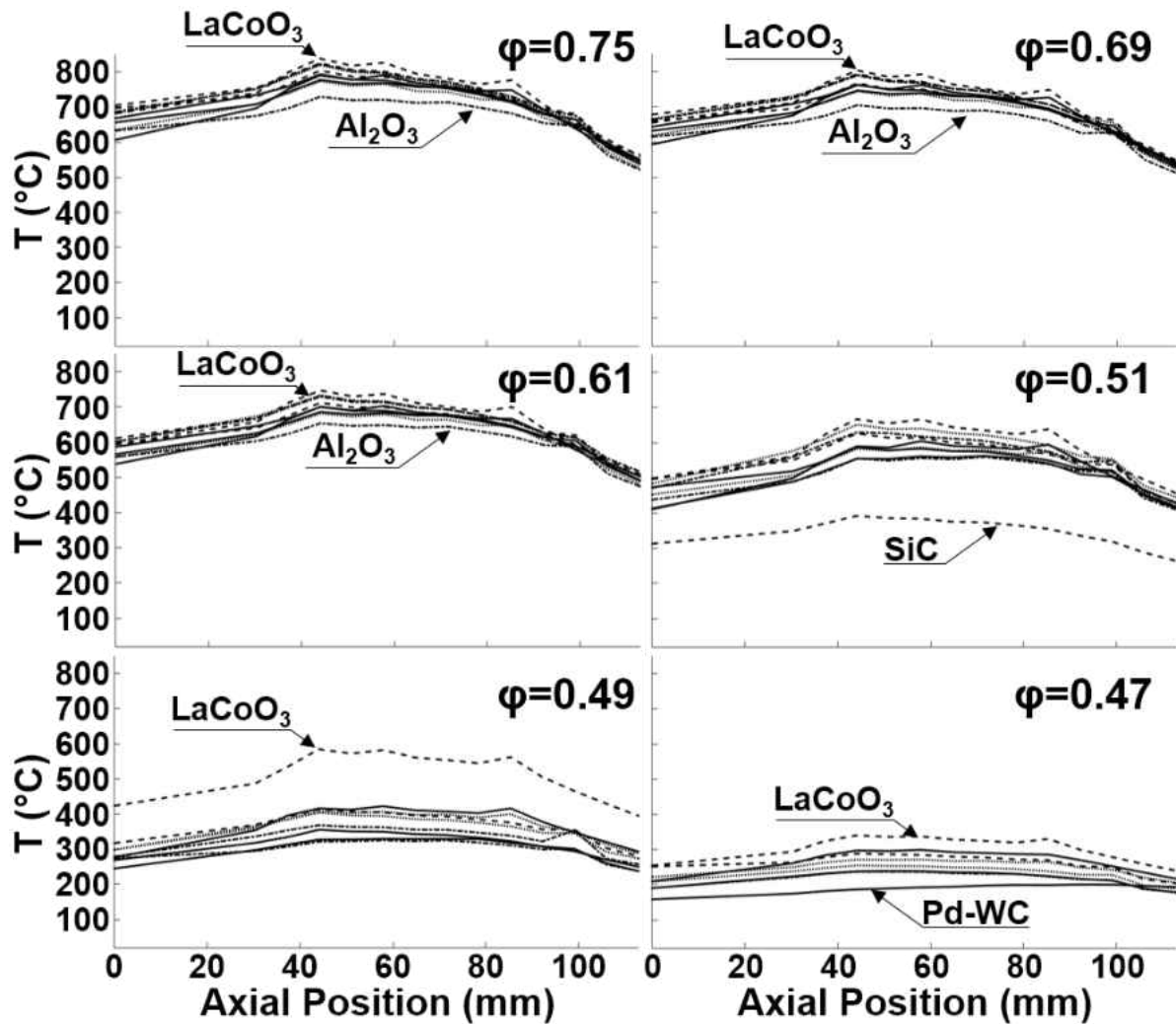


Figure 4-7: Axial temperature profiles of the catalyst and substrate combinations are presented for selected equivalence ratios.

It is not until equivalence ratios are lowered, near the lean limit that catalyst effectiveness can be truly evaluated as at these equivalence ratios temperatures are lower and the gas phase activation energy barrier is too large. Within Figure 4-8, temperature profiles of combustion under various

catalyst are presented. Of the selected catalysts,  $\text{LaCoO}_3$  enabled the highest temperatures at the low equivalence ratio of  $\phi=0.47\pm 0.02$ .  $\text{Ce}_{0.8}\text{Gd}_{0.2}\text{O}_{1.9}$  provided the second highest temperature at a significantly lower catalyst mass loading fraction. Strangely enough, the application of some catalysts actually lowered the maximum temperatures within the combustion chamber compared to the uncoated media. The catalysts which performed worse than the uncoated media at  $\phi=0.47\pm 0.02$  were  $\text{La}_{0.75}\text{Sr}_{0.25}\text{Fe}_{0.95}\text{Ru}_{0.05}\text{O}_3$ ,  $\text{ZrB}_2$ ,  $\text{La}_{0.80}\text{Ca}_{0.20}\text{CoO}_3$ , and Pd enhanced WC.

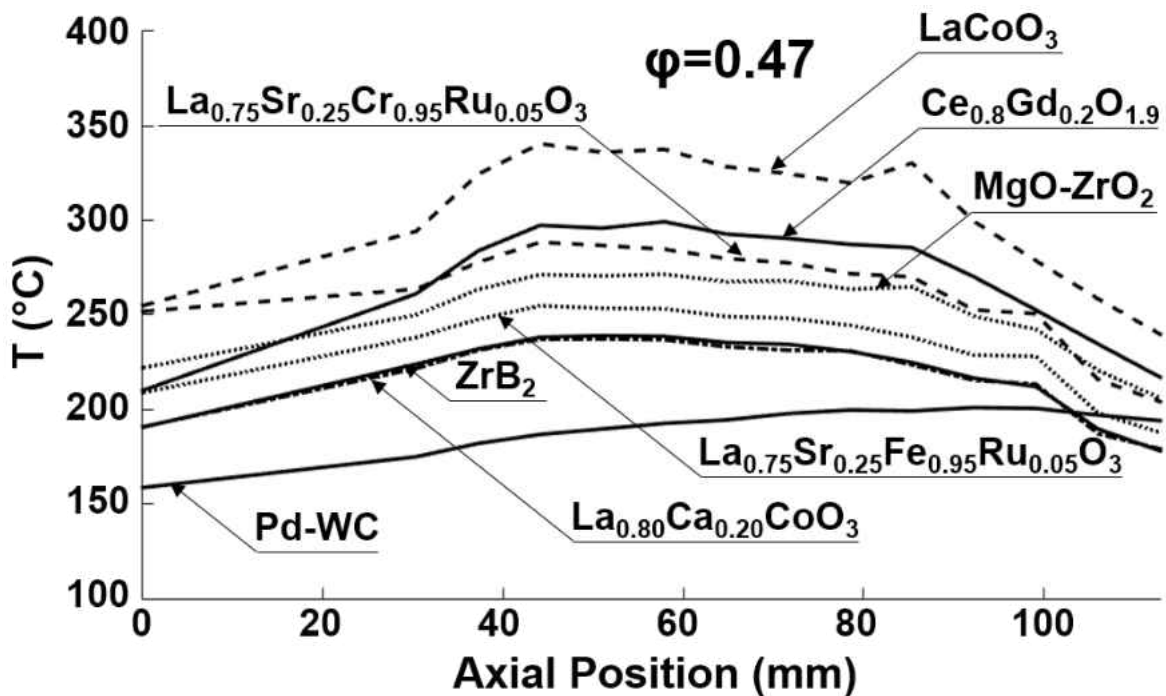


Figure 4-8: Axial temperature profiles at  $\phi=0.47\pm 0.02$  for the MSZ media and catalysts coated onto the MSZ substrate.

#### 4.3.2. Substrate Performance Overview

Three substrates were evaluated for performance in the heterogeneous combustion chamber  $\alpha\text{-Al}_2\text{O}_3$ , MSZ, and SiC media and the steady state temperature profiles at various equivalence ratios for a fixed are flow rate are presented in Figure 4-9. All of the media follow a similar trend, of a linear decrease in maximum temperature followed by a sudden drop at low equivalence ratio, though when such decrease in maximum temperature is substrate dependent. Of the three media

types, from  $\phi=0.75\pm0.02$  to  $\phi=0.55\pm0.02$  SiC maintained the highest temperature profile across the combustion chamber. However, at  $\phi=0.53\pm0.02$ , some change occurs in the flame structure and the temperature of the flame supported by the SiC media decreases suddenly, such changes are not observed in MSZ and  $\text{Al}_2\text{O}_3$  until  $\phi=0.49\pm0.02$ . maximum temperatures within the combustion chamber and the temperature at the last axial combustion chamber thermocouple can be seen in Table 4-2 and Table 4-3, respectively.

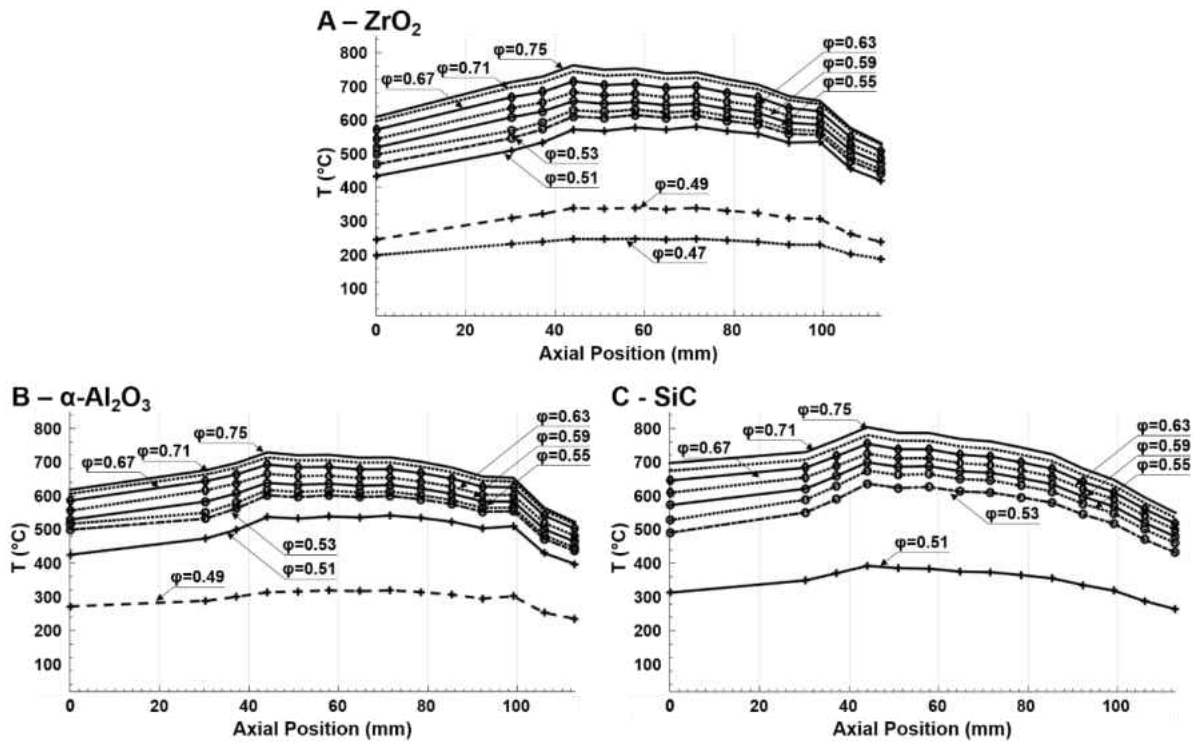


Figure 4-9: Axial temperature profiles of the selected substrates at various equivalence ratios.

$\phi\pm0.02$	0.75	0.71	0.67	0.63	0.59	0.55	0.53	0.51	0.49	0.47
SiC	804.1	780.4	754.6	725.3	699.6	674.8	636.3	392.3	-	-
$\text{Al}_2\text{O}_3$	728.8	713.7	692.7	665.0	638.4	601.6	601.6	541.6	319.3	-
MSZ	762.6	744.2	715.0	683.0	656.4	631.6	615.3	580.4	339.6	247.0

<b>Table 4-3: Maximum temperatures, <math>T_{\text{exh}} \pm 4.7^\circ\text{C}</math>, observed within the combustion chamber with selected substrates at various equivalence ratios.</b>										
$\phi \pm 0.02$	0.75	0.71	0.67	0.63	0.59	0.55	0.53	0.51	0.49	0.47
SiC	550.0	535.0	518.0	499.9	479.2	460.5	432.3	260.0	-	-
Al <sub>2</sub> O <sub>3</sub>	552.1	516.3	502.4	481.6	463.9	446.2	436.4	397.6	234.9	-
MSZ	531.5	527.4	507.8	488.9	471.1	452.7	441.2	420.4	238.3	188.4

At each steady state of flow rate and equivalence ratio, the acoustic signal was collected from the instrumentation setup as described in chapter 3, such acoustic signals for each substrate are presented in Figure 4-10. Regardless of the composition of the media, there is a similar structure to the frequency distribution of the acoustic peaks over the spectral range of 200 to 500 Hz, exhibiting a 4 peak acoustic signature and as the equivalence ratio is reduced there is a shift toward lower frequency. Additionally, as the equivalence ratios are reduced, peaks (2) and (3) coalesce into a single continuous peak (2') the equivalence ratio of when this happens is dependent upon the composition of the porous media. However, while the existence of noise over this spectral range there are profound differences which may also be observed.

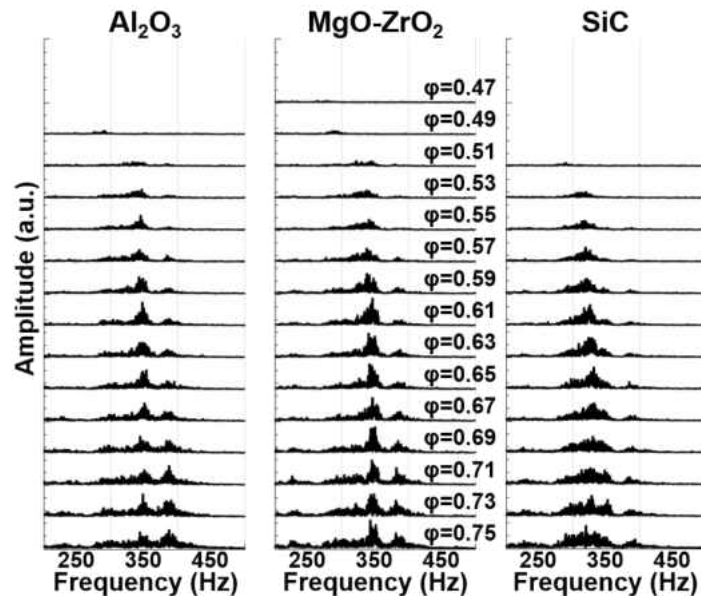


Figure 4-10: Acoustic profiles over the range of steady states pertaining to the selected substrates.



Examining the equivalence ratio of the three substrates at the equivalence ratio  $\phi=0.75\pm 0.02$  presented in Figure 4-11 such differences between the acoustic spectra for the substrates may be observed. The most prominent difference between the acoustic spectra can be observed in the SiC substrate as there is one continuous peak (2') as opposed to peak (2) and (3) which are exhibited by the  $\text{Al}_2\text{O}_3$  and MSZ media. Other differences which may be observed are the relative intensities of peak (3), or in the case of SiC (2'), to the other peaks (1), (2), and (4). In the acoustic spectra corresponding to MSZ, peak (3) exhibits nearly 2x the intensity of (4) and significantly more than either (1) or (2). Conversely in the spectra pertaining to the  $\text{Al}_2\text{O}_3$  media, peak (4) actually exhibits a higher intensity than any of the other peaks.

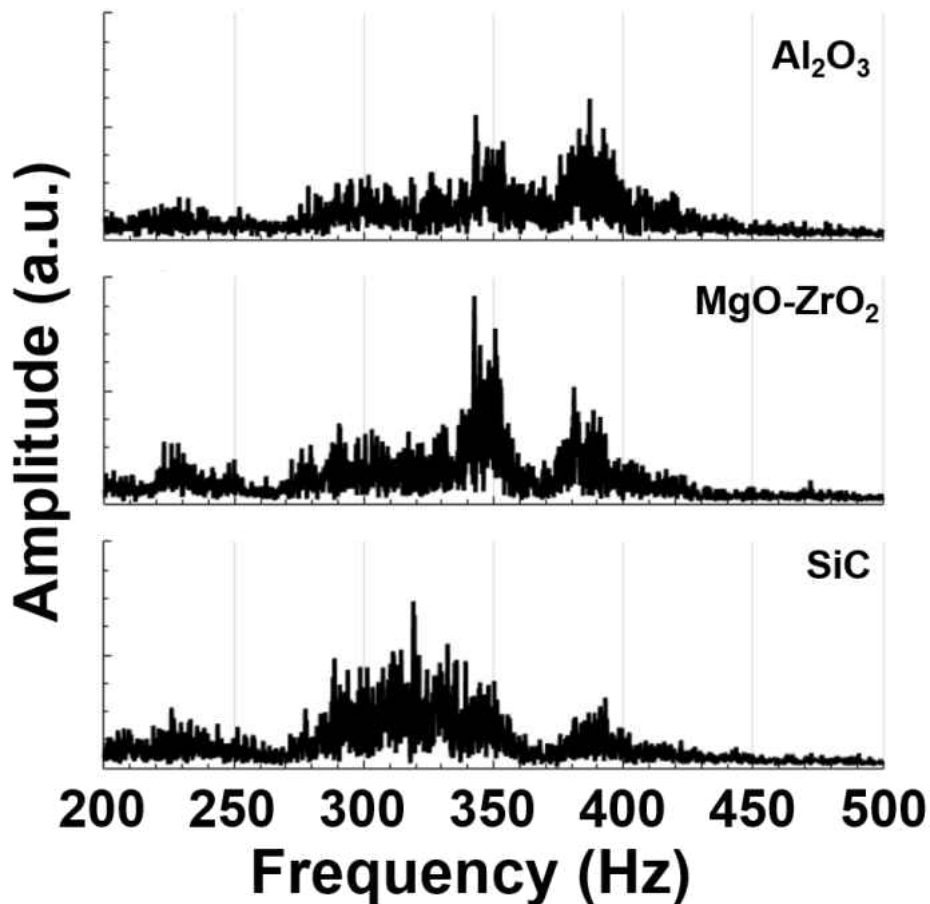


Figure 4-11: Equivalence ratio pertaining to operation of the combustion chamber with various substrates at the equivalence ratio of  $\phi=0.75\pm 0.02$

Acoustic spectra of the operation of the combustion chamber at  $\phi=0.53\pm0.02$  is presented in Figure 4-12. At this equivalence ratio, all of the acoustic spectra regardless of media composition exhibit peaks significantly lower than at  $\phi=0.75\pm0.02$ . Additionally, peaks (1) in each of the spectra have entirely decayed, similarly peak (4) have decayed entirely for SiC and MSZ.

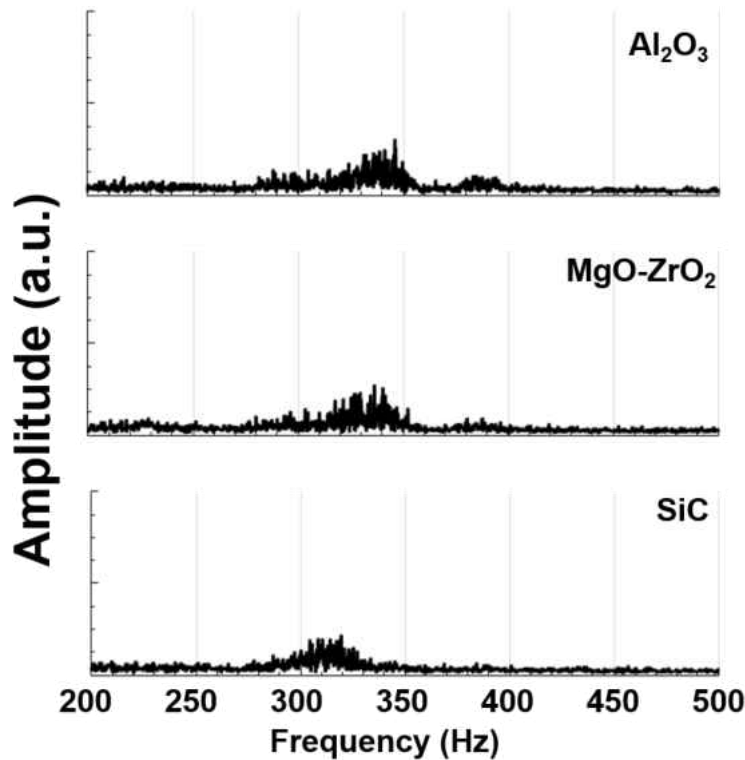


Figure 4-12: Equivalence ratio pertaining to operation of the combustion chamber with various substrates at the equivalence ratio of  $\phi=0.53\pm0.02$

Radiative emissions within the visible spectrum from the evaluated substrates are presented in Figure 4-13 at various steady states corresponding to the equivalence ratios  $\phi=0.75\pm0.02$ ,  $\phi=0.53\pm0.02$ , and  $\phi=0.51\pm0.02$ . Immediately it could be observed that the emissions from the substrates are different colors, where the  $\text{Al}_2\text{O}_3$  media is yellow, the MSZ media is pink, and the SiC media is violet at  $\phi=0.75\pm0.02$  such color change is a result of the spectral emissivity of the substrate, distribution of the flame within the combustion chamber and the temperature of the solid phase. It could also be observed that regardless of media composition the intensity of the light

emitted from the combustor exhaust decreases as does the position of the flame within the combustion chamber. At  $\phi=0.53\pm 0.02$ , the media is visible for both the SiC media and the  $\text{Al}_2\text{O}_3$  media, such media being visible indicates that the flame is contained within the porous media entirely and is actually submerged. However at this equivalence ratio the MSZ media is still only white. Further reduction of equivalence ratio to At  $\phi=0.51\pm 0.02$  causes the radiative emission from the SiC media to be undetectable by the detector. Similarly the intensity of the radiative emissions from flames supported by the MSZ and  $\text{Al}_2\text{O}_3$  media decrease.

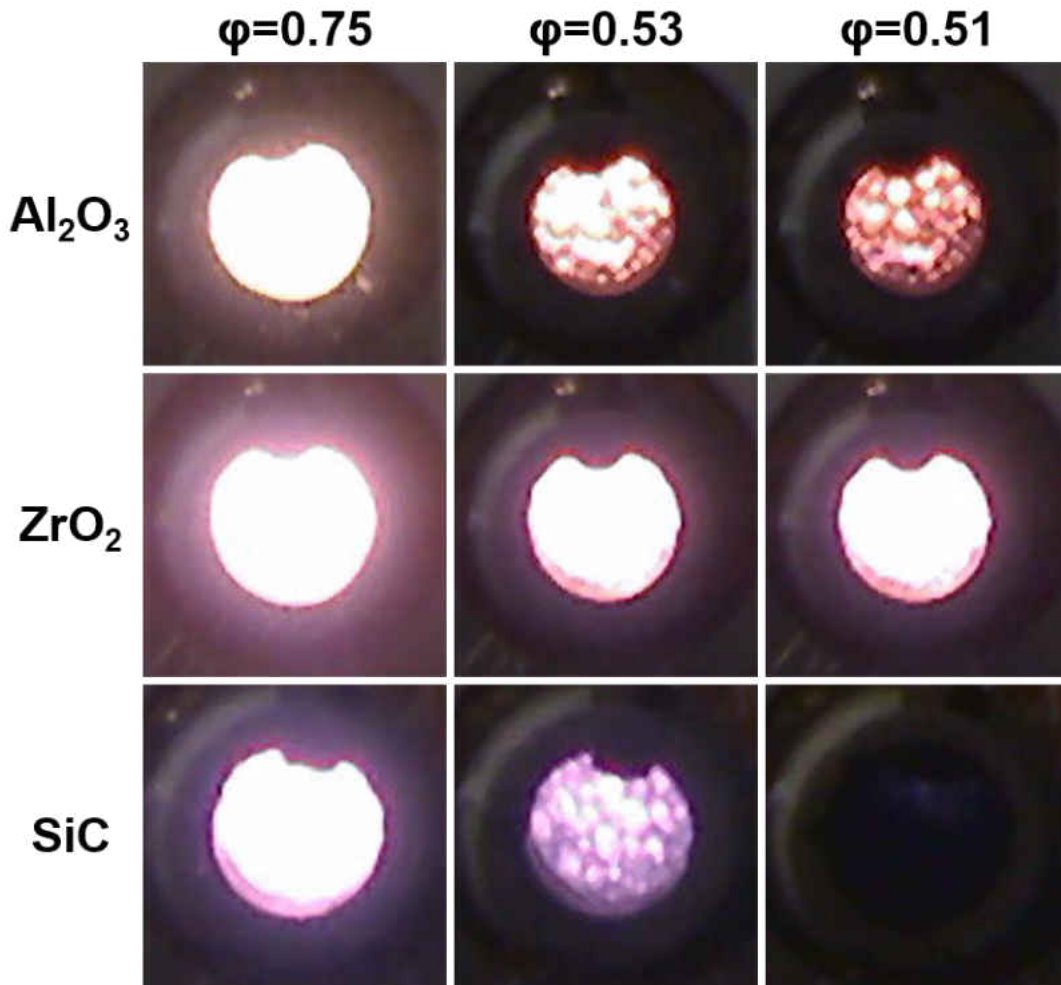


Figure 4-13: Photographs of radiative emissions of the porous media through the combustion chamber exhaust.

### 4.3.3. $Ce_{0.8}Gd_{0.2}O_{1.9}$ Catalyst Performance

Performance of the GDC coated MSZ media was surprisingly high given its low loading fraction. During warmup the maximum heating rate of the GDC was found to be  $34.9 \pm 6.2^\circ\text{C}/\text{min}$  at  $\phi = 0.80 \pm 0.02$   $\dot{V} = 51.59 \pm 0.61$  SLPM, versus a rate of  $24.0 \pm 6.2^\circ\text{C}/\text{min}$  for the uncoated MSZ. Steady state axial temperature profiles at various equivalence ratios are presented in Figure 4-14. When GDC is present, temperatures are significantly higher across the range of probed equivalence ratios. In addition to the heightened temperatures, there are secondary temperature increases within the combustion chamber following the maximum temperature observed at 44.1mm (TC1) at 57.9mm and 85.4mm (TC3), across the range of equivalence ratios  $\phi = 0.75 \pm 0.02$  to  $\phi = 0.59 \pm 0.02$ , which indicate a staged combustion process through the porous media. As the equivalence ratio is lowered to  $\phi = 0.51 \pm 0.02$ , the temperature increase at 44.1 mm becomes less pronounced, however at 57.9mm, and 85.4mm (TC3) the temperatures are still significantly higher than other parts of the porous media. Subsequent equivalence ratio reductions to  $\phi = 0.49 \pm 0.02$  reduce the magnitude of the two temperature increases and by  $\phi = 0.47 \pm 0.02$  the porous media is nearly isothermal. The lowest possible equivalence ratio achieved when GDC enhancement was present was equal to  $\phi = 0.45 \pm 0.02$ , which was not possible to achieve for MSZ without enhancement experiment. From the performed experiments one can conclude that the inclusion of GDC causes a significantly more complex flame structure.

Operating at  $\phi = 0.45 \pm 0.02$  with GDC catalyst present on the MSZ porous media, both  $\frac{\partial T}{\partial x_{\phi, \dot{V}}}$  and  $\frac{\partial^2 T}{\partial x^2_{\phi, \dot{V}}}$  become positive over the axis of the combustion chamber; indicating the combustor is operating in a different mode from all other observed behavior. In this second observed mode, low

temperature chemical reactions, which are assumed to occur primarily on the catalyst surface, enabling some small quantity of heat to be released. The released heat causes an increase in the axial temperature profile ( $\frac{\partial T}{\partial x_{\phi, V}}$ ) from the inlet to outlet of the combustion chamber, while also increasing the concentration of combustion intermediates facilitating further reactions, which causes an increase in the axial heat release rate over the combustion chamber length ( $\frac{\partial^2 T}{\partial x^2_{\phi, V}}$ ). It is not until gasses are discharged from the porous media that there is a sufficient quantity of free radicals and combustion intermediates with sufficient energy to undergo spontaneous chemical reactions and form a flame. Such flame location outside of the porous media is supported by the data obtained by the optical characterization.

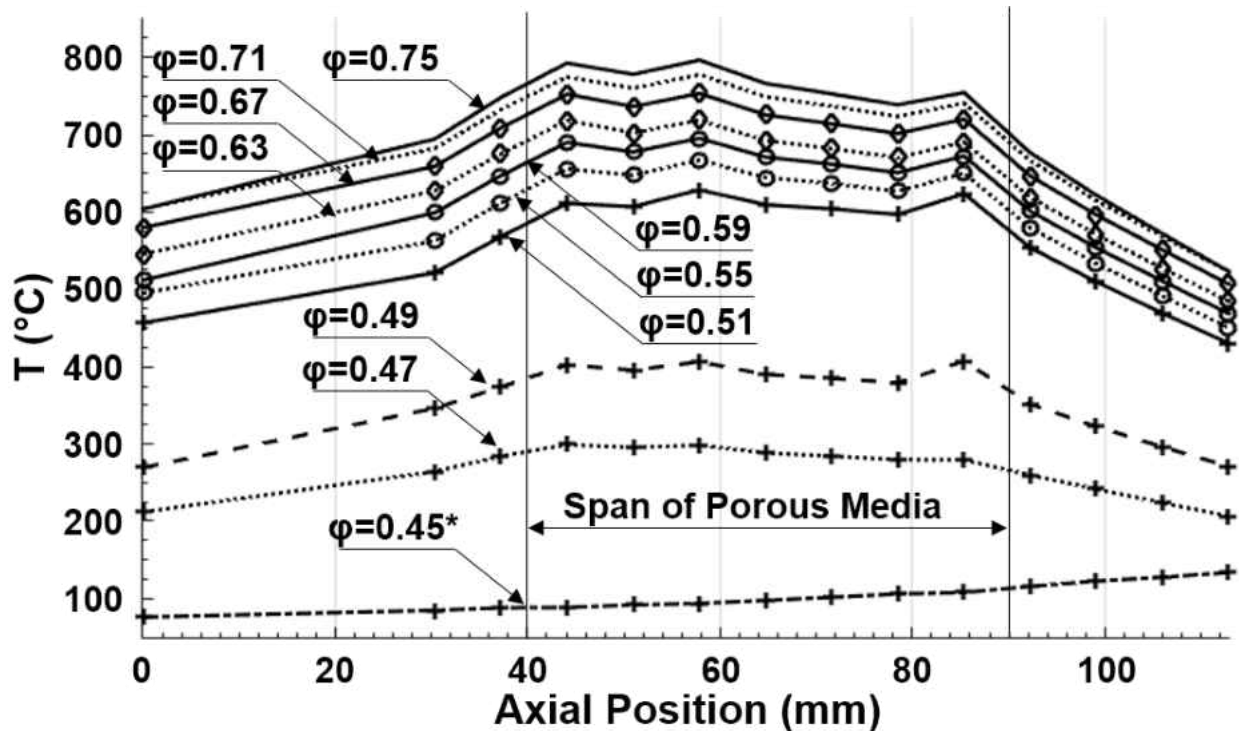


Figure 4-14: Photographs of radiative emissions of the porous media through the combustion chamber exhaust.

Asdasdasd

As with the uncoated  $\text{Al}_2\text{O}_3$  media, similar patterns can be seen with photographic imaging of the GDC coated MSZ media within the combustion chamber, as the equivalence ratio is reduced from  $\phi=0.75\pm 0.02$  the intensity of the emitted light is reduced. However, unlike the  $\text{Al}_2\text{O}_3$  media at  $\phi=0.49\pm 0.02$  the combustion chamber is still hot enough to enable visible radiative emissions. Upon subsequent reduction of equivalence ratio to  $\phi=0.47\pm 0.02$  however, the temperature of the porous media within the combustion chamber is too low to enable sufficient radiative emissions within the visible spectrum. At  $\phi=0.45\pm 0.02$  the flame, as the blue luminous region can be directly observed indicating that at this equivalence ratio and under this catalyst, the combustor is operating while the flame is not submerged.

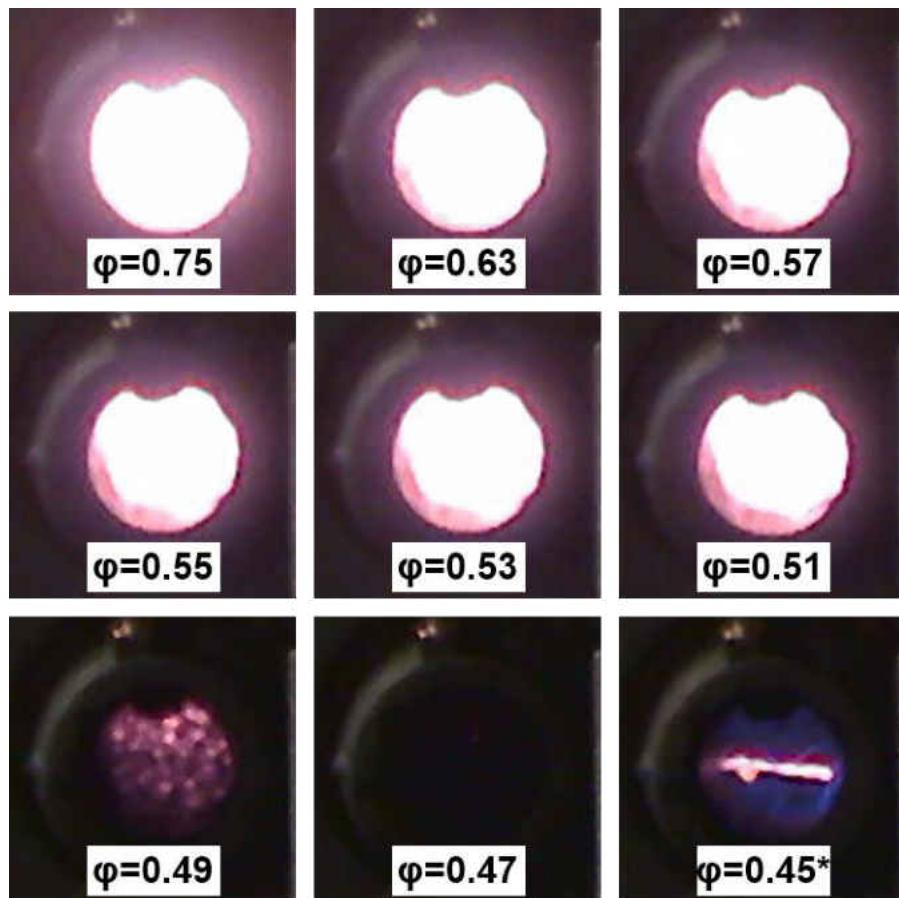


Figure 4-15: Photographs of radiative emissions of the porous media through the combustion chamber exhaust.

#### 4.3.4. *LaCoO<sub>3</sub> Catalyst Performance*

Within Figure 4-16, the axial temperature profiles of the combustion chamber are presented. At the equivalence ratio  $\phi=0.75\pm 0.02$  temperatures recorded between TC0 (0.0 mm) and the thermocouple at 30.3 mm are nearly isothermal, followed by a linear temperature increase until TC1 (44.1 mm). Such isothermal behavior across the first 30.3 mm of the combustion chamber is indicative of a particularly strong azimuthal swirl effect and recirculation within the entry region [180]. Formation and stabilization of such a region can be driven by heat release rates exciting characteristic recirculation within the combustion chamber [178].

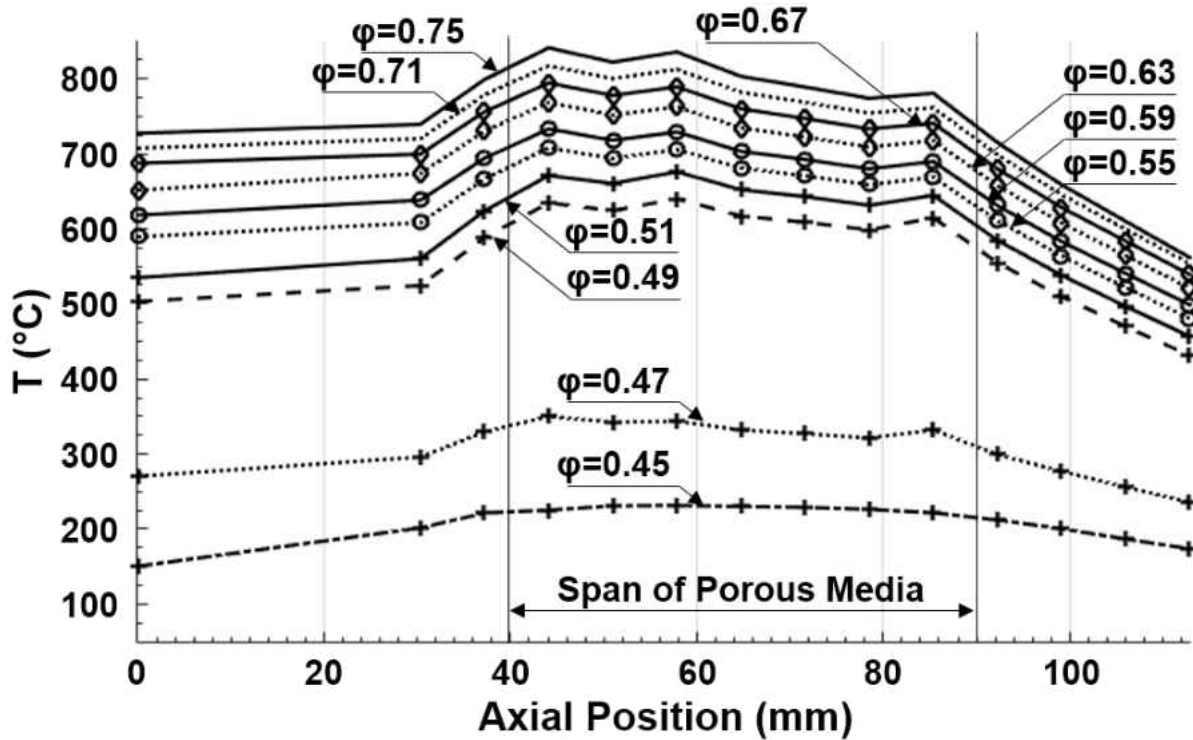


Figure 4-16: Axial temperature profile of the combustion chamber containing MSZ media coated with  $\text{LaCoO}_3$ .

Within the span of the porous media at the equivalence ratio of  $\phi=0.75\pm 0.02$ , temperatures recorded at 44.1mm (TC1) are the highest and temperatures decrease through the combustion chamber moving toward to the exhaust. However, there are secondary temperature increases across

the span of porous media at 57.9mm and 85.4mm (TC3), across the range of equivalence ratios  $\phi=0.75\pm0.02$  to  $\phi=0.49\pm0.02$ , which indicate a staged combustion process through the porous media; such staged combustion process was also observed, and even more pronounced, when only the GDC coating was present on the surface of the MSZ media [181]. It is possible that the relatively large temperature decrease between 57.9mm and 85.4mm (TC3) while the combustion chamber is operating at  $\phi=0.75\pm0.02$  is due to the rapid transformation of reactant gasses to equilibrium concentrations of combustion byproducts by 57.9mm, disallowing the release of heat until the temperature is low enough at 78.5mm to enable a shift in the equilibrium concentration of CO and other quasi stable combustion intermediates to CO<sub>2</sub>, with sufficiently high reaction rates which enables the release of additional heat over a finite span. Following the porous media, the temperature of exhaust gasses rapidly decay, at a near constant rate  $\frac{\partial T}{\partial x_{\phi, \dot{V}}} \approx 7.3\pm 6.8$  °C/mm, over the span of 85.4 mm to 112.9 mm indicating heat release rates over this segment of the combustion chamber are significantly lower than rates of heat loss.

As equivalence ratios within the combustion chamber decrease, there is a quasi-linear decrease in maximum temperatures, average temperatures, and temperature at 112.9 mm between  $\phi=0.75\pm0.02$  until  $\phi=0.49\pm0.02$ . Over this range of equivalence ratio shifts, the temperature difference between 44.1mm (TC1) and 57.9mm becomes less pronounced where at  $\phi=0.75\pm0.02$   $\Delta T_{57.9-44.1}=5.4\pm 9.1$  °C and at  $\phi=0.49\pm0.02$   $\Delta T_{57.9-44.1}=-5.5\pm 7.1$  °C. Such behavior is to be expected as the decrease in local temperatures over this range significantly reduce the maximum permissible rate of combustion byproduct formation.

Following the equivalence ratio reduction to  $\phi=0.47\pm0.02$  there is a dramatic decrease in average combustion chamber temperatures, approximately  $257.8\pm 6.3$  °C. It is expected that at this



dramatically reduced temperature range, the effect of surface facilitated chemical reactions becomes the primary pathway by which reactants are recombined into products. With this shift in temperature, the magnitude of the temperature variations over this range also significantly decrease. A subsequent reduction in equivalence ratio to  $\phi=0.45\pm0.02$  produces a nearly uniform temperature profile over the span of the combustion chamber and the temperature increases which were previously observed at 44.1 (TC1), 57.9mm and 85.4mm (TC3) become non-existent and instead the maximum temperature observed within the combustion chamber is located at 57.9 (TC2). Additionally, by examination of the temperature difference between 0.0mm (TC0) and 30.33 mm at  $\phi=0.45\pm0.02$ , it may be assumed that there is a significant shift in the structure of the recirculation within the combustion chamber.

Within Figure 4-17, both photographs of the porous media visible through the exhaust at steady state corresponding to selected equivalence ratios (Figure 4-17 A through H) and acoustic spectra of exhaust emissions at all of the observed equivalence ratio steady states (Figure 4-17K) are presented. Across equivalence ratios  $\phi=0.75\pm0.02$  to  $\phi=0.69\pm0.02$ , there is nearly no distinguishable difference in the radiative emissions in the visible spectrum observed through the exhaust with the exception of reduced glow surrounding the walls of the exhaust. At  $\phi=0.63\pm0.02$  a small region of pink becomes visible, which is indicative of cooling. A larger pink region is made visible at the equivalence ratio  $\phi=0.57\pm0.02$  and the color coinciding with this feature shifts from pink to a more purplish hue. At the equivalence ratio  $\phi=0.53\pm0.02$  there is a near symmetric region around the outer visible span of the porous media which reveals some features. As equivalence ratio is reduced to  $\phi=0.49\pm0.02$ , the majority of the exhaust pane of the porous media is visible and from the photo it can be determined that there is a near uniform intensity of the flame about

the azimuthal direction though simultaneously, as there is a small region which reveals no distinguishable features, it can be confirmed that there is a strong radial dependence of the flame. The subsequent equivalence reduction to  $\varphi=0.47\pm 0.02$  reveals only an extremely faint blue region and by  $\varphi=0.45\pm 0.02$  the temperature of the porous solid at the exit is below a temperature which enables sufficient emission of radiative thermal energy in the visible spectrum.

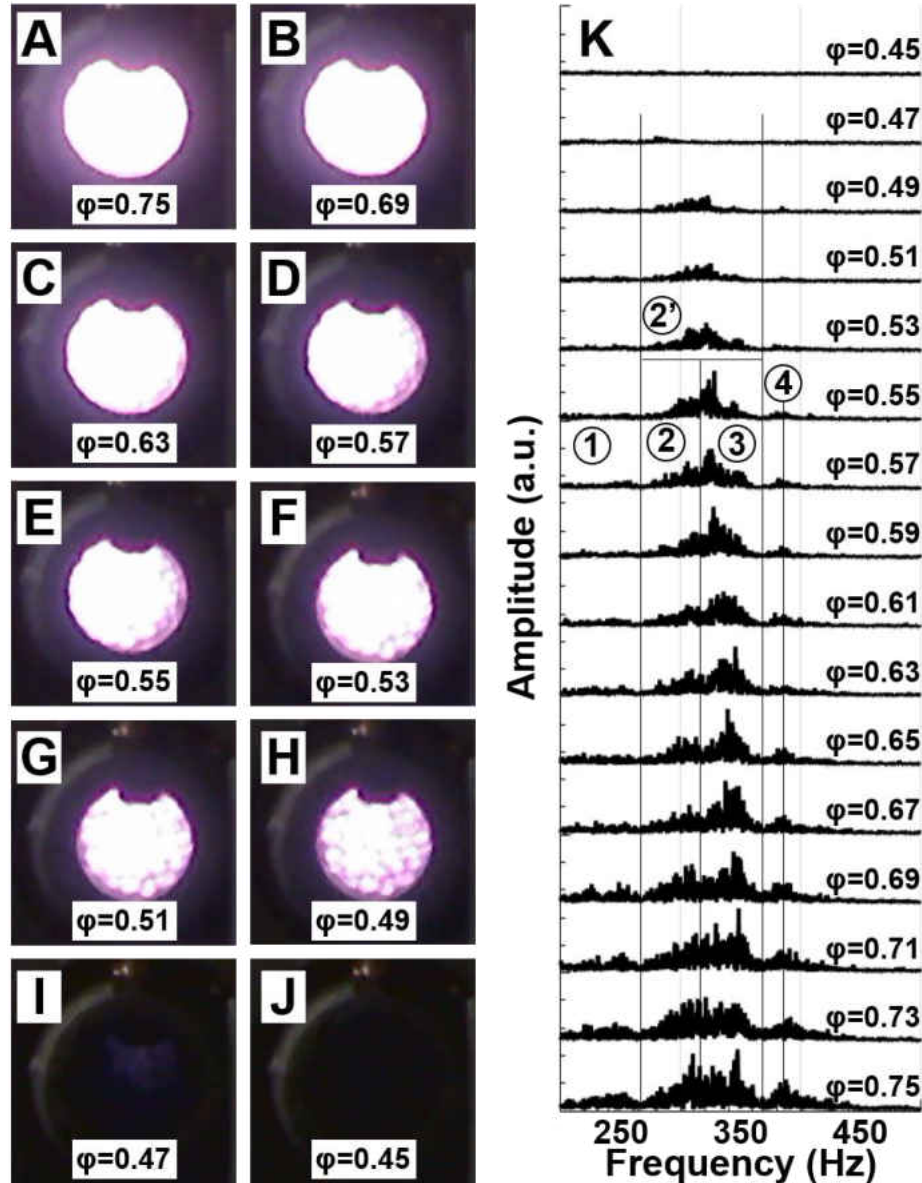


Figure 4-17: Acoustic and optical characterization of the exhaust emissions while  $\text{LaCoO}_3$  coated MSZ media was immersed in the combustion chamber.

Within Figure 4-17, acoustic profiles at all of the steady state equivalence ratios between  $\phi=0.75\pm0.02$  and  $\phi=0.45\pm0.02$  are presented. These acoustic spectra are subdivided into 4 other peaks as was done in previous works considering this combustion chamber [180-184]: peak (1) coincides with frequencies between 200 Hz and 270Hz, peak (2) coincides with the peak between 270Hz and 330Hz, peak (3) which is the highest amplitude peak at  $\phi=0.57\pm0.02$  may be observed between 330 Hz and 370 Hz, peak (4) is present at frequencies above X and below X. Within these spectra, the majority of the observed signal is present across peaks (2) and (3) with peak (1) and (4) having lesser amplitudes. As with the other evaluated media, peaks (1) and (4) both decrease in amplitude significantly faster than peaks (2) and (3) [180-184]. Furthermore, at equivalence ratios below  $\phi=0.55\pm0.02$ , peaks (2) and (3) become indistinguishable and the conjoined peak is referred to as peak (2').

#### ***4.3.5. Pd-WC Catalyst Performance***

As one can see from Figure 4-18, axial temperature distributions within the combustion chamber are the highest within the span of the porous media across all of the observed steady states at each equivalence ratio and flow rate combination. For all  $0.53\pm0.02\leq\phi\leq0.75\pm0.02$  the highest temperature within the combustion chamber was measured at 44.1 mm (TC1) at the location near the entry but still inside of the porous MSZ media. Temperatures recorded within the combustion chamber between 85.4 and 112.9 mm (TC3 and TC4), after the porous media, exhibit a rapid drop in temperature indicating that the rate of heat release within this part of the combustion chamber is significantly lower than the rate of heat loss through the wall of the combustion chamber to the environment (Figure 4-18). It is also possible to see that as the equivalence ratio within the combustion chamber is lowered, the temperature profile measured within porous ceramic media

becomes increasingly homogeneous. The maximum temperature location at 44.1mm becomes increasingly less pronounced as equivalence ratio is decreased from  $\phi=0.75\pm0.02$  to  $\phi=0.53\pm0.02$ , and at  $\phi=0.51\pm0.02$  and below the temperature profile across the porous media is almost isothermal, indicating that the heat release rate from combustion is almost constant through the porous media.

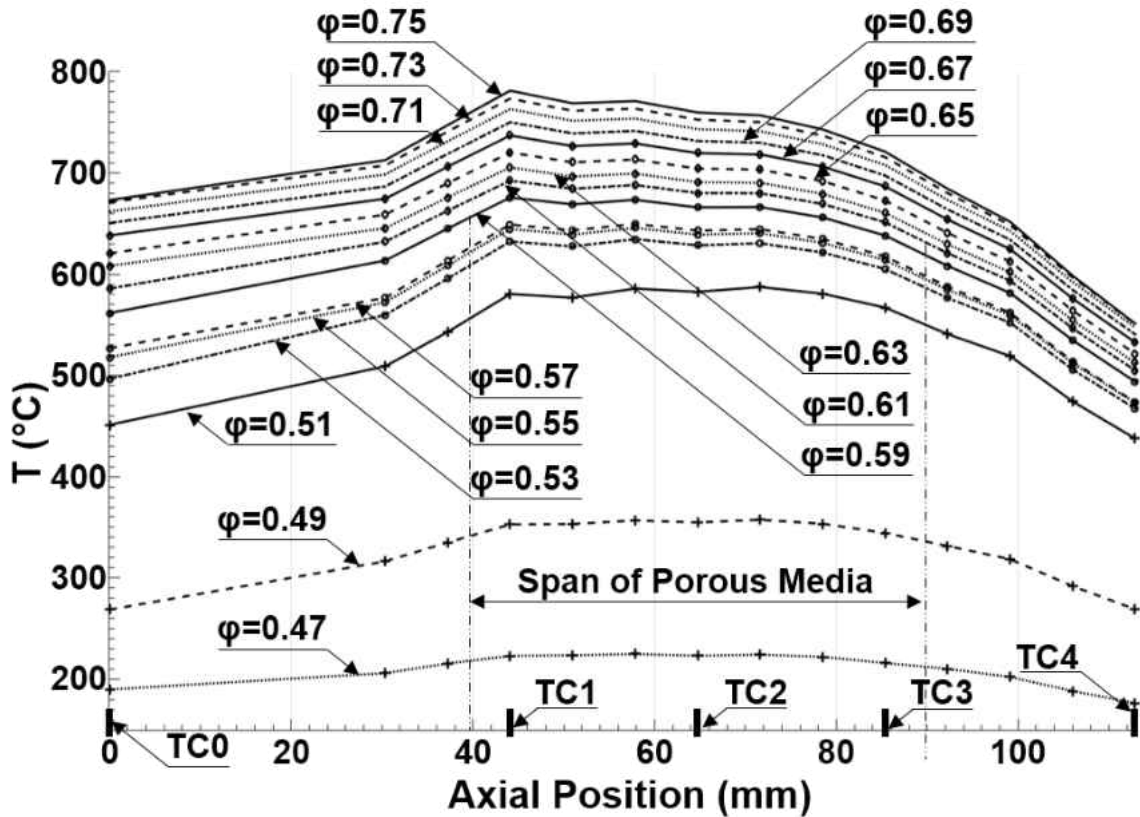


Figure 4-18: Acoustic and optical characterization of the exhaust emissions while  $\text{LaCoO}_3$  coated MSZ media was immersed in the combustion chamber.

Images of the exhaust pane at a steady state operation corresponding to selected equivalence ratios at a fixed air flow rate are shown in Figure 4-19. At equivalence ratios above  $\phi=0.53\pm0.02$  the porous media is hot enough to emit a sufficient quantity of electromagnetic radiation in the visible spectrum which can be seen as the white region within the center of each pane of the image. As one can see from Figure 4-19 the intensity and color of the porous media visible through the

exhaust varies minimally across equivalence ratios of  $\phi=0.75\pm0.02$  to  $\phi=0.53\pm0.02$ . However, across the range of equivalence ratios, the slight reduction in the glow surrounding the exhaust port occurs as the equivalence is reduced and the semicircular areas of porous media becomes discernable at the outer radius of the combustion chamber (Figure 4-19). Such changes in the visible radiative emission with decrease in equivalence ratio is a combination of at least two different competing processes and can be explained (i) by the decrease in the temperature of the flame, at  $\phi=0.75\pm0.02$  the intensity of combustion causes the porous media to be extremely hot but as the equivalence ratio decreases, the heat release rate is lowered allowing the porous media to cool, and at the same time, a competing process causing the media to glow brighter occurs; (ii) as equivalence is reduced the boundary of the flame moves closer to the exhaust, causing light emitted from the gas phase to become more visible via the included instrumentation.

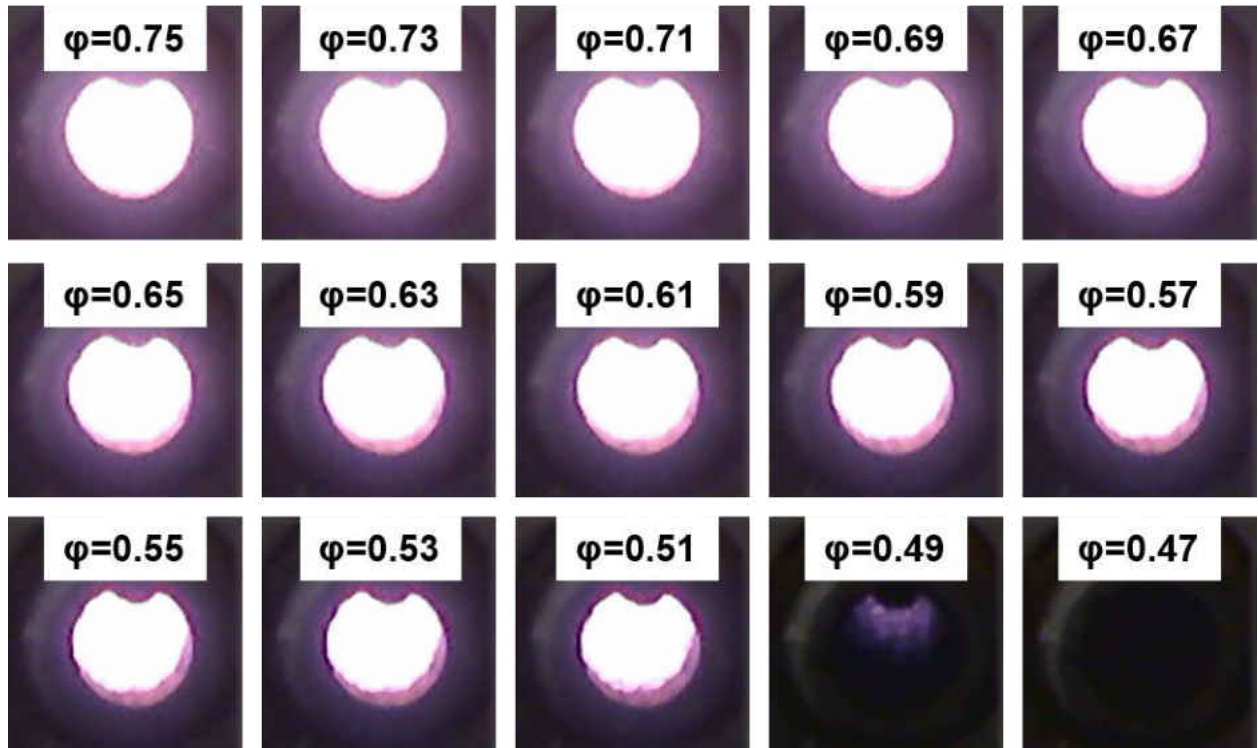


Figure 4-19: Optical images of the combustor exhaust with Pd Enhanced WC catalyst.

Once the equivalence is reduced to  $\varphi=0.53\pm 0.02$ , changes in the emitted thermal radiation at the exhaust become significantly more pronounced. At equivalence ratio  $\varphi=0.51\pm 0.02$ , the color of light emitted by the porous media becomes pink. Upon the following reduction of equivalence ratio  $\varphi=0.51\pm 0.02$  to  $\varphi=0.49\pm 0.02$ , the intensity of light observed across the exit pane of the combustion chamber is significantly reduced with only purplish regions observed at small portion of the exhaust image. A subsequent reduction in equivalence to  $\varphi=0.47\pm 0.02$  reduces the emissive intensity across the visible spectrum below the detectable limits of the CCD camera.

Acoustic profiles from the combustion chamber measured at different equivalence ratios at several state operation across the special range between 200 and 500 Hz are presented in Figure 4-20. At the highest equivalence ratio of  $\varphi=0.75\pm 0.02$ , four acoustic peaks: (1) a low frequency and very broad peak with a low intensity centered at 229.8 Hz; (2) a broad and higher intensity peak 270 -> 340 Hz; (3) a well defined and highest intensity peak centered at 349.0 Hz; and (4) an asymmetric peak with a peak amplitude centered at 387.1 Hz. As the equivalence ratio is reduced from  $\varphi=0.75\pm 0.02$  to  $\varphi=0.61\pm 0.02$  significant changes in the structure of the acoustic noise emitted from the combustion chamber are detected (Figure 4-20). While peak (2) intensities of exhaust emission are approximately constant at  $0.61\pm 0.02 \leq \varphi \leq 0.75\pm 0.02$ , a disappearance of (1) peaks occurs and the amplitude of (4) peak rapidly decays when equivalence is decreased further beyond 0.61. At  $\varphi=0.59\pm 0.02$  instead of two 272.5-339.1 Hz and 349.0 Hz peaks, only one very broad peak (2') ranging between 273.2 Hz and 360.9 Hz can be observed. As equivalence is further decreased to below  $\varphi=0.53\pm 0.02$ , the intensity of this very broad peak rapidly decays and its position shifts toward lower frequencies.

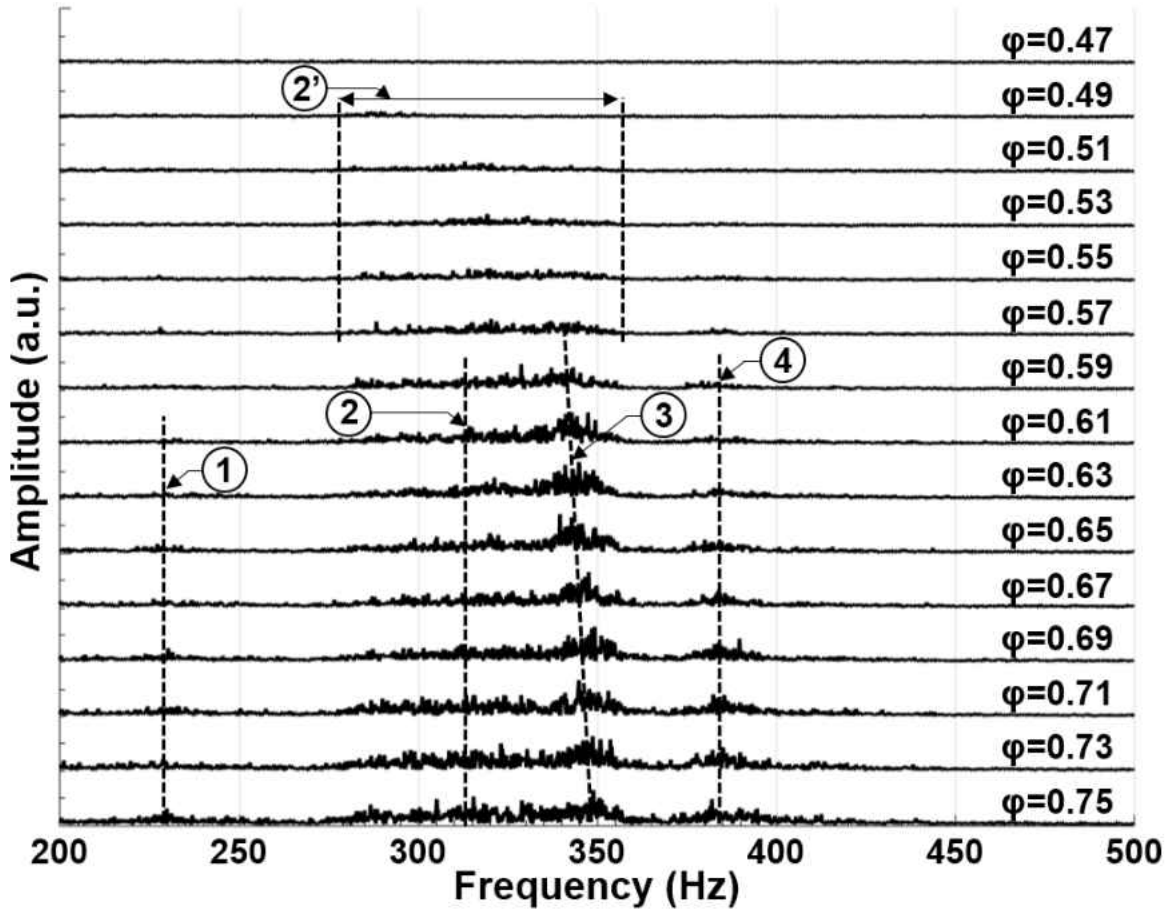


Figure 4-20: Acoustic profiles from the combustion chamber with a Pd-WC catalyst.

As it has been shown that heat release rates drive acoustic modes within combustion chambers [178], it is possible to draw correlations between the observed changes in acoustic profiles at different equivalence ratios with temperature profiles and flame structure within the combustion chamber containing a WC-Pd catalytically enhanced MSZ porous media. As equivalence ratios are decreased with a constant air flow rate, both the total acoustic energy and maximum temperature profile within the combustion chamber decrease. As the equivalence ratio shifts between below  $\phi=0.75\pm 0.02$  until  $\phi=0.59\pm 0.02$  and the flame shifts away from the inlet, there is a significant decrease in the observed amplitudes of peaks (1) and (4) indicating these peaks in the acoustic spectrum correlate with stable structures of flow at the combustion chamber inlet. Lastly,

as the flame elongates within the combustion chamber which is most pronounced at equivalence ratios below  $\varphi=0.59\pm 0.02$  the intensity of the acoustic emissions associated with peak (iii) decreases and the nominal intensity of this peak becomes increasingly homogeneous. No acoustic signal can be detected at  $\varphi=0.47\pm 0.02$  which correlates with nearly isothermal and rather low temperatures across the entire combustion chamber.



## 5. CONCLUSIONS

Within this work a flow stabilized heterogeneous combustion chamber was developed with several instrumentation techniques to characterize combustion. Such techniques were: temperature measurements via thermocouples, exhaust sample analysis via gas chromatography, acoustic spectroscopy using an external microphone, and an external CCD camera to collect optical emissions from the combustion chamber. Performed experiments within the combustion chamber were done at a fixed air flow rate of  $\dot{V}_{air}=47.56$  SLPM and equivalence ratios on the order of  $0.45 \leq \phi \leq 0.75$ . Three types of porous media were evaluated, MSZ, SiC, and  $Al_2O_3$ . Of these media types, MSZ enabled the highest temperatures at low equivalence operation.

For the first time acoustic spectroscopy was utilized as a characterization tool for heterogeneous combustion. Using acoustic spectroscopy it was shown that there is a dependence of the acoustic profile of the combustor based on position of the flame, equivalence ratio, and structure of the flame within the combustion chamber.

As MSZ enabled the highest temperatures at low equivalence ratio, it was evaluated as a substrate to support several catalysts: Pd enhanced WC,  $ZrB_2$ ,  $Ce_{0.80}Gd_{0.20}O_{1.90}$ ,  $LaCoO_3$ ,  $La_{0.80}Ca_{0.20}CoO_3$ ,  $La_{0.75}Sr_{0.25}Fe_{0.95}Ru_{0.05}O_3$ , and  $La_{0.75}Sr_{0.25}Cr_{0.95}Ru_{0.05}O_3$ . Of the evaluated catalysts,  $LaCoO_3$  enabled the highest temperatures within the combustion chamber and operation at the lowest equivalence ratio of  $\phi=0.45 \pm 0.02$ .

## REFERENCES

- [1] I. Glassman and R. Yetter, *Combustion*: Academic press, 2008.
- [2] S. R. Turns, *An introduction to combustion* vol. 287: McGraw-hill New York, 1996.
- [3] C. Law and F. Egolfopoulos, "A kinetic criterion of flammability limits: The CHO-inert system," in *Symposium (International) on Combustion*, 1991, pp. 413-421.
- [4] A. Kronenburg, R. Bilger, and J. Kent, "Modeling soot formation in turbulent methane-air jet diffusion flames," *Combustion and Flame*, vol. 121, pp. 24-40, 2000.
- [5] M. Frenklach, "Reaction mechanism of soot formation in flames," *Physical Chemistry Chemical Physics*, vol. 4, pp. 2028-2037, 2002.
- [6] X. Zhou and J. Pereira, "Comparison of four combustion models for simulating the premixed combustion in inert porous media," *Fire and Materials*, vol. 22, pp. 187-197, 1998.
- [7] O. Herbinet, W. J. Pitz, and C. K. Westbrook, "Detailed chemical kinetic mechanism for the oxidation of biodiesel fuels blend surrogate," *Combustion and Flame*, vol. 157, pp. 893-908, 2010.
- [8] A. Abou-Taouk, S. Sadasivuni, D. Lörstad, B. Ghenadie, and L.-E. Eriksson, "CFD analysis and application of dynamic mode decomposition for resonant-mode identification and damping in an SGT-100 DLE combustion system," in *Proceedings of the 7th European Combustion Meeting*, 2015.
- [9] G. P. Smith, D. M. Golden, M. Frenklach, N. W. Moriarty, B. Eiteneer, M. Goldenberg, *et al.*, "GRI-Mech 3.0," ed, 1999.
- [10] G. Sivashinsky, "Structure of Bunsen flames," *The Journal of Chemical Physics*, vol. 62, pp. 638-643, 1975.
- [11] J. Bechtel and R. Teets, "Hydroxyl and its concentration profile in methane-air flames," *Applied Optics*, vol. 18, pp. 4138-4144, 1979.
- [12] A. Van Maaren, D. Thung, and L. R. H. DE GOEY, "Measurement of flame temperature and adiabatic burning velocity of methane/air mixtures," *Combustion Science and Technology*, vol. 96, pp. 327-344, 1994.

- [13] S. Liao, D. Jiang, J. Gao, and Z. Huang, "Measurements of Markstein numbers and laminar burning velocities for natural gas-air mixtures," *Energy & fuels*, vol. 18, pp. 316-326, 2004.
- [14] A. Cybulski and J. A. Moulijn, "Monoliths in heterogeneous catalysis," *Catalysis Reviews—Science and Engineering*, vol. 36, pp. 179-270, 1994.
- [15] L. Giani, G. Groppi, and E. Tronconi, "Mass-transfer characterization of metallic foams as supports for structured catalysts," *Industrial & engineering chemistry research*, vol. 44, pp. 4993-5002, 2005.
- [16] W. R. Gustafson, "Shaped catalyst particles," ed: Google Patents, 1976.
- [17] S. Wood and A. T. Harris, "Porous burners for lean-burn applications," *Progress in Energy and Combustion Science*, vol. 34, pp. 667-684, 2008.
- [18] W. Xu, H. Zhang, Z. Yang, and J. Zhang, "Numerical investigation on the flow characteristics and permeability of three-dimensional reticulated foam materials," *Chemical Engineering Journal*, vol. 140, pp. 562-569, 2008.
- [19] B. Stelzner, C. Keramiotis, S. Voss, M. Founti, and D. Trimis, "Analysis of the flame structure for lean methane–air combustion in porous inert media by resolving the hydroxyl radical," *Proceedings of the Combustion Institute*, vol. 35, pp. 3381-3388, 2015.
- [20] T. Takeno, K. Sato, and K. Hase, "A theoretical study on an excess enthalpy flame," in *Symposium (International) on Combustion*, 1981, pp. 465-472.
- [21] K. V. Dobrego, S. A. Zhdanok, and E. I. Khanevich, "Analytical and experimental investigation of the transition from low-velocity to high-velocity regime of filtration combustion," *Experimental Thermal and Fluid Science*, vol. 21, pp. 9-16, 2000.
- [22] V. Babkin, V. Drobyshevich, Y. M. Laevskii, and S. Potytnyakov, "Filtration combustion of gases," *Combustion, Explosion and Shock Waves*, vol. 19, pp. 147-155, 1983.
- [23] K. Hanamura, R. Echigo, and S. A. Zhdanok, "Superadiabatic combustion in a porous medium," *International Journal of Heat and Mass Transfer*, vol. 36, pp. 3201-3209, 1993.
- [24] A. Oliveira and M. Kaviany, "Nonequilibrium in the transport of heat and reactants in combustion in porous media," *Progress in Energy and Combustion Science*, vol. 27, pp. 523-545, 2001.

- [25] V. Babkin and Y. M. Laevskii, "Seepage gas combustion," *Combustion, Explosion, and Shock Waves*, vol. 23, pp. 531-547, 1987.
- [26] F. Weinberg, "Combustion temperatures: the future?," *Nature*, vol. 233, pp. 239-241, 1971.
- [27] B. Manuel Robayo, Delose, Dasgupta, Nina Orlovskaya, Chen, "Perovskite catalysts enhanced combustion inside of the porous media," *Applied Energy*, In preparation for submission.
- [28] K. T. Mueller, O. Waters, V. Bubnovich, N. Orlovskaya, and R.-H. Chen, "Super-adiabatic combustion in Al<sub>2</sub>O<sub>3</sub> and SiC coated porous media for thermoelectric power conversion," *Energy*, vol. 56, pp. 108-116, 2013.
- [29] K. Hanamura and R. Echigo, "An analysis of flame stabilization mechanism in radiation burners," *Wärme-und Stoffübertragung*, vol. 26, pp. 377-383, 1991.
- [30] M. K. Drayton, A. V. Saveliev, L. A. Kennedy, A. A. Fridman, and Y.-E. D. Li, "Syngas production using superadiabatic combustion of ultra-rich methane-air mixtures," in *Symposium (International) on Combustion*, 1998, pp. 1361-1367.
- [31] J.-R. Shi, M.-Z. Xie, G. Li, H. Liu, J.-T. Liu, and H.-T. Li, "Approximate solutions of lean premixed combustion in porous media with reciprocating flow," *International Journal of Heat and Mass Transfer*, vol. 52, pp. 702-708, 2009.
- [32] Y. Chen, R. Matthews, and J. Howell, "The effect of radiation on the structure of premixed flame within a highly porous inert medium," *Radiation, Phase Change Heat Transfer and Thermal Systems*, vol. 81, pp. 35-42, 1987.
- [33] D. Trimis and K. Wawrzinek, "Flame stabilization of highly diffusive gas mixtures in porous inert media," *J Comput Appl Mech*, vol. 5, pp. 367-81, 2004.
- [34] P. Carman, "Permeability of saturated sands, soils and clays," *The Journal of Agricultural Science*, vol. 29, pp. 262-273, 1939.
- [35] R. Fand, B. Kim, A. Lam, and R. Phan, "Resistance to the flow of fluids through simple and complex porous media whose matrices are composed of randomly packed spheres," *Journal of fluids engineering*, vol. 109, pp. 268-273, 1987.

- [36] T. Perkins and O. Johnston, "A review of diffusion and dispersion in porous media," *Society of Petroleum Engineers Journal*, vol. 3, pp. 70-84, 1963.
- [37] E. L. Cussler, *Diffusion: mass transfer in fluid systems*: Cambridge university press, 2009.
- [38] J. Howell, M. Hall, and J. Ellzey, "Combustion of hydrocarbon fuels within porous inert media," *Progress in Energy and Combustion Science*, vol. 22, pp. 121-145, 1996.
- [39] T. Takeno and K. Sato, "An excess enthalpy flame theory," *Combustion Science and Technology*, vol. 20, pp. 73-84, 1979.
- [40] J. Hirschfelder, C. Curtiss, and D. E. Campbell, "The theory of flames and detonations," in *Symposium (International) on Combustion*, 1953, pp. 190-211.
- [41] F. A. Williams, *Combustion Theory: the fundamental theory of chemical reacting flow systems*: Addison-Wesley, 1965.
- [42] V. Maizza and A. Maizza, "Unconventional working fluids in organic Rankine-cycles for waste energy recovery systems," *Applied Thermal Engineering*, vol. 21, pp. 381-390, 2001.
- [43] B. C. Steele and A. Heinzl, "Materials for fuel-cell technologies," *Nature*, vol. 414, pp. 345-352, 2001.
- [44] H. Pedersen-Mjaanes, L. Chan, and E. Mastorakos, "Hydrogen production from rich combustion in porous media," *International journal of hydrogen energy*, vol. 30, pp. 579-592, 2005.
- [45] M. K. Hubbert and D. G. Willis, "Mechanics of hydraulic fracturing," 1972.
- [46] A. Hudgins, "Fracking's future in a coal mining past: subjectivity undermined," *Culture, Agriculture, Food and Environment*, vol. 35, pp. 54-59, 2013.
- [47] G. Moore, R. Young, and H. Toulmin, "Effect of Fuel Volatility on Starting and Warmup of New Automobiles," SAE Technical Paper1957.
- [48] J. X. Ma, D. R. Alexander, and D. E. Poulain, "Laser spark ignition and combustion characteristics of methane-air mixtures," *Combustion and Flame*, vol. 112, pp. 492-506, 1998.
- [49] P. D. Ronney, "Laser versus conventional ignition of flames," *Optical Engineering*, vol. 33, pp. 510-521, 1994.

- [50] H. Kopecek, H. Maier, G. Reider, F. Winter, and E. Wintner, "Laser ignition of methane–air mixtures at high pressures," *Experimental Thermal and Fluid Science*, vol. 27, pp. 499-503, 2003.
- [51] P.-A. Bui, D. Vlachos, and P. Westmoreland, "Catalytic ignition of methane/oxygen mixtures over platinum surfaces: comparison of detailed simulations and experiments," *Surface science*, vol. 385, pp. L1029-L1034, 1997.
- [52] G. Brenner, K. Pickenäcker, O. Pickenäcker, D. Trimis, K. Wawrzinek, and T. Weber, "Numerical and experimental investigation of matrix-stabilized methane/air combustion in porous inert media," *Combustion and flame*, vol. 123, pp. 201-213, 2000.
- [53] M. Kaplan and M. J. Hall, "The combustion of liquid fuels within a porous media radiant burner," *Experimental Thermal and Fluid Science*, vol. 11, pp. 13-20, 1995.
- [54] A. C. Terracciano, "Design and Development of Heterogenous Combustion Systems for Lean Burn Applications," University of Central Florida Orlando, Florida, 2014.
- [55] J. L. ELLZEY and R. Goel, "Emissions of CO and NO from a two stage porous media burner," *Combustion science and technology*, vol. 107, pp. 81-91, 1995.
- [56] J. Peirs, D. Reynaerts, and F. Verplaetsen, "Development of an axial microturbine for a portable gas turbine generator," *Journal of Micromechanics and Microengineering*, vol. 13, p. S190, 2003.
- [57] C. Schulz and V. Sick, "Tracer-LIF diagnostics: quantitative measurement of fuel concentration, temperature and fuel/air ratio in practical combustion systems," *Progress in Energy and Combustion Science*, vol. 31, pp. 75-121, 2005.
- [58] N. D. Joshi, E. E. Ekstedt, and M. J. Epstein, "Air fuel mixer for gas turbine combustor," ed: Google Patents, 1993.
- [59] M. Kamal and A. Mohamad, "Enhanced radiation output from foam burners operating with a nonpremixed flame," *Combustion and flame*, vol. 140, pp. 233-248, 2005.
- [60] C. Law, "Recent advances in droplet vaporization and combustion," *Progress in energy and combustion science*, vol. 8, pp. 171-201, 1982.

- [61] M. A. Mujeebu, M. Abdullah, M. A. Bakar, A. Mohamad, and M. Abdullah, "A review of investigations on liquid fuel combustion in porous inert media," *Progress in Energy and Combustion Science*, vol. 35, pp. 216-230, 2009.
- [62] S. Jugjai, N. Wongpanit, T. Laoketkan, and S. Nokkaew, "The combustion of liquid fuels using a porous medium," *Experimental Thermal and Fluid Science*, vol. 26, pp. 15-23, 2002.
- [63] T. Fuse, N. Kobayashi, and M. Hasatani, "Combustion characteristics of ethanol in a porous ceramic burner and ignition improved by enhancement of liquid-fuel intrusion in the pore with ultrasonic irradiation," *Experimental thermal and fluid science*, vol. 29, pp. 467-476, 2005.
- [64] S. D. Givler and J. Abraham, "Supercritical droplet vaporization and combustion studies," *Progress in Energy and combustion Science*, vol. 22, pp. 1-28, 1996.
- [65] E. R. Newburn and A. K. Agrawal, "Liquid fuel combustion using heat recirculation through annular porous media," *Journal of Engineering for Gas Turbines and Power*, vol. 129, pp. 914-919, 2007.
- [66] B. Belaisaoui, G. Cabot, M.-S. Cabot, D. Willson, and E. Favre, "CO<sub>2</sub> capture for gas turbines: an integrated energy-efficient process combining combustion in oxygen-enriched air, flue gas recirculation, and membrane separation," *Chemical Engineering Science*, vol. 97, pp. 256-263, 2013.
- [67] J. H. Sharp, M. Scheurlen, and M. B. Hansel, "COMBINED CYCLE PLANT INJECTION WATER PREHEATING ARRANGEMENT," ed: US Patent 20,150,192,038, 2015.
- [68] S. Roux, G. Lartigue, T. Poinso, U. Meier, and C. Bérat, "Studies of mean and unsteady flow in a swirled combustor using experiments, acoustic analysis, and large eddy simulations," *Combustion and Flame*, vol. 141, pp. 40-54, 2005.
- [69] N. Syred, "A review of oscillation mechanisms and the role of the precessing vortex core (PVC) in swirl combustion systems," *Progress in Energy and Combustion Science*, vol. 32, pp. 93-161, 2006.
- [70] A. Klein, "Characteristics of combustor diffusers," *Progress in Aerospace Sciences*, vol. 31, pp. 171-271, 1995.
- [71] A. Revuelta, "On the two-dimensional flow in a sudden expansion with large expansion ratios," *Physics of Fluids (1994-present)*, vol. 17, p. 028102, 2005.

- [72] R. Hermann, *Supersonic inlet diffusers and introduction to internal aerodynamics*: Minneapolis-Honeywell Regulator Company, Aeronautical Division, 1956.
- [73] Y. Huang and V. Yang, "Effect of swirl on combustion dynamics in a lean-premixed swirl-stabilized combustor," *Proceedings of the Combustion Institute*, vol. 30, pp. 1775-1782, 2005.
- [74] S. Alavandi and A. Agrawal, "Experimental study of combustion of hydrogen-syngas/methane fuel mixtures in a porous burner," *International Journal of Hydrogen Energy*, vol. 33, pp. 1407-1415, 2008.
- [75] M. D. Robayo, B. Beaman, B. Hughes, B. Delose, N. Orlovskaya, and R.-H. Chen, "Perovskite catalysts enhanced combustion on porous media," *Energy*, vol. 76, pp. 477-486, 2014.
- [76] O. Pickenäcker, K. Pickenäcker, K. Wawrzinek, D. Trimis, W. Pritzkow, C. Müller, *et al.*, "Innovative ceramic materials for porous-medium burners, II," *Interceram*, vol. 48, pp. 424-433, 1999.
- [77] P.-F. Hsu, W. D. EVANS, and J. R. HOWELL, "Experimental and numerical study of premixed combustion within nonhomogeneous porous ceramics," *Combustion Science and Technology*, vol. 90, pp. 149-172, 1993.
- [78] S. Brunauer, P. H. Emmett, and E. Teller, "Adsorption of gases in multimolecular layers," *Journal of the American chemical society*, vol. 60, pp. 309-319, 1938.
- [79] M. A. Mujeebu, M. Z. Abdullah, A. Mohamad, and M. A. Bakar, "Trends in modeling of porous media combustion," *Progress in Energy and Combustion science*, vol. 36, pp. 627-650, 2010.
- [80] C. Keramiotis, B. Stelzner, D. Trimis, and M. Founti, "Porous burners for low emission combustion: An experimental investigation," *Energy*, vol. 45, pp. 213-219, 2012.
- [81] J. Hoffmann, R. Echigo, H. Yoshida, and S. Tada, "Experimental study on combustion in porous media with a reciprocating flow system," *Combustion and Flame*, vol. 111, pp. 32-46, 1997.
- [82] A. K. Ismail, M. Z. Abdullah, M. Zubair, Z. A. Ahmad, A. R. Jamaludin, K. F. Mustafa, *et al.*, "Application of porous medium burner with micro cogeneration system," *Energy*, vol. 50, pp. 131-142, 2013.



- [83] N. Mishra, S. C. Mishra, and P. Muthukumar, "Performance characterization of a medium-scale liquefied petroleum gas cooking stove with a two-layer porous radiant burner," *Applied Thermal Engineering*, vol. 89, pp. 44-50, 2015.
- [84] K. Naumann and L. Stadler, "DOUBLE-PULSE SOLID ROCKET MOTOR TECHNOLOGY–APPLICATIONS AND TECHNICAL SOLUTIONS," *Pulse*, vol. 1, p. P2, 2010.
- [85] G. Bulat, W. Jones, and A. Marquis, "NO and CO formation in an industrial gas-turbine combustion chamber using LES with the Eulerian sub-grid PDF method," *Combustion and Flame*, vol. 161, pp. 1804-1825, 2014.
- [86] R. Rajendran, "Gas turbine coatings–An overview," *Engineering Failure Analysis*, vol. 26, pp. 355-369, 2012.
- [87] T. G. Wakeman, A. Walker, and H. M. Maclin, "Gas turbine engine multi-hole film cooled combustor liner and method of manufacture," ed: Google Patents, 1993.
- [88] A. Fichera, C. Losenno, and A. Pagano, "Experimental analysis of thermoacoustic combustion instability," *Applied Energy*, vol. 70, pp. 179-191, 2001.
- [89] V. Hindasageri, R. Vedula, and S. Prabhu, "Thermocouple error correction for measuring the flame temperature with determination of emissivity and heat transfer coefficient," *Review of Scientific Instruments*, vol. 84, p. 024902, 2013.
- [90] P. Molcan, G. Lu, T. Le Bris, Y. Yan, B. Taupin, and S. Caillat, "Characterisation of biomass and coal co-firing on a 3MWth combustion test facility using flame imaging and gas/ash sampling techniques," *Fuel*, vol. 88, pp. 2328-2334, 2009.
- [91] J. R. Howell, R. Siegel, and M. P. Menguc, *Thermal radiation heat transfer*: CRC press, 2010.
- [92] C. F. Poole, *Gas Chromatography*: Elsevier, 2012.
- [93] D. Smith and E. Zukoski, "Combustion instability sustained by unsteady vortex combustion," 1985.
- [94] L. A. Clifton, H. Yin, and Y. Zhang, "Support vector machine in novelty detection for multi-channel combustion data," in *Advances in Neural Networks-ISNN 2006*, ed: Springer, 2006, pp. 836-843.

- [95] M. L. Frezzotti, A. Terracciano, F. Nasuti, S. Hester, and W. E. Anderson, "Low-order model studies of combustion instabilities in a DVRC combustor," in *50th AIAA/ASME/SAE/ASEE Joint Propulsion Conference*, 2014, p. 3485.
- [96] L. Beranek, "Acoustics (Acoustical Society of America, New York, 1993)," *Original work published by McGraw-Hill, New York*, pp. 47-77, 1954.
- [97] S. Dahl, A. Logadottir, R. Egeberg, J. Larsen, I. Chorkendorff, E. Törnqvist, *et al.*, "Role of steps in N<sub>2</sub> activation on Ru (0001)," *Physical Review Letters*, vol. 83, p. 1814, 1999.
- [98] D. Moy and A. Chishti, "Methods and catalysts for the manufacture of carbon fibrils," ed: Google Patents, 2000.
- [99] D. F. Ollis and C. Turchi, "Heterogeneous photocatalysis for water purification: Contaminant mineralization kinetics and elementary reactor analysis," *Environmental progress*, vol. 9, pp. 229-234, 1990.
- [100] P. Bandyopadhyay, M. Sathe, G. Prasad, P. Sharma, and M. Kaushik, "Mesoporous mixed metal oxide nanocrystals: efficient and recyclable heterogeneous catalysts for the synthesis of 1, 2-disubstituted benzimidazoles and 2-substituted benzothiazoles," *Journal of Molecular Catalysis A: Chemical*, vol. 341, pp. 77-82, 2011.
- [101] P. Forzatti and L. Lietti, "Catalyst deactivation," *Catalysis today*, vol. 52, pp. 165-181, 1999.
- [102] F. Durst and D. Trimis, "Combustion by free flames versus combustion reactors," *Clean Air*, vol. 3, pp. 1-20, 2002.
- [103] W. M. Mathis and J. L. Ellzey, "Flame stabilization, operating range, and emissions for a methane/air porous burner," *Combustion Science and Technology*, vol. 175, pp. 825-839, 2003.
- [104] S. Chou, W. Yang, J. Li, and Z. Li, "Porous media combustion for micro thermophotovoltaic system applications," *Applied Energy*, vol. 87, pp. 2862-2867, 2010.
- [105] V. I. Bubnovich, N. Orlovskaya, L. A. Henríquez-Vargas, and F. E. Ibacache, "Experimental Thermoelectric Generation in a Porous Media Burner," *International Journal of Chemical Engineering and Applications*, vol. 4, p. 301, 2013.

- [106] J. Greeley, J. K. Nørskov, and M. Mavrikakis, "Electronic structure and catalysis on metal surfaces," *Annual Review of Physical Chemistry*, vol. 53, pp. 319-348, 2002.
- [107] M. F. Zwinkels, S. G. Järås, P. G. Menon, and T. A. Griffin, "Catalytic materials for high-temperature combustion," *Catalysis Reviews—Science and Engineering*, vol. 35, pp. 319-358, 1993.
- [108] B. Hornetz, H. Michel, and J. Halbritter, "ARXPS studies of SiO<sub>2</sub>-SiC interfaces and oxidation of 6H SiC single crystal Si-(001) and C-(00 1) surfaces," *Journal of materials research*, vol. 9, pp. 3088-3094, 1994.
- [109] K. Tanabe, "Surface and catalytic properties of ZrO<sub>2</sub>," *Materials Chemistry and Physics*, vol. 13, pp. 347-364, 1985.
- [110] A. Trovarelli, "Catalytic properties of ceria and CeO<sub>2</sub>-containing materials," *Catalysis Reviews*, vol. 38, pp. 439-520, 1996.
- [111] E. Ramirez-Cabrera, A. Atkinson, and D. Chadwick, "Reactivity of ceria, Gd- and Nb-doped ceria to methane," *Applied Catalysis B: Environmental*, vol. 36, pp. 193-206, 2002.
- [112] M. Barsoum and M. Barsoum, *Fundamentals of ceramics*: CRC press, 2002.
- [113] B. T. Kilbourn, *Cerium: A guide to its role in chemical technology*: Molycorp, 1992.
- [114] C. Li, Q. Xin, X. Gua, and T. Onishi, "Surface Oxygen Species and Their Reactivities in the Oxidation of CH<sub>4</sub>, C<sub>2</sub>H<sub>6</sub> and C<sub>2</sub>H<sub>4</sub> Over Cerium Oxide at Mild Temperatures," *Studies in Surface Science and Catalysis*, vol. 75, pp. 1955-1958, 1993.
- [115] C. Li and Q. Xin, "FT-IR spectroscopic investigation of methane adsorption on cerium oxide," *The Journal of Physical Chemistry*, vol. 96, pp. 7714-7718, 1992.
- [116] C. Li, Q. Xin, and X.-x. Guo, "Surface oxygen species and their reactivities in the mild oxidation of ethylene on cerium oxide studied by FT-IR spectroscopy," *Catalysis letters*, vol. 12, pp. 297-305, 1992.
- [117] V. Choudhary and V. Rane, "Acidity/basicity of rare-earth oxides and their catalytic activity in oxidative coupling of methane to C 2-hydrocarbons," *Journal of Catalysis*, vol. 130, pp. 411-422, 1991.

- [118] M. Alifanti, N. Blangenois, M. Florea, and B. Delmon, "Supported Co-based perovskites as catalysts for total oxidation of methane," *Applied Catalysis A: General*, vol. 280, pp. 255-265, 2005.
- [119] G. Balducci, J. Kašpar, P. Fornasiero, M. Graziani, and M. S. Islam, "Surface and reduction energetics of the CeO<sub>2</sub>-ZrO<sub>2</sub> catalysts," *The Journal of Physical Chemistry B*, vol. 102, pp. 557-561, 1998.
- [120] T. Kuznetsova, V. Sadykov, L. Batuev, E. Moroz, E. Burgina, V. Rogov, *et al.*, "Modified Ceria-Zirconia Fluorite-Like Catalysts for the Combustion of Methane," *Journal of Natural Gas Chemistry*, vol. 15, pp. 149-163, 2006.
- [121] Y. Chen, N. Orlovskaya, M. Klimov, X. Huang, D. Cullen, T. Graule, *et al.*, "Layered YSZ/SCSZ/YSZ electrolytes for intermediate temperature SOFC Part I: design and manufacturing," *Fuel Cells*, vol. 12, pp. 722-731, 2012.
- [122] R. Heikes, R. Miller, and R. Mazelsky, "Magnetic and electrical anomalies in LaCoO<sub>3</sub>," *Physica*, vol. 30, pp. 1600-1608, 1964.
- [123] M. Itoh, M. Sugahara, I. Natori, and K. Motoya, "Spin state and hyperfine interaction in LaCoO<sub>3</sub>: NMR and magnetic susceptibility studies," *Journal of the Physical Society of Japan*, vol. 64, pp. 3967-3977, 1995.
- [124] N. Orlovskaya, Y. Gogotsi, M. Reece, B. Cheng, and I. Gibson, "Ferroelasticity and hysteresis in LaCoO<sub>3</sub> based perovskites," *Acta materialia*, vol. 50, pp. 715-723, 2002.
- [125] L. Nomerovannaya, A. Makhnev, S. Streltsov, I. Nekrasov, M. Korotin, S. Shiryayev, *et al.*, "The influence of the Co<sup>3+</sup> spin state on the optical properties of LaCoO<sub>3</sub> and HoCoO<sub>3</sub>," *Journal of Physics: Condensed Matter*, vol. 16, p. 5129, 2004.
- [126] B. Białobok, J. Trawczyński, W. Miśta, and M. Zawadzki, "Ethanol combustion over strontium-and cerium-doped LaCoO<sub>3</sub> catalysts," *Applied Catalysis B: Environmental*, vol. 72, pp. 395-403, 2007.
- [127] H. Zhu, P. Zhang, and S. Dai, "Recent advances of lanthanum-based perovskite oxides for catalysis," *ACS Catalysis*, vol. 5, pp. 6370-6385, 2015.
- [128] S. Royer, H. Alamdari, D. Duprez, and S. Kaliaguine, "Oxygen storage capacity of La<sub>1-x</sub>A'<sub>x</sub>BO<sub>3</sub> perovskites (with A'= Sr, Ce; B= Co, Mn)—relation with catalytic activity in the CH<sub>4</sub> oxidation reaction," *Applied Catalysis B: Environmental*, vol. 58, pp. 273-288, 2005.

- [129] H. Arai, T. Yamada, K. Eguchi, and T. Seiyama, "Catalytic combustion of methane over various perovskite-type oxides," *Applied catalysis*, vol. 26, pp. 265-276, 1986.
- [130] T. Sawada and T. Akashi, "Grain Growth Behavior of  $\text{La}_{0.6}\text{Sr}_{0.4}\text{CoO}_{3-\delta}$  Film Dispersed with a Second Phase," *ECS Transactions*, vol. 16, pp. 199-204, 2009.
- [131] H. Meng, P. K. Shen, Z. Wei, and S. P. Jiang, "Improved Performance of Direct Methanol Fuel Cells with Tungsten Carbide Promoted Pt/C Composite Cathode Electrocatalyst," *Electrochemical and solid-state letters*, vol. 9, pp. A368-A372, 2006.
- [132] M. Rosenbaum, F. Zhao, M. Quaas, H. Wulff, U. Schröder, and F. Scholz, "Evaluation of catalytic properties of tungsten carbide for the anode of microbial fuel cells," *Applied Catalysis B: Environmental*, vol. 74, pp. 261-269, 2007.
- [133] E. Antolini and E. R. Gonzalez, "Tungsten-based materials for fuel cell applications," *Applied Catalysis B: Environmental*, vol. 96, pp. 245-266, 2010.
- [134] D. Baresel, W. Gellert, J. Heidemeyer, and P. Scharner, "Tungsten carbide as anode material for fuel cells," *Angewandte Chemie International Edition in English*, vol. 10, pp. 194-195, 1971.
- [135] P. N. Ross and P. Stonehart, "The relation of surface structure to the electrocatalytic activity of tungsten carbide," *Journal of Catalysis*, vol. 48, pp. 42-59, 1977.
- [136] D. McIntyre, G. Burstein, and A. Vossen, "Effect of carbon monoxide on the electrooxidation of hydrogen by tungsten carbide," *Journal of Power Sources*, vol. 107, pp. 67-73, 2002.
- [137] V. S. Palanker, R. Gajyev, and D. Sokolsky, "On adsorption and electro-oxidation of some compounds on tungsten carbide; their effect on hydrogen electro-oxidation," *Electrochimica Acta*, vol. 22, pp. 133-136, 1977.
- [138] R. Levy and M. Boudart, "Platinum-like behavior of tungsten carbide in surface catalysis," *science*, vol. 181, pp. 547-549, 1973.
- [139] K. Lee, A. Ishihara, S. Mitsushima, N. Kamiya, and K.-i. Ota, "Stability and electrocatalytic activity for oxygen reduction in WC+ Ta catalyst," *Electrochimica Acta*, vol. 49, pp. 3479-3485, 2004.

- [140] D. Ciuparu, M. R. Lyubovsky, E. Altman, L. D. Pfefferle, and A. Datye, "Catalytic combustion of methane over palladium-based catalysts," *Catalysis Reviews*, vol. 44, pp. 593-649, 2002.
- [141] R. Burch and M. Hayes, "C-H bond activation in hydrocarbon oxidation on solid catalysts," *Journal of Molecular Catalysis A: Chemical*, vol. 100, pp. 13-33, 1995.
- [142] J. Au-Yeung, K. Chen, A. T. Bell, and E. Iglesia, "Isotopic studies of methane oxidation pathways on PdO catalysts," *Journal of Catalysis*, vol. 188, pp. 132-139, 1999.
- [143] H. Conrad, G. Ertl, J. Küppers, and E. Latta, "Interaction of NO and O<sub>2</sub> with Pd (111) surfaces. II," *Surface Science*, vol. 65, pp. 245-260, 1977.
- [144] Y. Lu, J. Li, J. Han, H.-T. Ng, C. Binder, C. Partridge, *et al.*, "Room temperature methane detection using palladium loaded single-walled carbon nanotube sensors," *Chemical Physics Letters*, vol. 391, pp. 344-348, 2004.
- [145] N. Mohajeri, T. Ali, G. Bokerman, J. E. Captain, B. V. Peterson, M. Whitten, *et al.*, "TEM-XRD analysis of PdO particles on TiO<sub>2</sub> support for chemochromic detection of hydrogen," *Sensors and Actuators B: Chemical*, vol. 144, pp. 208-214, 2010.
- [146] S. Yang, A. Maroto-Valiente, M. Benito-Gonzalez, I. Rodriguez-Ramos, and A. Guerrero-Ruiz, "Methane combustion over supported palladium catalysts: I. Reactivity and active phase," *Applied Catalysis B: Environmental*, vol. 28, pp. 223-233, 2000.
- [147] W. S. Epling and G. B. Hoflund, "Catalytic oxidation of methane over ZrO<sub>2</sub>-supported Pd catalysts," *Journal of Catalysis*, vol. 182, pp. 5-12, 1999.
- [148] M. Cargnello, J. D. Jaén, J. H. Garrido, K. Bakhtmutsky, T. Montini, J. C. Gámez, *et al.*, "Exceptional activity for methane combustion over modular Pd@ CeO<sub>2</sub> subunits on functionalized Al<sub>2</sub>O<sub>3</sub>," *Science*, vol. 337, pp. 713-717, 2012.
- [149] D. Ciuparu, E. Altman, and L. Pfefferle, "Contributions of lattice oxygen in methane combustion over PdO-based catalysts," *Journal of Catalysis*, vol. 203, pp. 64-74, 2001.
- [150] D. Ciuparu, F. Bozon-Verduraz, and L. Pfefferle, "Oxygen exchange between palladium and oxide supports in combustion catalysts," *The Journal of Physical Chemistry B*, vol. 106, pp. 3434-3442, 2002.

- [151] A. C. Terracciano, S. S. Vasu, and N. Orlovskaya, "Design and development of a porous heterogeneous combustor for efficient heat production by combustion of liquid and gaseous fuels," *Applied Energy*, vol. 179, pp. 228-236, 2016.
- [152] (2016). *ASK Chemicals Foundry Products*  
Available: <http://www.ask-chemicals.com/foundry-products/products/filters.html>
- [153] J. Pan, D. Wu, Y. Liu, H. Zhang, A. Tang, and H. Xue, "Hydrogen/oxygen premixed combustion characteristics in micro porous media combustor," *Applied Energy*, vol. 160, pp. 802-807, 2015.
- [154] H. Gao, Z. Qu, X. Feng, and W. Tao, "Combustion of methane/air mixtures in a two-layer porous burner: A comparison of alumina foams, beads, and honeycombs," *Experimental Thermal and Fluid Science*, vol. 52, pp. 215-220, 2014.
- [155] J.-R. Shi, C.-M. Yu, B.-W. Li, Y.-F. Xia, and Z.-J. Xue, "Experimental and numerical studies on the flame instabilities in porous media," *Fuel*, vol. 106, pp. 674-681, 2013.
- [156] F. Durst, T. Maxworthy, and J. Pereira, "Piston-driven, unsteady separation at a sudden expansion in a tube: Flow visualization and LDA measurements," *Physics of Fluids A: Fluid Dynamics (1989-1993)*, vol. 1, pp. 1249-1260, 1989.
- [157] H. Frazer, "Flow recirculation in centrifugal pumps," in *ASME meeting*, 1981.
- [158] R. W. Wyckoff, "IX. Die Kristallstruktur von  $\beta$ -Cristobalit  $\text{SiO}_2$  (bei hohen Temperaturen stabile Form)," *Zeitschrift für Kristallographie-Crystalline Materials*, vol. 62, pp. 189-200, 1925.
- [159] C. Burdick and E. Owen, "THE ATOMIC STRUCTURE OF CARBORUNDUM DETERMINED BY X-RAYS," *Journal of the American Chemical Society*, vol. 40, pp. 1749-1759, 1918.
- [160] M. Dubey, U. Ram, and G. Singh, "A new polytype of silicon carbide, 189R. Its structure and growth," *Acta Crystallographica Section B: Structural Crystallography and Crystal Chemistry*, vol. 29, pp. 1548-1550, 1973.
- [161] L. Ramsdell and J. Kohn, "Developments in silicon carbide research," *Acta Crystallographica*, vol. 5, pp. 215-224, 1952.

- [162] H. Ott, "Die Gitterstruktur des Karborunds (SiC)," *Naturwissenschaften*, vol. 13, pp. 319-319, 1925.
- [163] P. Bouvier, E. Djurado, C. Ritter, A. Dianoux, and G. Lucazeau, "Low temperature phase transformation of nanocrystalline tetragonal ZrO<sub>2</sub> by neutron and Raman scattering studies," *International Journal of Inorganic Materials*, vol. 3, pp. 647-654, 2001.
- [164] K. Whittle, G. Lumpkin, and S. Ashbrook, "Neutron diffraction and MAS NMR of Cesium Tungstate defect pyrochlores," *Journal of Solid State Chemistry*, vol. 179, pp. 512-521, 2006.
- [165] G. Katz, "X-Ray Diffraction Powder Pattern of Metastable Cubic ZrO<sub>2</sub>," *Journal of the American Ceramic Society*, vol. 54, pp. 531-531, 1971.
- [166] C. Howard and R. Hill, "The polymorphs of zirconia: phase abundance and crystal structure by Rietveld analysis of neutron and X-ray diffraction data," *Journal of materials science*, vol. 26, pp. 127-134, 1991.
- [167] X. L. Wang, C. R. Hubbard, K. B. Alexander, P. F. Becher, J. A. Fernandez-Baca, and S. Spooner, "Neutron Diffraction Measurements of the Residual Stresses in Al<sub>2</sub>O<sub>3</sub>-ZrO<sub>2</sub> (CeO<sub>2</sub>) Ceramic Composites," *Journal of the American Ceramic Society*, vol. 77, pp. 1569-1575, 1994.
- [168] G. Brauer and H. Gradinger, "Über heterotype Mischphasen bei Seltenerdoxyden. I," *Zeitschrift für anorganische und allgemeine Chemie*, vol. 276, pp. 209-226, 1954.
- [169] A. Zhang, M. Liu, M. Liu, Y. Xiao, Z. Li, J. Chen, *et al.*, "Homogeneous Pd nanoparticles produced in direct reactions: green synthesis, formation mechanism and catalysis properties," *Journal of Materials Chemistry A*, vol. 2, pp. 1369-1374, 2014.
- [170] L. Scriven, "Physics and applications of dip coating and spin coating," in *MRS proceedings*, 1988, p. 717.
- [171] K. D. Litasov, A. Shatskiy, Y. Fei, A. Suzuki, E. Ohtani, and K. Funakoshi, "Pressure-volume-temperature equation of state of tungsten carbide to 32 GPa and 1673 K," *Journal of Applied physics*, vol. 108, p. 053513, 2010.
- [172] K. IS and S. POLYAKOV, "ELECTRON-DIFFRACTION STUDY OF CO<sub>3</sub>O<sub>4</sub>," vol. 17, ed: MEZHDUNARODNAYA KNIGA 39 DIMITROVA UL., 113095 MOSCOW, RUSSIA, 1972, pp. 661-&.



- [173] W. J. Moore Jr and L. Pauling, "The crystal structures of the tetragonal monoxides of lead, tin, palladium, and platinum," *Journal of the American Chemical Society*, vol. 63, pp. 1392-1394, 1941.
- [174] A. W. Hull, "X-ray crystal analysis of thirteen common metals," *Physical Review*, vol. 17, p. 571, 1921.
- [175] R. Stadelmann, M. Lugovy, N. Orlovskaya, P. Mchaffey, M. Radovic, V. Sglavo, *et al.*, "Mechanical properties and residual stresses in ZrB<sub>2</sub>-SiC spark plasma sintered ceramic composites," *Journal of the European Ceramic Society*, vol. 36, pp. 1527-1537, 2016.
- [176] V. Yang and F. E. C. Culick, "On the existence and stability of limit cycles for transverse acoustic oscillations in a cylindrical combustion chamber. 1: Standing modes," *Combustion Science and Technology*, vol. 72, pp. 37-65, 1990.
- [177] F. Culick, "Non-linear growth and limiting amplitude of acoustic oscillations in combustion chambers," *Combustion Science and Technology*, vol. 3, pp. 1-16, 1971.
- [178] N. A. Worth and J. R. Dawson, "Modal dynamics of self-excited azimuthal instabilities in an annular combustion chamber," *Combustion and Flame*, vol. 160, pp. 2476-2489, 2013.
- [179] K. Schadow, E. Gutmark, T. Parr, D. Parr, K. Wilson, and J. Crump, "Large-scale coherent structures as drivers of combustion instability," *Combustion science and technology*, vol. 64, pp. 167-186, 1989.
- [180] A. C. Terracciano, S. De Oliveria, M. Robayo, S. S. Vasu, N. Orlovskaya, "Design and Development of a Flow Stabilized Porous Heterogeneous Combustor," *Submitted to Applied Energy*, 2016.
- [181] A. C. Terracciano, S. De Oliveria, D. Vazquez-Molina, F. J. Uribe-Romo, S. S. Vasu, N. Orlovskaya, "Effect of Catalytically Active Ce<sub>0.8</sub>Gd<sub>0.2</sub>O<sub>1.9</sub> Coating on the Heterogeneous Combustion of Methane Within MgO Stabilized ZrO<sub>2</sub> Porous Ceramics," *Submitted to Combustion and Flame*, 2016.
- [182] A. C. Terracciano, S. De Oliveria, S. S. Vasu, N. Orlovskaya, "Flow Stabilized Porous Heterogeneous Combustor: Operational Parameters and the Acoustic Emission," *Submitted to Fuel Processing Technology*, 2016.
- [183] A. C. Terracciano, S. De Oliveria, D. Vazquez-Molina, F. Uribe-Romo, S. S. Vasu, N. Orlovskaya, "Comparison in the Acoustic and Thermal Profiles of a

Flow Stabilized Porous Media Burner Using Either: Al<sub>2</sub>O<sub>3</sub>, MgO-ZrO<sub>2</sub>, or SiC Media of Constant Porosity and Length," *In Preparation for Submission*, 2016.

- [184] A. C. Terracciano, S. De Oliveria, D. Siddhanti, R. Blair, S. S. Vasu, N. Orlovskaya, "An Evaluation of a Pd Enhanced WC Catalyst to Promote Heterogeneous Methane Combustion," *Accepted to Applied Thermal Engineering*, 2016.